Stellingen

behorende bij het proefschrift

MIGRATION OF SEISMIC DATA IN THE DOUBLE RADON DOMAIN

I

The transformation of the original coordinate system of shot and receiver positions and two-way travel time into shot and receiver ray parameters and vertical travel time causes reorientation of the seismic data according to the local time dip of the interfaces. This new data orientation permits a selective velocity analysis to be performed only on the energy reflected from interfaces with a particular time dip. A very good background model is obtained by analysing only the energy reflected from horizontal segments of the interfaces.

II

The information lost in the Radon transformation is increased in practice for land seismic data with limited offsets, irregular geometry and large spatial shot intervals. The loss of information may exceed the advantages gained by the transformation.

III

A pre-stack or post-stack depth migration produces a migrated depth section of the complex subsurface which is superior to a time section resulting from a time migration, but only if a depth velocity model is known.

IV *The velocity paradox*

"Wave equation migration is a process which tracks waves through a medium of known velocity in order to find unknown reflectors. That the reflectors are in large part caused by the velocity changes that the wave must pass through is a paradox inherent in the process."

R.H. Stolt and A.K. Benson, 1986, *Seismic migration*, *p* 16.

V

Migration in the double Radon domain cannot incorporate laterally varying velocity, because it is a spatial transform method. Therefore it is fundamentally inconsistent to attempt to perform a complete depth migration in this domain.

VI

Unfortunately for velocity analysis, oil tends to occur in the complex geology of rapid lateral velocity variations, rather than in the layer-cake uniformity often assumed by the theory.

N. Anstey, 1982, *Simple Seismics, p* 17.

VII

The testing of algorithms on synthetic data is a necessary, but insufficient, condition for their success on real data.

VIII

The algorithms for the migration of seismic data are often far less sophisticated than the theories on which they are based. The general understanding of the limitations of the theories proceeds more rapidly by studying the performance of the algorithms on the data, than by studying the theories themselves.

IX

When scientists sacrifice their scientific principles for political gain, there is a net loss to science and the political outcome is unpredictable.

X

The "truth" we receive from the media, responding to the authorities, is served to us principally to maintain those authorities in power.

Delft, 15 *June* 1992 *Radmila Tatalovic*

MIGRATION OF SEISMIC DATA IN THE DOUBLE RADON TRANSFORMED DOMAIN

MIGRATION OF SEISMIC DATA IN THE

DOUBLE RADON

TRANSFORMED DOMAIN

Proefschrift

ter verkrijging van de graad van doctor aan de Technische Universiteit Delft,
op gezag van de Rector Magnificus, Prof. drs. P. A. Schenck,
in het openbaar te verdedigen ten overstaan van een commissie
aangewezen door het College van Dekanen op
maandag 15 juni 1992 te 10.00 uur

door

Radmila Tatalovic
geboren te Zrenjanin
Master of Science

Dit proefschrift is goedgekeurd door de promotor
Prof. A. M. Ziolkowski M.A., Ph.D., M.Sc. (Econ.)
en door de toegevoegd promotor Dr. ir. J. T. Fokkema

Let peace return to Yugoslavia

CONTENTS

SUMMARY

The seismic wavefield, as recorded at the surface, has suffered certain changes during propagation through the subsurface, and does not directly indicate the nature of the subsurface. It is the aim of migration to reveal the true geometry of subsurface reflectors. In this thesis, a pre-stack time migration algorithm is developed which is applied to the shot-oriented and double Radon transformed data.

The Radon transform has traditionally been applied to CMP-oriented data, with the assumption that the earth consists of plane horizontal layers. The double Radon transformation consists of two steps: the first transform, with respect to offset coordinate, is applied to all the shot gathers in a seismic line, and the second transform is applied to the once transformed data, with respect to shot coordinate. The introduction of the second transform makes it possible to apply the Radon transform without making the assumption of a horizontally layered earth.

In the double Radon domain, the data are discretized according to the local time dip of the acoustic interfaces. The phase function becomes separated into two parts, the horizontal phase and the vertical phase. This makes it possible to perform the imaging of the data by keeping the vertical slowness constant. With the application of this condition the energy reflected from a particular interface is selected into an imaging plane. One inverse transformation applied to the data in the imaging plane leads to the time image of the interface. The method of stationary phase used to derive the imaging equations is a high frequency approximation, which emphasizes the onset of the seismic events.

The migration equations are derived for a single arbitrarily shaped interface, and then extended to include any arbitrarily layered subsurface by introducing a smooth background RMS velocity model. Due to the data discretization in the double Radon domain, the velocity can readily be obtained from the double Radon transformed data. A plane in the double Radon transformed data cube is selected, in which only reflections from the horizontal segments of the

interfaces are present. Not only is the best fit between the theoretical curves and the data achieved in this plane, but also the RMS velocity function is obtained rather than the stacking velocity.

The derived background velocity function is valid for the entire data set; since the migration is applied in the spatially transformed domain, the velocity cannot be varied laterally. This can be regarded as both the drawback of the method, as well as its strength. It is not desirable for a migration algorithm to be unable to accept a laterally variant velocity model; however, a laterally variant velocity model is the result expected *from* the migration and thus it is not available *prior* to migration. The result of any migration algorithm which can handle a laterally variant velocity model, is heavily influenced by the *approximate* laterally variant velocity model. On the other hand, a migration algorithm which does not require laterally changing velocity field, such as the one presented in this thesis, produces result which is much more influenced by the data than by the *approximate* laterally variant velocity model.

The method has been successfully applied to two complex data sets: the Marmousi synthetic data set and the Tubbergen field data set. In spite of difficulties involved with the practical application, such as great structural complexity in the Marmousi data and the irregular shooting geometry in the Tubbergen data, good results have been achieved for both data sets. These results are encouraging for the further research.

NOTATIONS AND CONVENTIONS

In this thesis, orthogonal Cartesian coordinates x_1, x_2, and x_3 are employed in a right handed system to locate a point in space, together with vectors $\boldsymbol{i}_1$, $\boldsymbol{i}_2$, and $\boldsymbol{i}_3$, where $\boldsymbol{i}_3$ is pointing downwards. Vectors are typed bold-faced.

The list of major symbols follows:

t	Time coordinate	(s)
f	Frequency	(s^{-1})
$\omega = 2\pi f$	Angular frequency	$(rad \cdot s^{-1})$
$s \rightarrow -i\omega$	Laplace transform parameter	$(rad \cdot s^{-1})$
p	Horizontal slowness (Ray parameter)	$(s \cdot m^{-1})$
q	Vertical slowness	$(s \cdot m^{-1})$
$\alpha \rightarrow -ip$	Spatial Fourier transform parameter	$(s \cdot m^{-1})$
k_x	Wave number	(m^{-1})
$K_x = 2\pi k_x$	Wave number	(m^{-1})
$p\ (x,t)$	Acoustic pressure	$(Pa = N \cdot m^{-2} = kg \cdot s^{-2} \cdot m^{-1})$
$\widehat{w}(s)$	Source function, $\widehat{w}(s) = -s\rho w(t)$	$(kg \cdot s^{-2})$
$\widehat{w}(\omega)$	Source function, $\widehat{w}(\omega) = i\omega\rho w(t)$	$(kg \cdot s^{-2})$
$\widehat{G}(x,s)$	Green's function	(m^{-1})
c	Acoustic velocity	$(m \cdot s^{-1})$

In this thesis, the following transformations are used: Fourier transform (both temporal and spatial), Laplace transform, and Radon transform.

The temporal Fourier transform pair, as defined in this thesis, is given by

$$\hat{f}(\omega) = \int_{-\infty}^{\infty} f(t)\, exp\,(i\omega t)\, dt\,,$$

and

$$f(t) = \int_{-\infty}^{\infty} \hat{f}(\omega)\, exp\,(-i\omega t)\, d\omega\,.$$

For causal time functions, where the function f does not exist for $t < 0$, the temporal Fourier pair becomes

$$\hat{f}(\omega) = \int_{0}^{\infty} f(t)\, exp\,(i\omega t)\, dt\,,$$

and

$$f(t) = 2\,Re\left[\int_{0}^{\infty} \hat{f}(\omega)\, exp\,(-i\omega t)\, d\omega\right].$$

The one-sided Laplace transform with respect to time, with real and positive transform parameter s, applied to a causal time function $f(t)$ is defined as

$$\hat{f}(s) = \int_{0}^{\infty} f(t)\, exp\,(-st)\, dt\,,\ s > 0.$$

The Radon transform pair for a 2-dimensional function in the frequency domain is defined as

$$\tilde{\hat{f}}(p,\omega) = \int_{-\infty}^{\infty} f(x,\omega)\, exp\,(-i\omega p x)\, d\omega\,,$$

and

$$\hat{f}\,(x,\omega) = \int_{-\infty}^{\infty} \tilde{\hat{f}}(p,\omega)\, exp\,(i\omega p x)\, dp\,.$$

The notations in the various domains are as follows:

SPACE-TIME DOMAIN	FREQUENCY DOMAIN	WAVE NUMBER DOMAIN	RAY PARAMETER DOMAIN
$f(x,t)$	$\hat{f}(x,\omega)$	$\bar{\hat{f}}(k_x,\omega)$	$\tilde{f}(p,\tau)$

1

INTRODUCTION

1.1 INTRODUCTION TO MIGRATION

The seismic method of geophysical exploration is based on changes in the propagating wavefield which are caused by subsurface reflectors. A subsurface reflector can be described as a discontinuity in the acoustic impedance of the earth, while the acoustic impedance is given as a product of seismic velocity and density. The change in acoustic impedance gives rise to reflections, with the amplitude of the reflected wave determined by the density and the velocity contrast, and the phase of the reflected wave, that is the timing of the the seismic event, determined only by the velocity part of the acoustic impedance.

The wavefield, as recorded at the surface, has suffered certain changes during propagation through the subsurface, and does not directly indicate the nature of the subsurface. It is the aim of migration to reveal the true geometry of subsurface reflectors. Since the positioning of reflections on a seismic section is determined by the velocity distribution, it follows that the aim of migration is to reveal the velocity structure of the subsurface. One way to view migration is to observe how the reflections approach the shape of the reflectors as the sources and the receivers are lowered down through the earth, towards the reflectors. In the limiting case, when the sources and the receivers are positioned directly above the discontinuities, they record the exact shape of the reflectors, and there is no wave distortion any more. The effect of migration is illustrated with three synthetic examples, created by summing diffractions from all point scatterers along an interface.

The first example shows a synthetic zero-offset section over a horizontal strip in Figure 1.1.1a. With the zero-offset section it is understood that the source and the receiver are coincident, and the reflection recorded on each trace originates from normal incidence rays, that is, rays which strike the reflector at 90°. The zero-offset section in Figure 1.1.1a does not reproduce a correct picture of the reflector due to diffracted energy at the edges of the strip: at both ends of the strip the reflection is followed by the diffraction, and from the zero-offset section alone it is difficult to distinguish between the reflection and the diffraction.

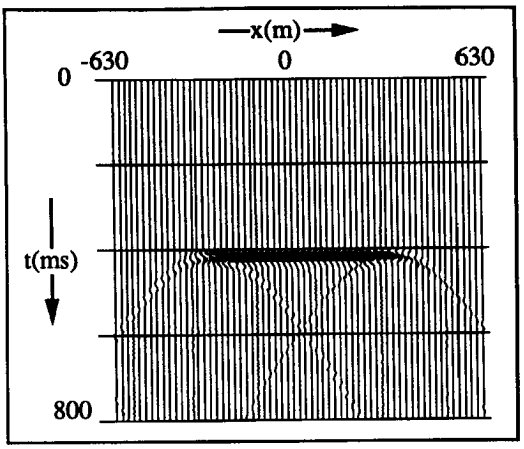

Fig.1.1.1a: The horizontal strip model: The zero-offset section

The generation of diffractions is explained in Figure 1.1.1b: since the edge of the strip can be considered as a point, an infinite number of normal incidence rays can be reflected from this point. The diffraction hyperbola is formed when these rays are plotted directly below the source-receiver position. As the source-receiver level is lowered down to the reflector, the diffraction energy is collapsed. At the end, the effect of the migration is the same as positioning the sources

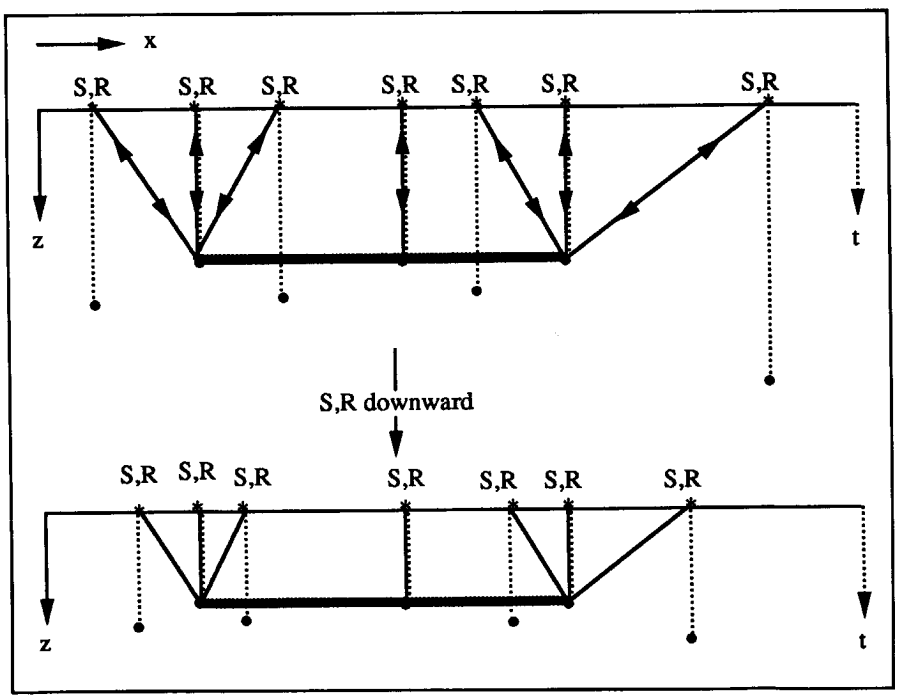

Fig.1.1.1b: The horizontal strip model: Diffraction generation

and the receivers directly above the reflector: the two diffractions are collapsed into "points" at the edges and the horizontal extent of the strip is easily determined on the migrated section in Figure 1.1.1c.

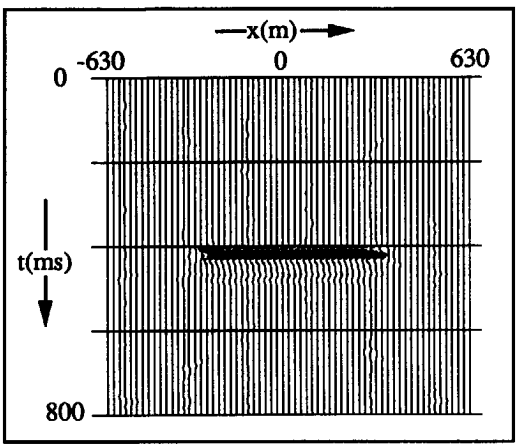

Fig.1.1.1c: The horizontal strip model: The migrated section

The second example illustrates a case of a plane interface dipping at an angle θ. On a synthetic zero-offset section in Figure 1.1.2a the interface appears to be dipping at an angle α, which is smaller than the true dip angle. The mechanism which creates the apparent dip is explained in Figure 1.1.2b, where two normal incidence rays are traced to the reflector. On the zero-offset section, the travel-times of these two rays are plotted directly below their source-receiver positions, creating the reflection R of the discontinuity D. From the geometry of Figure 1.1.2b, it follows that the apparent dip and the true dip are related as

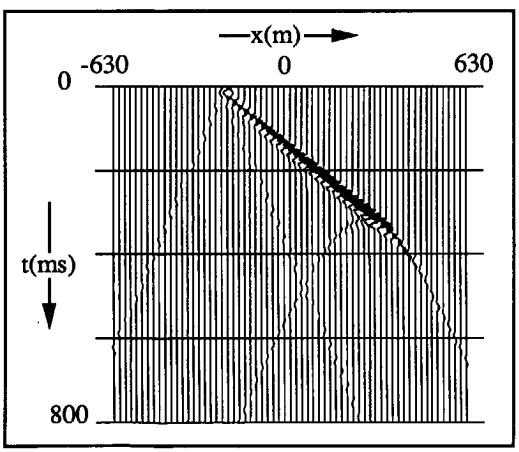

Fig.1.1.2a: The dipping layer model: The zero-offset section

$$tan\ \alpha = sin\ \theta. \qquad (1.1.1)$$

On the migrated section in Figure 1.1.2c the reflection from the dipping interface is migrated to its true time position. The true dip of the interface is recovered by relating the time to depth by the velocity of the wave propagation.

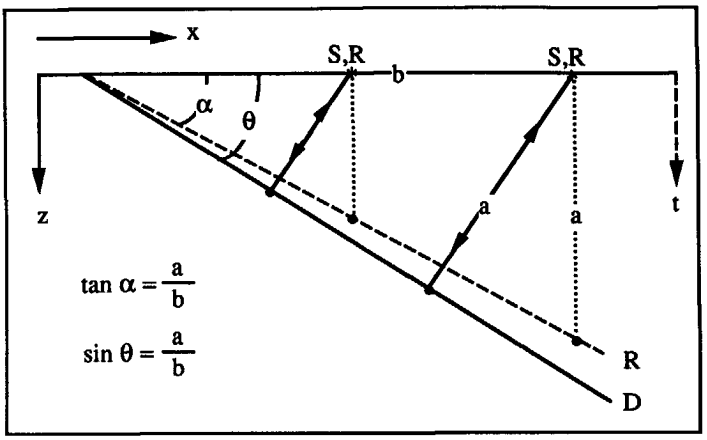

Fig.1.1.2b: The dipping layer model: A geometrical explanation for the apparent dip

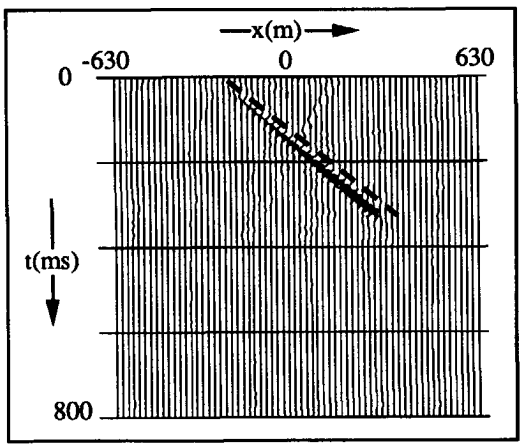

Fig.1.1.2c: The dipping layer model: The migrated section, with the dashed line indicating the position of the reflection on the unmigrated section.

In the third example, Figure 1.1.3a shows a rather complicated synthetic zero-offset section over a syncline, where the reflections are not only obscured by the energy diffracted from the edges of the syncline, but are also distorted by the reflector curvature. The same mechanism which creates the diffractions and the apparent dip of the dipping interface is employed to explain the zero-offset section of the syncline in Figure 1.1.3.b. Three normal incidence rays

are traced from one source-receiver surface position; the arrival times plotted directly below this position in Figure 1.1.3c give rise to the complicated "bow-tie" appearance of the zero-offset section over a syncline. The migration collapses the diffractions, maps the reflections from the curved interface back to their true time position, and the shape of the syncline becomes obvious in the migrated section in Figure 1.1.3d.

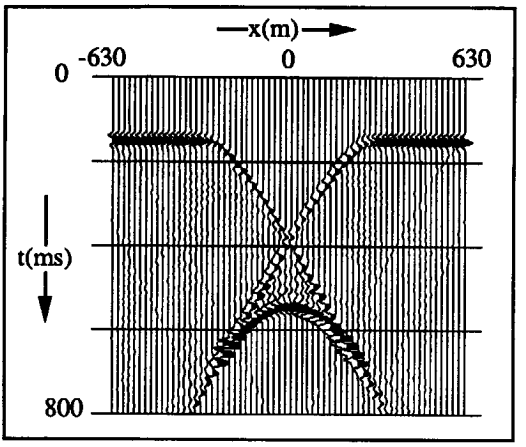

Fig.1.1.3a: The syncline model: The zero-offset section

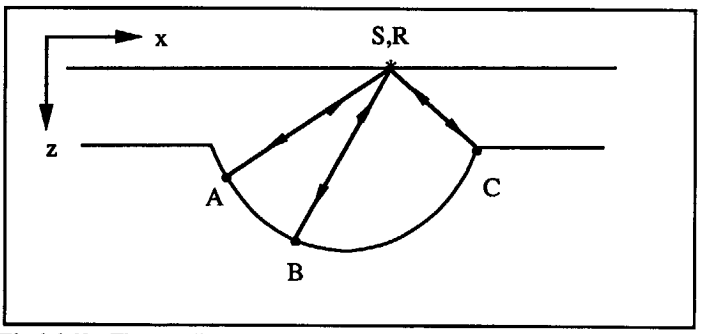

Fig.1.1.3b: The syncline model: The depth model

The three examples chosen here are quite simple; when the complexity of the earth is considered, the *need* for migration becomes clear. The question which remains is *how* to do migration.

1.2 THE CONVENTIONAL APPROACH TO MIGRATION

1.2.1 Classification

The migration methods which are in use in seismic data processing can be classified according to several different criteria as follows:

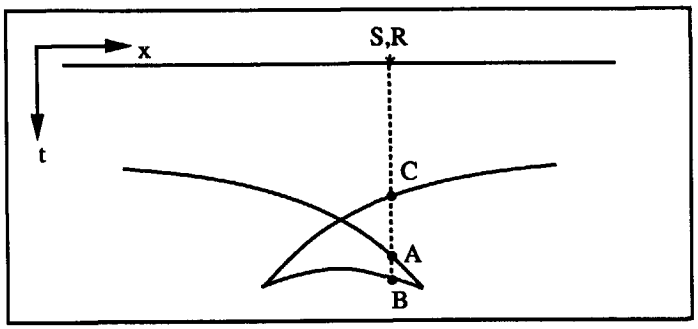

Fig.1.1.3c: The syncline model: A geometrical explanation for the apparent dip

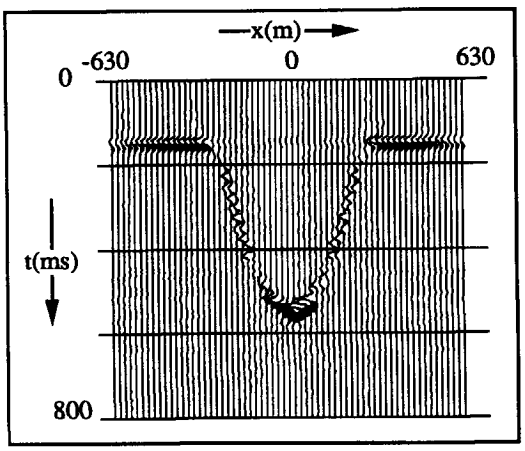

Fig.1.1.3d: The syncline model: The migrated section

1) Based on its place in the processing sequence, the migration can be applied either as:
   - pre-stack migration, or
   - post-stack migration.

Migration applied to stacked data assumes that the stacked section is a good approximation of a zero-offset section. In post-stack migration, the sources and the receivers are coincident, and can be downward continued simultaneously, whereas in pre-stack migration they have to be downward continued separately, according to their spatial coordinates. Post-stack migration often employs the exploding reflector model (Loewenthal et al., 1976), in which the reflectors in the earth are replaced by seismic sources, which all explode at time $t = 0$. The waves travel at half the seismic velocity, and are recorded by the receivers which are positioned at the surface. There are two *motivations* for post-stack migration: first, stacking has attenuated the multiple reflections, and the assumption of a primaries only model is therefore good; second, since stacking has reduced the data volume, the cost of the process is much lower than the pre-stack migration. The main *problem* with it is that the approximation of a zero-offset section is often

violated, specially in areas with conflicting dips or strong lateral velocity changes, where the incorrect stacking procedure will destroy the information rather than enhance it.

A considerable amount of time and effort has been directed towards developing procedures for improving stacking in problematic areas. These procedures, known as partial migration before stack, or dip moveout (DMO), to a certain extent solve the conflicting dip problem. Various researchers have worked on this problem: Sherwood et al. (1978), Yilmaz and Claerbout (1980), Deregowski and Rocca (1981), Hale (1984), Fowler (1984), French et al. (1984). DMO methods vary in the domains in which they are applied, the computational effort required, and the accuracy of the solution. All these methods try to map non-zero offset data to zero-offset data in the presence of conflicting dips to enable proper stacking, which can then be followed by some conventional migration scheme. According to Yilmaz (1987), there are several problems with DMO processing: the methods based on a constant velocity assumption can suppress dipping events instead of preserving them; some methods are limited to small dips and small offsets; DMO sometimes enhances multiples; and finally, some of these methods handle only small lateral velocity variations. It is theoretically more justifiable, although more exhaustive, to apply migration prior to stacking.

2) Based on the extrapolation coordinate, the algorithms are organized either as:

- time migration, or
- depth migration.

For time migration, the input velocity model is given as a function of time, the extrapolation is performed in steps of time, and the output is a migrated time section. For depth migration the interval velocity model is given as a function of depth, the extrapolation is performed in steps of depth, and the output is a depth section. Generally, time migration algorithms are more approximate than depth migration algorithms, but they are more robust; the input model for the time migration is given as a RMS velocity function, and as a consequence the output from such an algorithm gives a less detailed answer than depth migration. On the other hand, the depth migration algorithms, which are preferable in geologically complicated areas, produce more detailed depth images of the subsurface, but they also require more detailed input velocity models; the resulting depth images, which heavily depend on the input velocity models, are only correct when a very good estimate of the true subsurface velocity field is available.

3) Based on the extrapolation domain, the algorithms are grouped as:

- time-space (t-x) migration,
- frequency-wavenumber (f-k) migration, or
- frequency-space (f-x) migration.

Historically, the time-space algorithms were developed first. The frequency-wavenumber migration algorithms were developed either to increase the accuracy or to speed up the computations. The major advantage of time-space algorithms is that velocity can vary both

vertically and horizontally, which is not possible in the frequency-wavenumber domain. The frequency-space algorithms combine some of the advantages of the original and transformed domains.

4) Based on the input for each extrapolation step, the algorithms can be:

- recursive migration, or
- non-recursive migration.

In recursive algorithms, the velocity model is subdivided into a number of horizontal strips, usually of a small thickness. Then the extrapolation and imaging are performed for each horizontal strip separately, the output from one strip being the input for the following strip. The important advantage of recursive techniques is that they can incorporate velocity changes; the main disadvantage is that small errors at each step will accumulate as the extrapolation proceeds. In non-recursive algorithms, the input to the migration program is always the data recorded at surface, whether it is carried out in one or more steps. The non-recursive techniques are generally numerically less exhaustive, since at each step the data need only to be evaluated at $t = 0$.

Further, most of the existing algorithms can be extended from 2 dimensions to 3 dimensions; then, rather than solving a problem of a seismic profile along a line, an area of two horizontal dimensions is considered. This is a rather important aspect in seismic migration, since very often 3D features cannot be neglected or approximated as 2D, and consequently the 2D migration cannot reveal the structure properly.

1.2.2 Major contributions

As wave propagation through the earth is governed by the wave equation, the migration of seismic data is usually formulated as the back propagation of waves. Therefore, the solution to the migration problem is sought as the solution to the wave equation. The 2D scalar wave equation, which describes propagation of compressional waves $p = p\,(x,z,t)$, where x and z are the horizontal and the vertical spatial coordinate and t is the time coordinate, in a medium of constant density and velocity c, is given by

$$\frac{\partial^2 p}{\partial x^2} + \frac{\partial^2 p}{\partial z^2} - \frac{1}{c^2}\frac{\partial^2 p}{\partial t^2} = 0 \,, \tag{1.2.1}$$

in which it is assumed that there are no sources.

It is often more convenient to consider the wave equation in the Fourier domain, which can be achieved by the substitutions of the time coordinate t by angular frequency ω, the horizontal spatial coordinate x by the horizontal wave number k_x, and the vertical spatial coordinate z by the vertical wave number k_z

$$\frac{\partial}{\partial t} = -i\omega$$
$$\frac{\partial}{\partial x} = ik_x \qquad (1.2.2)$$
$$\frac{\partial}{\partial z} = ik_z .$$

Substitution of the first two of equations 1.2.2 into the time-space domain representation of the wave equation, leads to the expression which describes the propagation of plane waves $P = P(k_x,z,\omega)$ as

$$\frac{\partial^2 P}{\partial z^2} + \left(\frac{\omega^2}{c^2} - k_x^2\right) P = 0 . \qquad (1.2.3)$$

Various ways of solving the wave equation - that is various approximations applied to the wave equation in order to solve it - have led to various schemes for the migration of seismic data.

Finite-difference migration was pioneered by Claerbout (1970), Claerbout and Johnson (1971), and Claerbout and Doherty (1972). The finite difference techniques approximate the partial derivatives in the wave equation with the operators which work with the difference between neighbouring grid points from a mesh of discrete sampled data. The name "finite difference" then refers to the approximation of derivatives (that is the infinitesimal differences) with finite differences. The paraxial wave equation is solved instead of the scalar wave equation (Claerbout, 1985), mainly to avoid the difficulties which arise from internal multiples created by the scalar wave equation, evanescent waves, and the need for the second partial derivatives in depth as the boundary conditions, which are not available. The paraxial wave equation, or the one-way wave equation in the Fourier domain is given as

$$\frac{\partial P}{\partial z} - i\sqrt{\frac{\omega^2}{c^2} - k_x^2}\; P = 0 , \qquad (1.2.4)$$

and the solution to the paraxial wave equation in the Fourier domain is given by

$$P(k_x,z,\omega) = P(k_x,z=0,\omega)\; exp\left(-ik_z z\right). \qquad (1.2.5)$$

The square root in the paraxial wave equation describes the dispersion relation

$$k_z = \frac{\omega}{c}\sqrt{1-\left(\frac{ck_x}{\omega}\right)^2}\,. \tag{1.2.6}$$

This square root is rewritten in the time-space domain using equations 1.2.2, expanded into a series as a polynomial ratio and subsequently truncated, leading to various approximate solutions. The "15° migration", obtained by keeping only the first two terms of the series, can handle dips up to 15° properly. It has an effect of replacing the second depth derivative in the scalar wave equation by a mixed first derivative in depth and time. The extension of "15° migration" to include another term in the series leads to the "45° migration", which treats dips up to 45° properly.

Reverse time migration (Baysal et al., 1983, and McMechan, 1983) also uses finite differences to solve the wave equation, but it starts from the scalar wave equation, rather than the paraxial wave equation. The wave propagation is carried out backwards in time, starting from the last recorded time sample. The migrated depth image is obtained when zero time is reached. This algorithm is more accurate for higher dips than the finite-difference migration based on paraxial equation, since the scalar wave equation is valid for all dips.

Kirchhoff summation migration was introduced by French (1975) and Schneider (1978). This method is based on the integral formulation of the solution of the scalar wave equation, where the recorded seismic data at the surface are considered as the boundary value, and the migrated image is obtained by solving the line integral (2D) or surface integral (3D) over the recorded data. In the 2D case, the integral solution is given as

$$P(x,z,t) = \frac{1}{2\pi}\int\left[\frac{\cos i}{R^2}P\left(x, z=0, t-\frac{R}{c}\right)+\frac{\cos i}{cR}\frac{\partial}{\partial t}P\left(x, z=0, t-\frac{R}{c}\right)\right]dx\,, \tag{1.2.7}$$

where R is the distance between the surface point and the subsurface point, and i is the angle between the direction of propagation and the vertical axis z. The contribution of the first term (near-field term) is negligible compared with the contribution of the second term (far-field term), and is often dropped in practical applications. This integration amounts to summing the amplitudes along hyperbolic trajectories for each reflection point, where the hyperbolic trajectories are determined by subsurface velocities. The integration is performed for the entire data, and the migrated result at each location is obtained by setting $t = 0$.

The Kirchhoff summation method was originally developed as a non-recursive scheme in the time-space domain. It was later formulated in the frequency-space domain as a recursive scheme, in order to take into account both vertical and lateral velocity variations (Berkhout and van Wulfften Palthe, 1979). If the extrapolation is implemented as a spatial convolution, the advantage of operating in the frequency-space domain is obvious (Berkhout, 1980): the

convolution is two dimensional in t-x (along both the t and the x axis), but it is one dimensional in the f-x domain (over the x-axis only).

The Stolt f-k migration was introduced by Stolt (1978), as a fast migration procedure in the frequency-wavenumber domain. It was recognized that the dispersion relation (equation 1.2.6) can be used to map the data from a grid regular in k_x-ω into a grid regular in k_x-k_z, which is, in the space domain, equivalent to a map from x-t into x-z. This simple mapping is explained in Figure 1.2.1, which also shows how the apparent dip α is related to the true dip θ in the Fourier domain. The entire migration is achieved with fast Fourier transform algorithms and mapping. The dispersion relation holds for constant velocity only; the change of velocity in the vertical direction can be approximated by a stretch of the time axis prior to migration.

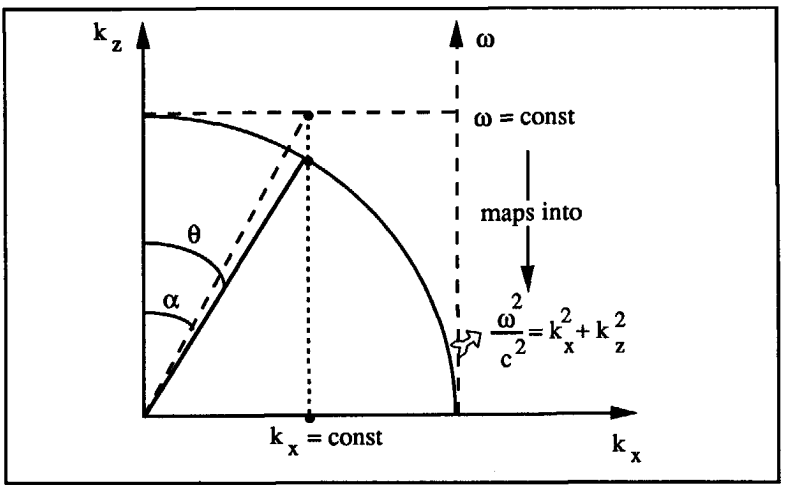

Fig.1.2.1: Frequency mapping in the Fourier domain for the f-k migration. The event dipping at the apparent dip angle α (dashed line) in the ω-k_x domain is mapped into an event dipping at the true dip angle θ (solid line) in the k_z-k_x domain.

The phase shift migration (Gazdag, 1978) is also implemented in the f-k domain. The solution to the wave equation in the f-k domain is the sum of monochromatic plane waves (equation 1.2.5); the propagation of a plane wave is governed by its phase. The extrapolation of the wave field is achieved by the phase shift of each plane wave component separately, through strips of a small thickness and uniform velocity

$$P(k_x, z + \Delta z, \omega) = P(k_x, z = 0, \omega)\, exp\left(-i k_z \Delta z\right). \qquad (1.2.8)$$

After extrapolation at each depth step, the data are imaged for time $t = 0$. The vertical variation in velocity is implemented by assigning a different velocity to each depth strip. An approximate way to include the lateral variation of velocity is by applying the extrapolation in each depth step

with several different (but each time uniform) velocities, and the final result is obtained by interpolating between individual wave fields (Gazdag and Squazzero, 1984).

Split-step Fourier migration is an extension to the phase shift method, developed to include lateral velocity changes (Stoffa et al., 1990a). This method is based on decomposing the interval slowness (reciprocal of interval velocity) into a mean vertically varying slowness and a laterally varying perturbation in each depth interval. The downward continuation of the wavefield across each depth interval is accomplished in two steps. The first step employs a phase shift in the frequency-wavenumber domain using the mean slowness in the depth migration interval. The second step is a phase shift in the frequency-space domain that takes into account the lateral slowness contribution. This method has been further developed to perform migration prior to stack (Stoffa et al., 1990b).

1.2.3 Common problems with migration methods

All described methods have four things in common: they

1) assume there is no free surface,

2) assume there are no internal multiple reflections,

3) assume the velocity model is known, and

4) perform extrapolation prior to imaging.

The first two assumptions imply that only primary reflections are present in the seismogram. In post-stack migration algorithms the primary-only assumption is based on the property of the free-surface multiples becoming largely attenuated in the stacking process. The internal multiples are usually ignored, since they do not stack out, unless there are significant velocity changes with depth. The primaries-only assumption is particularly poor for pre-stack migration algorithms, unless the multiples can be removed using methods other than migration. The multiples which are still present in the seismogram are migrated as primaries. The algorithm presented in this thesis also ignores the presence of the multiples and assumes that they have been removed.

The migration equations are usually derived by solving the wave equation for a constant velocity medium. After the solution has been derived, the velocity is then allowed to vary vertically, or even horizontally. A crucial input for all known migration algorithms is the velocity model. But the velocity model is the *answer* which is expected from the migration. This is known as the "velocity paradox" (Stolt and Benson, 1986). In practical applications, the velocity model supplied for the migration process is usually provided by the stacking velocity analysis. This starting model is then allowed to change in the following migration runs, leading to a "better" result. This is a costly process, and a lot of research is being carried out to ensure fast convergence to the right answer. This is the property inherent in all the migration methods, and at present cannot be avoided. The migration algorithm in this thesis goes a step further, but still does not solve the velocity paradox completely. The constant velocity medium, which is bounded by an arbitrarily shaped interface, is here also extended into an arbitrary velocity distribution in the derivation of the migration equations. Further, it does not require an accurate

velocity model as input, and provides a method for obtaining the background RMS velocity function from the data.

With the known velocity model, the migration is usually performed in two steps: first, the sources and the receivers are *extrapolated* down to a new depth level; second, the data are *imaged* at the time $t = 0$. This two-step procedure is repeated until the source-receiver pairs have been lowered through all the available data. Such a procedure is only possible with a known velocity model. In the migration presented in this thesis, the imaging is the crucial step and it is performed independently of the extrapolation; the complete migration can be performed in one imaging step. As an extension to this theory, an extrapolation procedure can be developed as a follow-up procedure which would yield a depth image of the subsurface.

The most serious, unsolved problem with migration is the velocity paradox. For all migration algorithms described so far, the following holds: migration is applied to discover the true position of subsurface velocity discontinuities, given the seismic data, and given the *approximate* value of seismic velocities and *approximate* position of the velocity discontinuities, as observed on seismic data. When this approximate velocity model is not the correct one, the seismic events are migrated to wrong positions, thus creating a false picture of subsurface discontinuities.

When migration with the wrong velocity is applied pre-stack, the events on each offset will be migrated to a different position. This can be used for a self-consistent migration velocity analysis, often called the macro velocity model estimation, in the same form as the iterative forward modelling by model-fitting. The principle is similar to the stacking velocity analysis, where the use of the correct velocities will straighten the events in a CMP gather, but the use of wrong velocities will cause a residual moveout which then can be used to estimate the "true" or "less wrong" velocity. This is explained on an example of pre-stack split-step migration (Tatalovic et al., 1990), which performs migration on the τ - p transformed CMP gathers. For the purpose of velocity estimation, the data are migrated with a number of trial velocity functions. As shown in Figure 1.2.2, the event migrated with the correct velocity is horizontal, too low a velocity causes smaller travel times at higher ray parameters, and too high a velocity causes increased travel times at higher ray parameters. The amount of curvature can than be used to improve the velocity estimate for the next migration run. The remaining problem with all these methods is how to choose the starting trial velocity model, and how to ensure a fast convergence to the right model.

For post-stack migration algorithms, however, there is no such control of output other than whether the migrated section "looks good". The wrong velocity model used to back propagate the seismic waves will position the reflectors to the wrong places, thus creating a false picture of the subsurface.

1.3 MIGRATION IN THE DOUBLE RADON TRANSFORMED DOMAIN

The high dependence of conventional migration algorithms on prior knowledge of the velocity field has motivated the development of a new method, namely pre-stack time migration

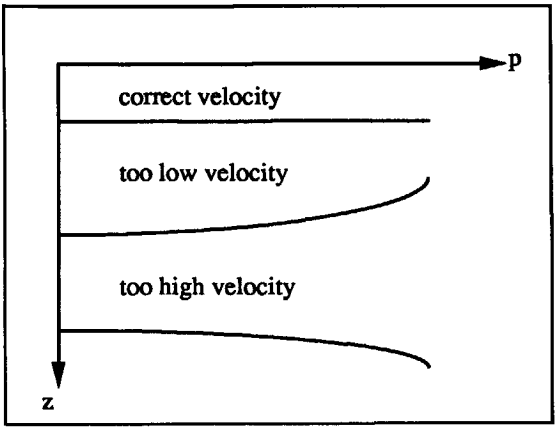

Fig.1.2.2: A CMP gather with three events migrated using the correct velocity, too low velocity, and too high velocity

in the ray parameter-frequency domain. In terms of classification described in section 1.2.1, the new method can only be clearly classified based on the first two criteria: it is a pre-stack, time migration. Based on the third criterion, it mostly corresponds to the frequency-wavenumber methods, since both temporal and spatial coordinates are transformed, but it differs in the spatial transform parameter. The fourth classification cannot be applied directly to this method, since this classification is mainly based on the extrapolation part of the migration, which, at present, is not included in this migration method. Imaging is performed in one step for the entire data, and as such can be regarded as a non-recursive method.

The double Radon domain is approached by transforming offset and source coordinates into corresponding ray parameters, and the time coordinate into frequency. In this domain, the data are discretized according to the local time dip of the velocity discontinuity interfaces. Thus, by taking the double Radon domain with respect to offset and shot coordinates, the spatial characteristics of the interfaces become separated from the ray-parameter dependent characteristics in the phase function. In the mathematical derivation of the migration equations, the stationary phase method is employed to solve the resulting integrals, which, as a high frequency approximation, emphasizes the *onset* of the arriving waves.

The earth model and the approximations made are explained in the mathematical derivation of the double Radon transform in chapter 2. It is shown how the application of two Radon transformations with respect to the spatial coordinates helps to separate the phase of the transformed wavefield into a horizontal and a vertical part. Also, the implementation of the double Radon transform using fast Fourier transforms and interpolation procedures is explained.

The main part of this thesis is imaging in the double Radon transformed domain, described in detail in chapter 3. The imaging is applicable not only to one arbitrarily shaped interface, but also to an arbitrarily layered earth by introducing the RMS velocity. It is shown how the RMS velocity function can be estimated from the double Radon transformed data. Since the data in the

double Radon domain are discretized according to the local time dip of the interface, the velocity analysis is performed in a plane where only contributions from horizontal interface segments are present.

The new aspects of the double Radon domain and migration in this domain are explained in chapter 4. These include an explanation of geometrical aspects of the double Radon domain, the reciprocity principle which can be applied in either the space-time domain or the double Radon domain, the changes which the wavelet suffers during these operations, and the consistency of the migration when the seismic line is broken into smaller segments.

Throughout the thesis, the explanations are illustrated using simple synthetic data examples. The performance of the method is demonstrated in chapter 5 on two complex data sets, the Marmousi synthetic data set and the Tubbergen field data example.

Finally, the thesis is concluded in chapter 6 with a discussion of the new method and possibilities for its extension.

2

DOUBLE RADON TRANSFORM

2.1 INTRODUCTION

The mathematical derivation of the double Radon transformation described in this chapter follows the theory of Fokkema and van den Berg (1992). The starting point is the boundary integral representation of the scattered field, by which the scattered field is expressed as a surface integral of the contributions from monopole and dipole secondary sources, distributed along the interface. The boundary integral describes the seismic data, provided the incident field has been removed. By applying a locally plane reflector approximation, the incident field is related to the scattered field through reflection coefficients. With these relations the source-related Green's function is introduced into the boundary integral representation, leading to an expression suitable for the transformations. The time coordinate of the data is subjected to a one-sided Laplace transform, and the whole asymptotic analysis is carried out in the Laplace domain. A spatial Fourier transform is applied to the horizontal receiver coordinates, and the resulting integrals are solved by carrying out an asymptotic analysis and applying the steepest descent arguments. The same procedure is repeated for the horizontal source coordinates. At this point, it becomes obvious that an important advantage is gained by applying the Radon transformation with respect to two horizontal spatial coordinates: the horizontal phase and the vertical phase of the propagating waves become separated. The receiver-source coordinate system is then transformed to an offset-source coordinate system, and the offset and the source ray parameters are introduced. The imaginary axis of the Laplace transform domain is turned into the frequency axis. The transform is finished by applying the source-receiver alignment and a scaled frequency domain filter, resulting in a double Radon transformed scattered field as a function of the offset and source ray parameters and frequency.

The equations for the double Radon transform are derived for 3D data, where the transforms are applied to two spatial dimensions for both sources and receivers. The algorithm is implemented for the 2D situation, where one of the spatial dimensions is set to zero, and for 2.5D data, where the source and the receiver are each approximated by a point. Instead of

Laplace transformation, the data are transformed to the frequency domain using a temporal Fourier transform. Then the double Radon transform can be achieved by using spatial Fourier transforms and interpolations, leading to the data as a function of offset ray parameter and source ray parameter. Finally, the data are inverse Fourier transformed from the frequency domain to vertical travel time.

2.2 EARTH MODEL AND APPROXIMATIONS

The changes in the propagating wave field are caused by discontinuities in the acoustic properties of the earth. These discontinuities are interfaces of arbitrary shape between the isotropic homogeneous earth layers with different acoustic parameters. To derive the equations for the double Radon transform, two such layers are considered and are shown in Figure 2.2.1. The two layers, D_0 and D_1, with acoustic velocities c_0 and c_1 respectively, are separated by the arbitrarily shaped interface S. In Cartesian coordinates $\boldsymbol{x} = \{x_1, x_2, x_3\}$, this interface is described as

$$x_3 = h(x_1, x_2), \tag{2.2.1}$$

where h is an arbitrary, but smooth function of horizontal coordinates x_1 and x_2.

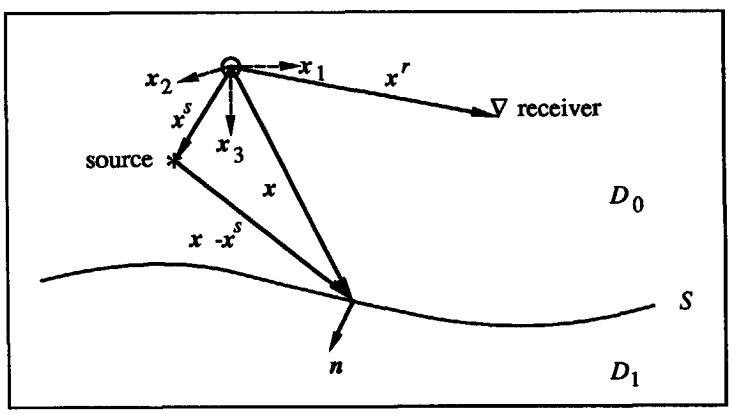

Fig.2.2.1: The scattering geometry

The source, located at $\boldsymbol{x}^s = \{x_1^s, x_2^s, x_3^s\}$, generates an impulsive wave field at time $t = 0$. The receiver, located at $\boldsymbol{x}^r = \{x_1^r, x_2^r, x_3^r\}$, records the field scattered by the interface S. Both the source and the receiver are located above the interface.

For mathematical convenience, the asymptotic analysis is carried out in the Laplace domain. The one-sided Laplace transform with respect to time, with real and positive transform parameter s, applied to a causal time function $f(t)$ is given by

$$\hat{f}(s) = \int_0^\infty f(t)\, exp\,(-st)\, dt, \quad (s) > 0\,. \tag{2.2.2}$$

The function $\hat{f}(s)$ has no singularities in the right half of the complex s-plane, and consequently the real part of the complex s-values can be allowed to approach zero. Then, after the double Radon domain has been achieved, the imaginary axis of the Laplace domain can be regarded as the frequency axis through $s \rightarrow -i\omega$.

In the s-domain, the source field generated by an explosive source located at $\boldsymbol{x}^s$, and observed at point $\boldsymbol{x}$ is given by

$$\hat{p}^{inc}(\boldsymbol{x},\boldsymbol{x}^s) = \hat{W}\,\hat{G}_0(\boldsymbol{x}-\boldsymbol{x}^s)\,, \tag{2.2.3}$$

where $\hat{W} = \hat{W}(s)$ is the Laplace transform of the source function $w(t)$. In the Laplace domain, the Green's function $\hat{G}_0$ for a point source located at $\boldsymbol{x} = 0$ is given by

$$\hat{G}_0(\boldsymbol{x}) = \frac{exp\left[-\frac{s}{c_0}|\,\boldsymbol{x}\,|\right]}{4\pi|\,\boldsymbol{x}\,|}, \tag{2.2.4}$$

where the distance $\boldsymbol{x}$ is given by

$$|\boldsymbol{x}| = \sqrt{x_1^2 + x_2^2 + x_3^2}\,. \tag{2.2.5}$$

The wavefield scattered by the interface S can be considered as the field generated by the secondary sources along interface S (Bleistein, 1984; Fokkema and van den Berg, 1992), and is expressed as a surface integral over these sources as

$$\hat{p}^{sct}(\boldsymbol{x}^r,\boldsymbol{x}^s) = \iint_{\boldsymbol{x}\,\in\,S} \left[\hat{G}_0(\boldsymbol{x}^r-\boldsymbol{x})\,\partial_n\left(\hat{p}^{sct}(\boldsymbol{x},\boldsymbol{x}^s)\right) - \partial_n\left(\hat{G}_0(\boldsymbol{x}^r-\boldsymbol{x})\right)\hat{p}^{sct}(\boldsymbol{x},\boldsymbol{x}^s)\right] dS. \tag{2.2.6}$$

In this integral equation, the first term gives the contribution of the monopole sources, and the second one gives the dipole sources contribution. The normal derivative pointing away from the upper layer D_0 (see Figure 2.2.1) is given by $\partial_n = \boldsymbol{n}\cdot\nabla$. This integral, for all $\boldsymbol{x}^r$ and $\boldsymbol{x}^s$, represents the seismic data from which, it is assumed, the incident field has been removed, and which are to be transformed to the double Radon domain. Before the transformations are applied, some approximations are introduced.

For large values of s, which is equivalent to a high frequency approximation, the reflectors are assumed to be locally plane. This is expressed by relating the incident and scattered field as

$$\begin{aligned} \hat{p}^{sct}(x,x^s) &= \eta\, \hat{p}^{inc}(x,x^s), \quad x \in S \\ \partial_n \hat{p}^{sct}(x,x^s) &= \zeta\, \partial_n \hat{p}^{inc}(x,x^s), \quad x \in S . \end{aligned} \tag{2.2.7}$$

The reflection coefficients $\eta\,(x, x-x^s)$ and $\zeta(x, x-x^s)$, which are s-independent, depend on the absolute position of the reflector x and on the relative position with respect to source $x-x^s$: at each point $x \in S$, the reflection coefficients η and ζ depend on the direction vector $x-x^s$ (see Figure 2.2.1). Since the actual values of the reflection coefficients are not of importance for migration, their behaviour during double Radon transform and imaging will not be investigated.

Substitution of the locally plane reflector approximation, equation 2.2.7, into the scattered field representation, equation 2.2.6, leads to

$$\hat{p}^{sct}(x^r,x^s) = \hat{W} \iint_{x \in S} \left[\zeta\, \hat{G}_0(x^r-x)\, \partial_n\left(\hat{G}_0(x-x^s)\right) - \eta\, \partial_n\left(\hat{G}_0(x^r-x)\right) \hat{G}_0(x-x^s) \right] dS. \tag{2.2.8}$$

The normal derivative operating on Green's functions (equation 2.2.4) is derived as

$$\partial_n\left(\hat{G}_0\right) = -\frac{s}{c_0}\, \hat{G}_0 \left(1 + \frac{c_0}{s\,|x|}\right) \partial_n |x| . \tag{2.2.9}$$

When the normal derivative of the Green's function is substituted into equation 2.2.8, the scattered field representation becomes

$$\hat{p}^{sct}(x^r,x^s) = \frac{s}{c_0}\, \hat{W} \iint_{x \in S} \hat{A}\, \hat{G}_0(x-x^r)\, \hat{G}_0(x-x^s)\, dS , \tag{2.2.10}$$

with the amplitude function $\hat{A} = \hat{A}\,(x, x-x^r, x-x^s)$ given by

$$\hat{A} = \eta \left(1 + \frac{c_0}{s\left|x-x^r\right|}\right) \partial_n \left|x-x^r\right| - \zeta \left(1 + \frac{c_0}{s\left|x-x^s\right|}\right) \partial_n \left|x-x^s\right| . \tag{2.2.11}$$

In equation 2.2.10, the scattered field is represented as an integral over the source and the receiver related Green's functions, and the amplitude function $\hat{A}$, which is given by equation

2.2.11. The importance of expressing the scattered field with these equations is that the function $\hat{A}$ becomes independent of s as the high frequency approximations, that is $|s| \to \infty$, are made to solve the integrals. The scattered field, as expressed by equation 2.2.10, is now subjected to two Radon transforms, with respect to both receiver coordinates and source coordinates.

2.3 TRANSFORM WITH RESPECT TO RECEIVER COORDINATES

The transform with respect to horizontal receiver coordinates x_1^r, x_2^r is achieved through a spatial Fourier transform applied to the scattered field with the transform parameter α^r as

$$\tilde{p}^{sct}(x_3^r, x^s; s\alpha^r) = \int\int_{-\infty}^{\infty} \hat{p}^{sct}(x^r, x^s)\, exp\left(is\,\alpha_1^r x_1^r + is\,\alpha_2^r x_2^r\right) dx_1^r\, dx_2^r . \tag{2.3.1}$$

In terms of the standard Fourier transformation, the real transform parameter is $s\alpha^r = \{s\alpha_1^r, s\alpha_2^r\}$, which is convenient for the mathematical derivation while operating in the Laplace domain. Since s is real, in the further analysis α_1^r and α_2^r are also taken to be real; only after deriving the Radon transform equations for both receiver and source coordinates, they will be transformed to the ray parameter through $\alpha^r \to -ip$, similarly to transforming the Laplace parameter into frequency. Application of the Fourier transform to the scattered field in equation 2.2.10, change of the order of integration, substitution of the source related Green's function by equation 2.2.4, and multiplication by $exp+\left(is\,\alpha_1^r x_1 + is\,\alpha_2^r x_2\right) \cdot exp-\left(is\,\alpha_1^r x_1 + is\,\alpha_2^r x_2\right)$, leads to

$$\tilde{p}^{sct}(x_3^r, x^s; s\alpha^r) = \frac{s}{c_0}\hat{W} \int\int_{x \in S} \tilde{B}\, \hat{G}_0(x - x^s)\, exp\left(is\,\alpha_1^r x_1 + is\,\alpha_2^r x_2\right) dS , \tag{2.3.2}$$

where the function $\tilde{B}$ is given by

$$\tilde{B} = \int\int_{-\infty}^{\infty} \frac{\hat{A}}{4\pi|x - x^r|}\, exp\left\{-s\left[i\alpha_1^r\left(x_1 - x_1^r\right) + i\alpha_2^r\left(x_2 - x_2^r\right) + \frac{|x - x^r|}{c_0}\right]\right\} dx_1^r\, dx_2^r . \tag{2.3.3}$$

Equation 2.3.2 defines the scattered field with the spatial Fourier transform applied to the receiver coordinates. The rest of this section is devoted to solving the integrals in the expression for the function $\tilde{B}$ in equation 2.3.3. De Hoop (1960, 1988) presented a technique for solving the integrals of the same type as 2.3.3 in his presentation of the modified Cagniard technique, which involves the manipulation of the integrand until it can be recognized as the Laplace transform of a certain function in time. The derivation which follows is carried out along the same lines and applying similar manipulations, and it will be done here in five steps:

1) Introduce polar coordinates, and variables of integration y^r, z^r.
2) Deform the imaginary y^r-axis into the steepest descent contour τ^r.
3) Change the order of integration $dz^r, d\tau^r \rightarrow d\tau^r, dz^r$.
4) Introduce the transformation $z^r \rightarrow \psi^r$.
5) Apply the high frequency approximation.

1) Introduce polar coordinates, and variables of integration y^r, z^r.

To solve the integrals in equation 2.3.3, the integration surface has to be deformed to force the expression in the square brackets in the exponent to become real. For that purpose, polar coordinates are introduced in the (α_1^r, α_2^r) plane as

$$\alpha_1^r = k^r \cos(\theta^r)$$
$$\alpha_2^r = k^r \sin(\theta^r), \text{ with} \qquad (2.3.4)$$
$$k^r = \sqrt{\left(\alpha_1^r\right)^2 + \left(\alpha_2^r\right)^2},$$

where $0 \le k^r < \infty$, and $0 \le \theta^r < 2\pi$. Also, the variables of integration in equation 2.3.3, x_1^r, x_2^r, are replaced by y^r, z^r through

$$x_1 - x_1^r = -iy^r \cos\theta^r - z^r \sin\theta^r$$
$$x_2 - x_2^r = -iy^r \sin\theta^r + z^r \cos\theta^r, \text{ with} \qquad (2.3.5)$$
$$\left(x_1 - x_1^r\right)^2 + \left(x_2 - x_2^r\right)^2 = \left(z^r\right)^2 - \left(y^r\right)^2.$$

To complete the transformation, the Jacobian is calculated as (see Appendix A.1)

$$dx_1^r\, dx_2^r = -i\, dy^r dz^r, \text{ and}$$
$$i\,\alpha_1^r \left(x_1 - x_1^r\right) + i\,\alpha_2^r \left(x_2 - x_2^r\right) = k^r y^r. \qquad (2.3.6)$$

Accordingly, the limits of integration change as

$$\iint_{-\infty}^{\infty} dx_1^r\, dx_2^r \rightarrow -\int_{-\infty}^{\infty} dz^r \int_{-i\infty}^{i\infty} i\, dy^r. \qquad (2.3.7)$$

With these transformations, as shown in Appendix A.1, the function $\widetilde{B}$ becomes

$$\widetilde{B} = \frac{1}{4\pi i} \int_{-\infty}^{\infty} dz^r \int_{-i\infty}^{i\infty} \frac{\widehat{A}}{R^r} \exp\left\{-s\left[k^r y^r + \frac{R^r}{c_0}\right]\right\} dy^r, \tag{2.3.8}$$

where

$$R^r = \left[\left(z^r\right)^2 + \left(x_3 - x_3^r\right)^2 - \left(y^r\right)^2\right]^{\frac{1}{2}}. \tag{2.3.9}$$

The choice of the new variables y^r, z^r has conveniently enabled the introduction of R^r, which later will be shown to be the position vector. The unwanted property of equation 2.3.8 is the integration along the imaginary axis; to avoid it, the integrand in the second integral in equation 2.3.8 will be analytically continued into the right half of the complex y^r-plane, away from the imaginary axis.

2) Deform the imaginary y^r-axis into the steepest descent contour τ^r.

As the integrand of equation 2.3.8 is extended in the complex y^r-plane, it needs to be kept single-valued. For that purpose, the branch cuts for the square root expression R^r are introduced as

$$\left[\left(z^r\right)^2 + \left(x_3 - x_3^r\right)^2\right]^{\frac{1}{2}} < \left|Re\left(y^r\right)\right| < \infty, \quad \text{and} \quad Im\left(y^r\right) = 0. \tag{2.3.10}$$

This is shown in Figure 2.3.1, for $\left(z^r\right)^2 + \left(x_3 - x_3^r\right)^2 = a^2$. When $|a| < y^r$, the argument of the square root becomes negative, and that is the range that has to be avoided. Also, $Re(R^r)$ is taken

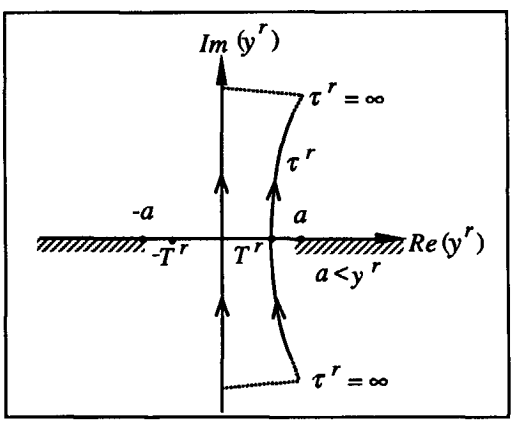

Fig.2.3.1: The branch cuts and the contours of integration in the complex y^r plane

to be positive in the entire cut y^r-plane. The imaginary y^r-axis is then deformed into a steepest descent contour τ^r which satisfies inequality 2.3.10, defined as

$$\tau^r = k^r y^r + \frac{R^r}{c_0}, \tag{2.3.11}$$

where τ^r is real and positive. The contour, shown in Figure 2.3.1 in the right half of the y^r-plane, is a branch of a hyperbola, and the integration along the imaginary y^r-axis will be replaced by the integration along τ^r. This hyperbolic path is composed of two complex conjugate branches, $y^r = y_1^r$ and $y^r = y_1^{r*}$, where * denotes complex conjugation. The parametric representation for y^r is obtained when R^r in equation 2.3.11 is substituted by equation 2.3.9 and the resulting equation solved for y^r, leading to

$$y_{1,2}^r = \frac{\tau^r k^r}{\left(k^r\right)^2 + \frac{1}{c_0^2}} \pm i \frac{\frac{1}{c_0}\sqrt{\left(\tau^r\right)^2 - \left(T^r(z^r)\right)^2}}{\left(k^r\right)^2 + \frac{1}{c_0^2}}, \quad \text{thus } y_2^r = y_1^{r*}, \tag{2.3.12}$$

where $T^r(z^r)$ is given by

$$T^r(z^r) = \sqrt{\left(k^r\right)^2 + \frac{1}{c_0^2}}\sqrt{\left(z^r\right)^2 + \left(x_3 - x_3^r\right)^2}. \tag{2.3.13}$$

The hyperbolic path given by equation 2.3.12 is symmetric with respect to the real y^r-axis, and crosses it at $\tau^r = T^r(z^r)$, that is between the two branch points $-a$ and $+a$, as shown in Figure 2.3.1.

The Jacobian of this transformation, derived in Appendix A.2, is

$$\frac{\partial y_1^r}{\partial \tau^r} = i \frac{R^r}{\sqrt{\left(\tau^r\right)^2 - \left(T^r(z^r)\right)^2}}. \tag{2.3.14}$$

The original path of integration along the imaginary y^r- axis is replaced by the integration along the contour $y_{1,2}^r$, which is joined to the imaginary y^r- axis with circular arcs at infinity. The contribution to the integral from the circular arcs vanishes (Jordan's lemma), and the integration is now performed along the two branches $y_{1,2}^r$ only. The change of the limits of integration from y^r to τ^r is explained in Figure 2.3.2: in y^r coordinates, the integral can reach

$\pm i\infty$ along $Im(y^r)$, but in τ^r coordinates the lowest limit on the τ^r contour is $T^r(z^r)$. Thus, after the deformation, the integral in equation 2.3.8 changes into

$$\widetilde{B} = \frac{1}{4\pi} \int_{-\infty}^{\infty} dz^r \int_{T^r(z^r)}^{\infty} \frac{2\,Re\left\{\widehat{A}(z^r,y^r)\right\}}{\sqrt{\left(\tau^r\right)^2 - \left(T^r(z^r)\right)^2}} \exp\left(-s\tau^r\right) d\tau^r , \qquad (2.3.15)$$

where the contributions of $\widehat{A}(z^r,y_1^r)$ and $\widehat{A}(z^r,y_1^{r\,*})$ are replaced by $2\,Re\left\{\widehat{A}(z^r,y_1^r)\right\}$, based on Schwartz reflection principle.

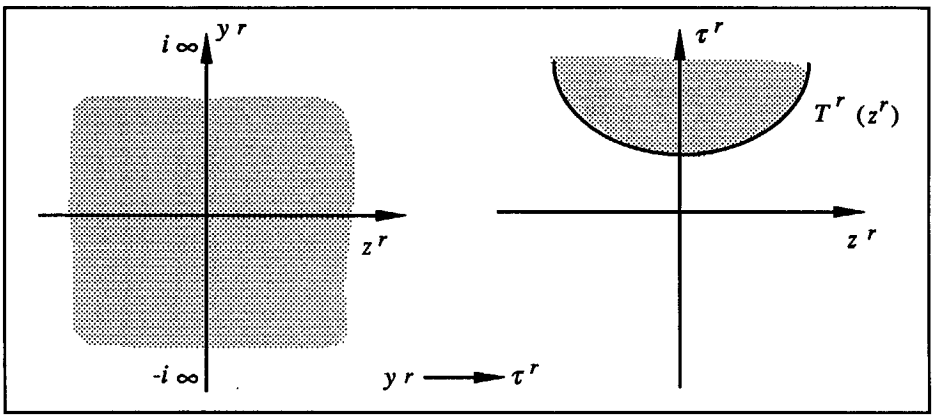

Fig.2.3.2: The transformation from y^r to τ^r.

3) Change the order of integration $dz^r, d\tau^r \rightarrow d\tau^r, dz^r$.

The order of integration in equation 2.3.15 is interchanged as explained in Figure 2.3.3, where the new limits of integration Z^r and T_0^r follow from equation 2.3.13; the equation 2.3.13 solved for z^r leads to Z^r

$$Z^r(\tau^r) = \sqrt{\frac{\left(\tau^r\right)^2}{\left(k^r\right)^2 + \frac{1}{c_0^2}} - \left(x_3 - x_3^r\right)^2} \quad , \qquad (2.3.16)$$

and for $z^r = 0$ in equation 2.3.13, T_0^r follows as

$$T_0^r = T^r(z^r = 0) = \sqrt{\left(k^r\right)^2 + \frac{1}{c_0^2}}\ \left(x_3 - x_3^r\right) . \qquad (2.3.17)$$

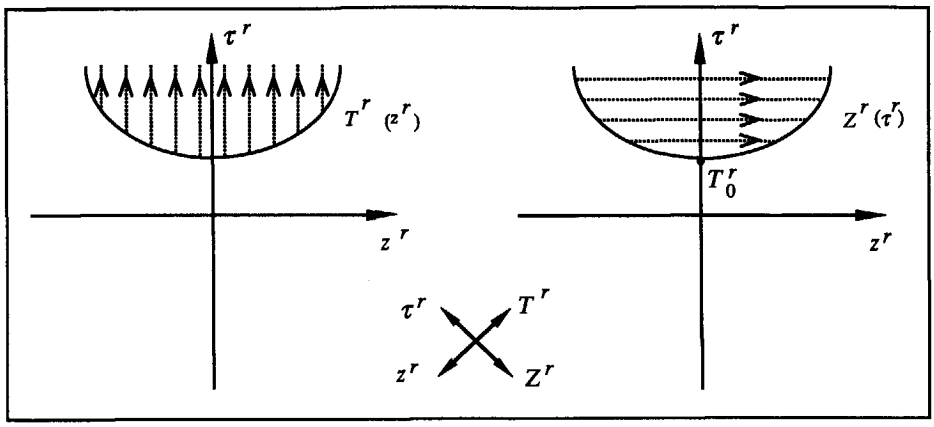

Fig.2.3.3: The change of the order of integration

With this change of the order of integration, equation 2.3.15 becomes

$$\widetilde{B} = \frac{1}{2\pi} \int_{T_0^r}^{\infty} exp\left(-s\tau^r\right) d\tau^r \int_{-Z^r(\tau^r)}^{Z^r(\tau^r)} \frac{Re\left\{\widehat{A}(z^r, y^r)\right\}}{\sqrt{\left(\tau^r\right)^2 - \left(T^r(z^r)\right)^2}} \, dz^r \,. \tag{2.3.18}$$

4) Introduce the transformation $z^r \rightarrow \psi^r$.

To be able to evaluate the second integral in the right-hand side of equation 2.3.18 in the high frequency approximation, a change of integration variables is introduced as

$$z^r = Z^r(\tau^r) \, sin \, \psi^r. \tag{2.3.19}$$

The Jacobian for this transformation $z^r \rightarrow \psi^r$ is

$$dz^r = Z^r(\tau^r) \, cos \, \psi^r d\psi^r, \tag{2.3.20}$$

and the new limits of integration follow from equation 2.3.19 as

$$\int_{-Z^r(\tau^r)}^{Z^r(\tau^r)} dz^r \rightarrow \int_{-\pi/2}^{\pi/2} d\psi^r \,. \tag{2.3.21}$$

After substitution of equation 2.3.19 into equation 2.3.13, the square root in equation 2.3.18 becomes

$$\sqrt{\left(\tau^r\right)^2-\left(T^r(z^r)\right)^2}=\sqrt{\left(k^r\right)^2+\frac{1}{c_0^2}}\cdot Z^r(\tau^r)\cos(\psi^r). \tag{2.3.22}$$

With these transformations, the expression for the function $\widetilde{B}$ (equation 2.3.18) becomes

$$\widetilde{B}=\frac{1}{2\pi\sqrt{\left(k^r\right)^2+\frac{1}{c_0^2}}}\int_{T_0^r}^{\infty}exp\left(-s\tau^r\right)d\tau^r\int_{-\pi/2}^{\pi/2}Re\left\{\widehat{A}(z^r,y_1^r)\right\}d\psi^r. \tag{2.3.23}$$

5) Apply the high frequency approximation.

By rewriting the second integral in equation 2.3.23 as $f(\tau)$, the integration by parts can be applied to the remaining integral. Choosing $u=f(\tau)$, and $dv=exp\left(-s\tau^r\right)d\tau^r$, integration by parts leads to

$$uv-\int v\,du=-\frac{f(\tau)}{s}exp\left(-s\tau^r\right)\Big|_{T_0^r}^{\infty}+\frac{1}{s}\int_{T_0^r}^{\infty}\frac{\partial}{\partial\tau}f(\tau)\,exp\left(-s\tau^r\right)d\tau^r. \tag{2.3.24}$$

Subsequent integrations by parts will increase the power of s in the denominator to $1/s^2$, $1/s^3$, and so on. Then, in the high frequency approximation, that is for $s\rightarrow\infty$, the contribution of integral in equation 2.3.24 becomes zero, leaving only the first part of equation 2.3.24 as the solution. When the limits of the integral are substituted, that is when τ is replaced by T_0^r, the amplitude $\widehat{A}$ does not depend of z^r ($z^r=0$ at T_0^r) or y^r any more, thus it is not a function of ψ^r any more, and the integral $f(\tau)$ can be solved, leading to

$$-\frac{f(\tau)}{s}exp\left(-s\tau^r\right)\Big|_{T_0^r}^{\infty}=\frac{exp\left(-sT_0^r\right)}{s}\widehat{A}_{|\,z^r=0,\;\tau^r=T_0^r}\cdot\int_{-\pi/2}^{\pi/2}d\psi^r. \tag{2.3.25}$$

Substitution of this result into equation 2.3.23 leads to

$$\widetilde{B}=\frac{exp\left(-sT_0^r\right)}{2s\gamma_0^r}\widehat{A}_{|\,z^r=0,\;\tau^r=T_0^r}, \tag{2.3.26}$$

where the square root in equation 2.3.23 is replaced by γ_0^r using equation 2.3.4 as

$$\gamma_0^r = \sqrt{\left(\alpha_1^r\right)^2 + \left(\alpha_2^r\right)^2 + \frac{1}{c_0^2}} \,. \tag{2.3.27}$$

Using this expression for γ_0^r and equation 2.3.17 for T_0^r, the new expression for T_0^r is established as

$$T_0^r = \gamma_0^r \left(x_3 - x_3^r\right). \tag{2.3.28}$$

Thus, equations 2.3.26 - 2.3.28 give the solution for the function $\widetilde{B}$, which was expressed as a double integral in equation 2.3.3.

In order to evaluate the value of $\widehat{A}$ for high frequencies, the parameter s in equation 2.2.11 is allowed to approach infinity, leading to

$$\widehat{A} = \eta \, \partial_n \left| x - x^r \right| - \zeta \, \partial_n \left| x - x^s \right|. \tag{2.3.29}$$

The normal derivative operating on $\left|x - x^r\right|$, as derived in Appendix A.3, is given by

$$\partial_n \left| x - x^r \right| = \frac{-\partial_1 h \cdot \left(x_1 - x_1^r\right) - \partial_2 h \cdot \left(x_2 - x_2^r\right) + \left(x_3 - x_3^r\right)}{\left|x - x^r\right| \sqrt{\left(\partial_1 h\right)^2 + \left(\partial_2 h\right)^2 + 1}} \,. \tag{2.3.30}$$

Using $z^r = 0$ in equations 2.3.5, and substituting it into the expression for R^r in equation 2.3.9, a new expression is obtained showing that R^r is the position vector

$$R^r = \left[\left(x_1 - x_1^r\right)^2 + \left(x_2 - x_2^r\right)^2 + \left(x_3 - x_3^r\right)^2\right]^{\frac{1}{2}} = \left|x - x^r\right|. \tag{2.3.31}$$

Another expression for R^r is obtained by substituting $\tau^r = T_0^r$ in equation 2.3.11, as shown in Appendix A.3, leading to

$$R^r = \frac{x_3 - x_3^r}{c_0 \gamma_0^r}. \tag{2.3.32}$$

Using the expressions for R^r and equations 2.3.5 and 2.3.12 in a manner shown in the Appendix A.3 the amplitude $\widehat{A}$ becomes

$$\widehat{A}\big|_{z^r=0,\,\tau^r=T_0^r} = c_0\eta\,\frac{i\,\alpha_1^r\partial_1 h + i\,\alpha_2^r\partial_2 h + \gamma_0^r}{\sqrt{(\partial_1 h)^2+(\partial_2 h)^2+1}} - \zeta\,\partial_n\left|x-x^s\right|, \tag{2.3.33}$$

for $s\to\infty$.

After the horizontal source coordinates have been transformed to the α-domain as well, the expressions 2.3.33 for $\widehat{A}$, and 2.3.26 for $\widetilde{B}$, will be included for the complete solution of the double Radon transform.

2.4 TRANSFORM WITH RESPECT TO SOURCE COORDINATES

The procedure for the transform with respect to source coordinates is equivalent to the receiver coordinates transform. Only the main steps are repeated here and applied to the source coordinates.

The Fourier transform applied to the scattered field $\tilde{p}^{sct}$ (equation 2.3.2.) with respect to x_1^s, x_2^s is expressed as

$$\tilde{\tilde{p}}^{sct}(x_3^r,x_3^s;s\alpha^r,s\alpha^s) = \int\int_{-\infty}^{\infty}\tilde{p}^{sct}(x_3^r,x^s;s\alpha^r)\,exp\left(is\,\alpha_1^s x_1^s + is\,\alpha_2^s x_2^s\right)dx_1^s\,dx_2^s. \tag{2.4.1}$$

Solution of this transformation of the scattered field $\tilde{p}^{sct}$ yields

$$\tilde{\tilde{p}}^{sct}(x_3^r,x_3^s;s\alpha^r,s\alpha^s) = \frac{s}{c_0}\widehat{W}\iint_{x\in S}\tilde{\tilde{C}}\,exp\left(is\left(\alpha_1^r+\alpha_1^s\right)x_1 + is\left(\alpha_2^r+\alpha_2^s\right)x_2\right)dS, \tag{2.4.2}$$

where the function $\tilde{\tilde{C}}$ can be written, equivalently to $\tilde{B}$ in equation 2.3.3, as

$$\tilde{\tilde{C}} = \int\int_{-\infty}^{\infty}\frac{\tilde{B}}{4\pi\left|x-x^s\right|}\,exp\left\{-s\left[i\alpha_1^s\left(x_1-x_1^s\right)+i\alpha_2^s\left(x_2-x_2^s\right)+\frac{\left|x-x^s\right|}{c_0}\right]\right\}dx_1^s\,dx_2^s. \tag{2.4.3}$$

Following again the same procedure which was used to obtain $\tilde{B}$ in equation 2.3.26, the value for $\tilde{\tilde{C}}$ is found for $s\to\infty$ as

$$\tilde{\tilde{C}} = \frac{exp\left(-sT_0^s\right)}{2s\gamma_0^s}\,\tilde{B}_{|\,z^s=0,\,\tau^s=T_0^s}, \tag{2.4.4}$$

where γ_0^s and T_0^s have definitions similar to their equivalent functions for the receiver coordinates

$$\gamma_0^s = \sqrt{\left(\alpha_1^s\right)^2 + \left(\alpha_2^s\right)^2 + \frac{1}{c_0^2}}\,, \tag{2.4.5}$$

and

$$T_0^s = \gamma_0^s\left(x_3 - x_3^s\right). \tag{2.4.6}$$

Substitution of $\tilde{B}$ from equation 2.3.26 yields

$$\tilde{\tilde{C}} = \frac{exp\left[-s\left(T_0^r + T_0^s\right)\right]}{2s\gamma_0^r s\gamma_0^s}\,\hat{A}_{|z^r=0,\,\tau^r=T_0^r\,;\,z^s=0,\,\tau^s=T_0^s}. \tag{2.4.7}$$

The new expression for $\hat{A}$ is obtained by further developing equation 2.3.33 for $\partial_n\left|x - x^s\right|$ as

$$\hat{A}_{|\,z^r=0,\,\tau^r=T_0^r\,;\,z^s=0,\,\tau^s=T_0^s} = \frac{E}{\sqrt{\left(\partial_1 h\right)^2 + \left(\partial_2 h\right)^2 + 1}}, \tag{2.4.8}$$

where the function E, which is independent of s, is given by

$$E = c_0\eta\left[i\,\alpha_1^r\partial_1 h + i\,\alpha_2^r\partial_2 h + \gamma_0^r\right] - c_0\zeta\left[i\,\alpha_1^s\partial_1 h + i\,\alpha_2^s\partial_2 h + \gamma_0^s\right]. \tag{2.4.9}$$

The functions η and ζ, which were introduced as functions of direction vectors x and $x-x^s$, are now dependent on horizontal coordinates of the interface x_1, x_2, and on vertical coordinate of the receiver and source x_3^r, x_3^s.

To calculate the final expression for the scattered field in the double α-domain, the following operations need to be done. The expressions for $\tilde{\tilde{C}}$ in equation 2.4.7 and for $\hat{A}$ in equation 2.4.8 are substituted into expression for the scattered field, equation 2.4.1. The variable of integration dS in the surface integral is changed into $dx_1\,dx_2$ as

$$\iint_{x\,\in S} dS \;\rightarrow\; \iint_{x\,\in S} \sqrt{\left(\partial_1 h\right)^2 + \left(\partial_2 h\right)^2 + 1}\;dx_1\,dx_2\,. \tag{2.4.10}$$

These substitutions lead to

$$\tilde{\tilde{p}}^{sct}(x_3^r,x_3^s;s\alpha^r,s\alpha^s)=\frac{\hat{W}}{4sc_0\gamma_0^r\gamma_0^s}\iint_{x\in S}E\exp\left[-s\left(T_0^r+T_0^s\right)\right]\cdot$$

$$\exp\left[is\left(\alpha_1^r+\alpha_1^s\right)x_1+is\left(\alpha_2^r+\alpha_2^s\right)x_2\right]\,dx_1\,dx_2\ . \tag{2.4.11}$$

The important result obtained with this equation is that, according to equation 2.3.28 and 2.4.6, T_0^r and T_0^s depend only on vertical coordinates, while the argument in the second exponent in equation 2.4.11 includes horizontal coordinates only. Thus, with the double transform over horizontal coordinates, the horizontal phase and the vertical phase of the data are separated. The importance of this result will become evident in the next chapter, when imaging is discussed.

2.5 RAY PARAMETER - FREQUENCY DOMAIN

The derivation of the double Radon transform equations was done in the Laplace domain. By allowing $s\rightarrow -i\omega$, the derived s-dependent functions can be transformed into frequency domain. If two functions in the Laplace domain are equal for real s, and $s\rightarrow\infty$, as

$$\hat{f}(x,s)=\hat{g}(x,s)\ ,\quad \text{real}\ s,\quad s\rightarrow\infty\ , \tag{2.5.1}$$

then their counterparts in the frequency domain also are equal for real ω, and $\omega\rightarrow\infty$ as

$$\hat{f}(x,-i\omega)=\hat{g}(x,-i\omega)\ ,\quad \text{real}\ \omega,\quad \omega\rightarrow\infty\ . \tag{2.5.2}$$

It follows that the derived expression for the scattered field, given by 2.4.11, holds not only for real $s\rightarrow\infty$, but also for $s\rightarrow -i\omega$, and for $\omega\rightarrow\infty$, provided $s\alpha^r$ and $s\alpha^s$ are kept real-valued.

At this point the horizontal offset coordinates, which are the local coordinates within each shot gather, are introduced instead of absolute receiver coordinates as

$$\begin{aligned}x_1^o&=x_1^r-x_1^s\\ x_2^o&=x_2^r-x_2^s\ .\end{aligned} \tag{2.5.3}$$

The coordinates are changed in the spatial Fourier domain also: ray parameters $\boldsymbol{p}^o=\{p_1^o,p_2^o\}$ and $\boldsymbol{p}^s=\{p_1^s,p_2^s\}$ are introduced to replace original α-coordinates as

$$p^o = i\,\alpha^r$$
$$p^s = i\left(\alpha^r + \alpha^s\right). \tag{2.5.4}$$

These new coordinates, x_1^o and x_2^o, and p^o and p^s, are introduced into equation 2.4.11 and into expressions for T_0^r and T_0^s in equations 2.3.28 and 2.4.6, and s is allowed to approach $-i\omega$, leading to the following expression for the scattered field

$$\tilde{\tilde{p}}^{sct}(x_3^r, x_3^s; -\omega p^o, \omega(p^o - p^s)) = -\frac{\widehat{W}}{4i\omega c_0 q_0^r q_0^s} \iint_{x \in S} E\, exp\left[-i\omega p_1^s x_1 - i\omega p_2^s x_2\right] \cdot$$
$$exp\left\{i\omega\left[q_0^r\left(x_3 - x_3^r\right) + q_0^s\left(x_3 - x_3^s\right)\right]\right\} dx_1\, dx_2\,, \tag{2.5.5}$$

for $\omega \to \infty$.

The new expression for E follows from introducing the new coordinates into equation 2.4.9 as

$$E = c_0\eta\left[p_1^o \partial_1 h + p_2^o \partial_2 h + q_0^r\right] + c_0\zeta\left[\left(p_1^o - p_1^s\right)\partial_1 h + \left(p_2^o - p_2^s\right)\partial_2 h + q_0^s\right]. \tag{2.5.6}$$

By introducing the ray parameters into equations 2.3.27 and 2.4.5 for γ_0^r and γ_0^s, the new expressions for q_0^r and q_0^s in equation 2.5.5 are recognized as vertical slowness functions, with respect to receiver and source coordinates respectively

$$q_0^r = \sqrt{\frac{1}{c_0^2} - \left(p_1^o\right)^2 - \left(p_2^o\right)^2}$$
$$q_0^s = \sqrt{\frac{1}{c_0^2} - \left(p_1^s - p_1^o\right)^2 - \left(p_2^s - p_2^o\right)^2}\,. \tag{2.5.7}$$

In equation 2.5.5, the scattered field is still a function of the different vertical source and receiver coordinates. For that reason the sources and receivers are brought to the same level by performing a phase shift $exp\left[i\omega q_0^r(x_3^r - x_3^s)\right]$. Also, a scaled frequency domain filter $-4i\omega c_0 q_0^r q_0^s$ is applied to compensate for the scaling factor in front of the integral in equation 2.5.5. These two corrections are introduced together as

$$E' = -4i\omega c_0 q_0^r q_0^s exp\left[i\omega q_0^r (x_3^r - x_3^s)\right]. \tag{2.5.8}$$

With this correction, the explicit dependence of the scattered field on x_3^r and x_3^s will be omitted in the notation. Thus, the scattered field becomes

$$\tilde{\tilde{p}}^{sct}(\boldsymbol{p}^o,\boldsymbol{p}^s) = E^{'}\widehat{W}\iint_{x\in S} E\exp\left[i\omega\left(q_0^r+q_0^s\right)\left(x_3-x_3^s\right)-i\omega p_1^s x_1-i\omega p_2^s x_2\right]dx_1dx_2. \quad (2.5.9)$$

Using equation 2.2.1, which describes the vertical interface coordinate x_3 as a function h of its horizontal coordinates x_1 and x_2, the surface integral over surface S is written as a double integral over its horizontal coordinates, where the variables of integration are allowed to approach $\pm\infty$. With this change, the final expression for scattered field in the double Radon domain is reached as

$$\tilde{\tilde{p}}^{sct}(\boldsymbol{p}^o,\boldsymbol{p}^s) = E^{'}\widehat{W}\int_{-\infty}^{\infty}\int E\exp\left\{i\omega\left[q_0\left(h-x_3^s\right)-p_1^s x_1-p_2^s x_2\right]\right\}dx_1\,dx_2\ , \quad (2.5.10)$$

where the function q_0 is defined as sum of the vertical slowness functions

$$q_0 = q_0^r + q_0^s. \quad (2.5.11)$$

Similarly to equation 2.4.11, these two equations show the separation of the vertical phase and the horizontal phase of the data: the first part of the exponent in equation 2.5.10 contains the vertical slowness and the vertical coordinates, and the second part contains the horizontal slowness and the horizontal coordinates. Also, the vertical phase term is now recognized as the frequency domain equivalent of the vertical travel time (Diebold and Stoffa, 1981).

2.6 THE DOUBLE RADON TRANSFORMED DOMAIN

2.6.1 From 3D to 2.5D and the 2D problem

The Double Radon transformation was derived for 3D seismic data, the three dimensions being the two horizontal coordinates x_1 and x_2, and the temporal coordinate t. In practice, it is often assumed that the seismic profile was measured along a strike line in the direction of x_1, so that $x_2 = 0$. Since the source and the receiver can each be approximated by a point, and the seismic data are measured in the 2D configuration, the situation is called 2.5D (Bleistein, 1986). In that case, $x_1 = x$, and the scattered field in the double Radon domain is expressed as

$$\tilde{\tilde{p}}^{sct}(p^o,p^s) = E'\,\hat{W}\int_{-\infty}^{\infty} E\,exp\left\{i\omega\left[q_0\left(h-x_3^s\right)-p^s x\right]\right\}dx \quad , \tag{2.6.1}$$

with

$$q_0 = \sqrt{\frac{1}{c_0^2}-\left(p^o\right)^2} + \sqrt{\frac{1}{c_0^2}-\left(p^s-p^o\right)^2} \tag{2.6.2}$$

The expression 2.6.2 appears to be equivalent to the 3D expression in equation 2.5.10. The difference between the two is hidden in the frequency scaled filter in E', which in the 2.5D case is $8\pi\sqrt{-i\omega c_0 q_0^r q_0^s}$. For computer simulated data, the sources and the receivers are often given in a line configuration (2D problem), and the filter becomes $-8\pi i\omega\sqrt{q_0^r q_0^s}$.

The derivation of the 2.5D or 2D expression of the double Radon transform becomes rather tedious with the steepest descent method, and it is shown in Fokkema and van den Berg (1992). This derivation becomes easier with the stationary phase method (for stationary phase method, see Bleistein, 1984). The derivation of the double Radon transform for the 2.5D case using stationary phase method is shown in Vissinga (1992).

For most practical situations, either 2D (synthetic data) or 2.5D (field data) expressions would be used. The theory which follows in this thesis is applicable to either 2D or 2.5D situations, depending on the frequency scaling filter only.

2.6.2 Implementation

The mathematical derivation of the double Radon transform was carried out in the Laplace domain for the temporal coordinate, and the spatial coordinates were transformed into the α-domain. In the final stage, the Laplace parameter was transformed into frequency, and the α-parameters were transformed into offset ray parameter and source ray parameter.

The actual implementation of the double Radon transform is done by temporal and spatial Fourier transforms directly. The double Radon transform is carried out in two steps, as indicated in the Figure 2.6.1. Practically, the first Radon transform is applied to shot gathers, and the coordinate x^o is transformed into p^o. After the data have been sorted into constant p^o-gathers, the second Radon transform is applied to the p^o-gathers, and the coordinate x^s is transformed into p^s.

It was recognized that an efficient algorithm for a τ-p transform can be achieved by applying two Fourier transforms, temporal and spatial, followed by an interpolation (Benoliel et al., 1987, Fokkema et al., 1992). The first Radon transform starts by applying a Fourier transform with respect to time to the measured scattered field $p^{sct}(x^o, x^s, t)$ as

$$\hat{p}^{sct}(x^o,x^s,\omega) = \int_{-\infty}^{\infty} p^{sct}(x^o,x^s,t)\,exp\left(i\,\omega\,t\right)dt \quad . \tag{2.6.3}$$

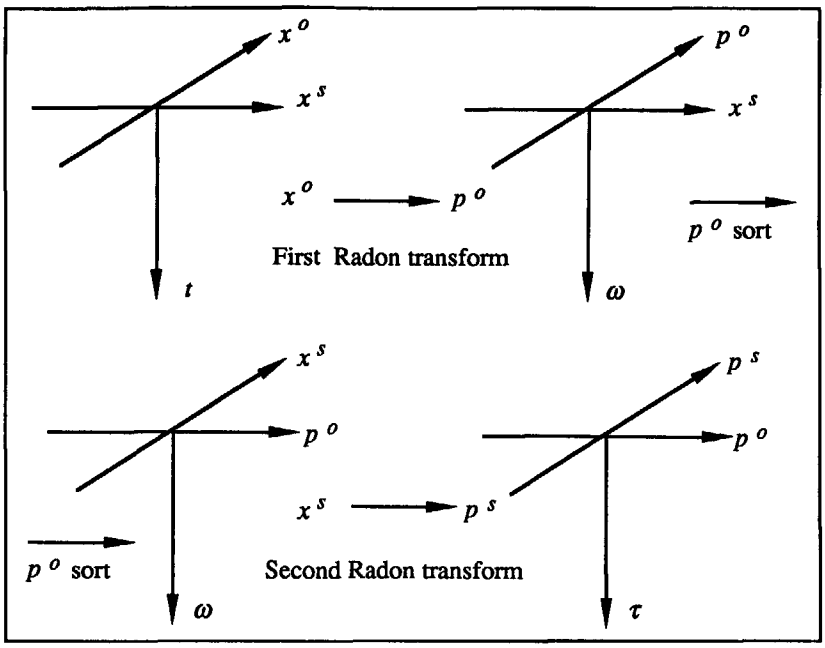

Fig.2.6.1: Implementation of the double Radon transform

The frequency dependent data are subjected to a spatial Fourier transform with respect to offset coordinate as

$$\tilde{\hat{p}}^{sct}(K_x^o, x^s, \omega) = \int_{-\infty}^{\infty} \hat{p}^{sct}(x^o, x^s, \omega)\, exp\left(-i K_x^o x^o\right) dx^o, \tag{2.6.4}$$

where $K_x^o = 2\pi k_x^o$. Using the projection slice theorem, the data are interpolated from a grid regular in K_x^o into a grid regular in p^o, using the equality $K_x^o = \omega p^o$ as

$$\tilde{\hat{p}}^{sct}(p^o, x^s, \omega) = \tilde{\hat{p}}^{sct}(K_x^o = \omega p^o, x^s, \omega). \tag{2.6.5}$$

For a conventional τ-p transform, it would be sufficient now to apply an inverse temporal Fourier transform and obtain the data as a function of the vertical travel time τ

$$\tilde{p}^{sct}(p^o, x^s, \tau) = \frac{1}{\pi} Re\left[\int_0^{\infty} \tilde{\hat{p}}^{sct}(p^o, x^s, \omega)\, exp\left(-i\omega t\right) \omega\, d\omega\right]. \tag{2.6.6}$$

For the double Radon transform, the data are kept in the frequency domain and sorted into common p^o - gathers for the second Radon transform. The transform is carried out by applying the second spatial Fourier transform, this time with respect to the horizontal source coordinate

$$\tilde{\tilde{P}}^{sct}(p^o,K_x^s,\omega) = \int_{-\infty}^{\infty} \tilde{\tilde{P}}^{sct}(p^o,x^s,\omega)\, exp\left(-iK_x^s x^s\right) dx^s. \tag{2.6.7}$$

Again, the projection slice theorem is applied to interpolate the data from the K_x^s grid to the p^s grid using $K_x^s = \omega p^s$ as

$$\tilde{\tilde{P}}^{sct}(p^o,p^s,\omega) = \tilde{\tilde{P}}^{sct}(p^o,K_x^s = \omega p^s,\omega). \tag{2.6.8}$$

At this point, the Double Radon transformed data in the frequency domain, as given by equation 2.6.1, are obtained. To transform frequency into vertical travel time, an inverse temporal Fourier transform is applied leading to

$$\tilde{\tilde{P}}^{sct}(p^o,p^s,\tau) = \frac{1}{\pi} Re\left[\int_0^{\infty} \tilde{\tilde{P}}^{sct}(p^o,p^s,\omega)\, exp\left(-i\omega t\right) \omega\, d\omega\right]. \tag{2.6.9}$$

Equations 2.6.3 - 2.6.9 are used for computer implementation. The execution of these equations for discrete data using fast Fourier transforms leads to the data set in the p^o - p^s - τ domain, which was also described by Vissinga (1992).

3

IMAGING IN THE DOUBLE RADON TRANSFORMED DOMAIN

3.1 INTRODUCTION

Imaging of the data in the double transformed Radon domain starts with the selection of the data along the imaging lines. As mentioned earlier, by double transforming the data to the Radon domain, the vertical phase (containing vertical slowness and vertical spatial coordinates) and the horizontal phase (containing horizontal slowness and horizontal spatial coordinates) of the data become separated. The imaging lines are determined by the vertical slowness function, which, in turn, restricts the possible values of the ray parameters to a particular combination of the p^o, p^s pairs. For a fixed value of the vertical slowness function, determined by the velocity of propagation through the layer of interest, the only possible combination of the p^o, p^s pairs is the one which belongs to the interface in question. For a particular value of p^o (the ray recorded at the receiver position), there are two possible corresponding values of p^s (the rays leaving the source), one updip and the other one downdip from the receiver position, depending on the dip of the interface. Thus, by fixing the vertical slowness function, a domain is selected which contains only the energy reflected from a particular interface. This energy is inverse Radon transformed once, giving the time image of the interface. The procedure is illustrated with a simple synthetic example.

The imaging is extended to the multi-interface case by introducing the RMS velocity function, rather than the interval velocity of a single layer. The background velocity function is obtained from the p^o - p^s transformed data, by exploiting the properties of the double transformed Radon domain. In the p^o - p^s domain, the data are discretized according to the local dip of the interface. This means that there is a domain in p^o - p^s space, where only energy reflected from horizontally layered interfaces is present. This domain is ideal for velocity analysis, since it satisfies the assumption of a horizontally layered earth. The τ-p velocity analysis described here employs the coherency calculation of the best fitting ellipse.

The double Radon transformed domain offers another possibility for migration of the data, which is carried out through frequency scaling in the domains of constant dip. The frequency scaling leads to an NMO-like operation which corrects for the phase differences caused by the elliptical and quasi-elliptical move-out.

3.2 SINGLE INTERFACE: CONSTANT VELOCITY

In chapter 2, the expression for the field scattered from an arbitrarily shaped interface and double transformed to the Radon domain, equation 2.6.1, was derived. For convenience, the integral representation of the scattered field and its slowness function are repeated here

$$\tilde{\tilde{p}}^{sct}(p^o,p^s,\omega) = E^{i}\,\hat{W}(\omega)\int_{-\infty}^{\infty} E\,exp\left\{i\omega\left[q_0 z - p^s x\right]\right\} dx \quad , \tag{3.2.1}$$

where $z = \left(h - x_3^s\right)$, with the slowness function

$$q_0 = \sqrt{\frac{1}{c_0^2} - \left(p^o\right)^2} + \sqrt{\frac{1}{c_0^2} - \left(p^s - p^o\right)^2} \quad . \tag{3.2.2}$$

In order to keep the slowness function real and the arguments of the square-root positive in equation 3.2.2, the maximum allowed values for the p^o and p^s range are

$$\begin{aligned} -\frac{1}{c_0} \le\ & p^o \le \frac{1}{c_0} \\ -\frac{1}{c_0} + p^o \le\ & p^s \le \frac{1}{c_0} + p^o \quad . \end{aligned} \tag{3.2.3}$$

This theoretically possible range of p^o and p^s values is shown in Figure 3.2.1 by the diamond shaped contour in the p^o - p^s plane. In the limiting case for the p^o value in equation 3.2.3, the limits for p^s become

$$p^s = \pm \frac{2}{c_0} \quad . \tag{3.2.4}$$

To proceed with the imaging, the slowness function is rewritten to express p^o explicitly. The solution of equation 3.2.2 for p^o indicates that two real solutions exist for each value of p^s and for real values of q_0, as

$$p^{o\pm} = \frac{p^s}{2} \pm \frac{q_0}{2} \frac{\sqrt{\frac{4}{c_0^2} - (p^s)^2 - (q_0)^2}}{\sqrt{(p^s)^2 + (q_0)^2}} \quad . \tag{3.2.5}$$

To keep the argument of the square root in the equation 3.2.5 positive and the solutions for p^o real, for a particular value of q_0, for example q_a, the values of p^s are restricted to the domain $\mathcal{D}(q_a)$, $p^s \in \mathcal{D}(q_a)$, where

$$\mathcal{D}(q_a) \quad : \quad (p^s)^2 \leq \frac{4}{c_0^2} - q_a^2. \tag{3.2.6}$$

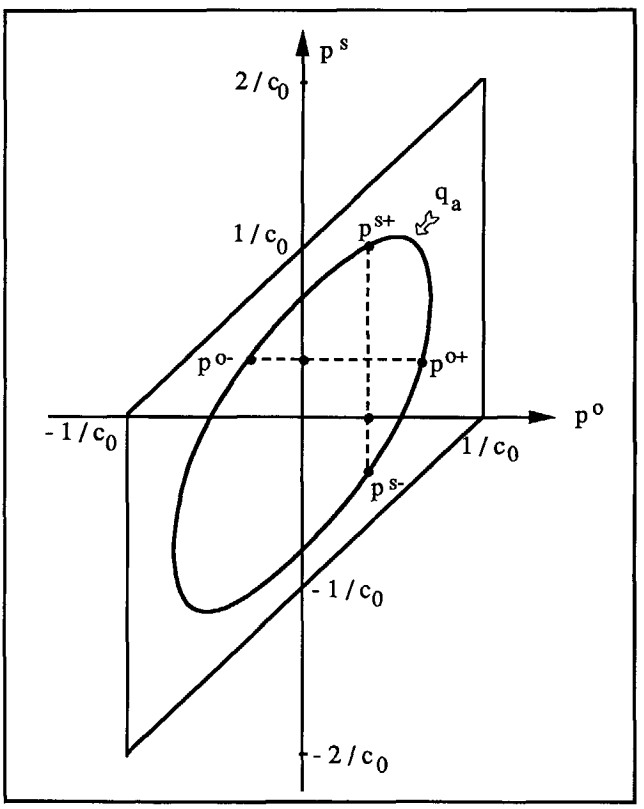

Fig.3.2.1: The theoretically possible range of p^o and p^s values. The imaging line q_a (a=1.85, and c_0=1.5 km/sec) has two solutions for p^o and two solutions for p^s.

The curve expressed in equation 3.2.5, for a chosen q_a, and for a particular velocity c_0, is called the imaging line and is shown in Figure 3.2.1. When extended to p^o - p^s -τ space, it

describes the imaging surface. Equation 3.2.5 restricts the values of p^s and p^o to a particular range, depending on the chosen value of q_0, and indicates that for each value of p^s, two values of p^o are possible. Also, the opposite holds: for each value of p^o, two values of p^s are possible. For each ray characterized by p^o, reflected from the interface and recorded at the receiver, two possible incident rays exist. These incident rays can be either updip or downdip from the receiver location, and the interface can be dipping either at a positive angle or at a negative angle, as indicated in Figure 3.2.2. The incident ray is not completely described by its p^s value. If the ray parameter of the downgoing ray is denoted by p^d, where $p^d = \pm (p^s - p^o)$, then for a fixed p^o value the p^s value characterizes either of rays $(p^s - p^o)$ or $(p^o - p^s)$. For a fixed value of p^s, two incident rays are possible, $(p^s - p^{o+})$ or $(p^s - p^{o-})$, and therefore two possible solutions for p^o exist, p^{o+} and p^{o-}, as indicated in Figure 3.2.3. This means that by selecting all p^o - p^s pairs characterized by q_a, the rays that could have been reflected from the interface are gathered, regardless of the shape of the interface.

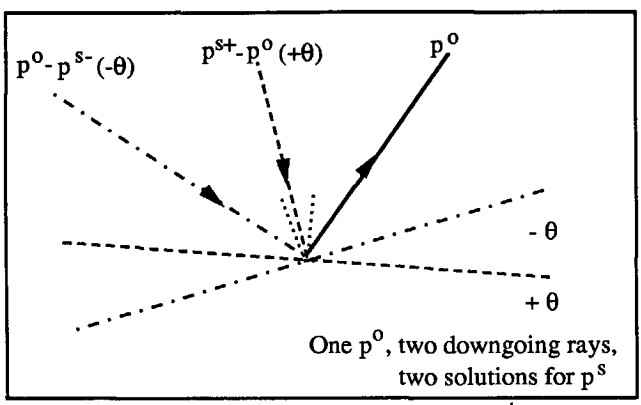

Fig.3.2.2: The reflected ray p^o originates either from $p^d = (p^{s+} - p^o)$ or $p^d = (p^o - p^{s-})$, depending on the dip of the interface

The selection of the particular p^o - p^s pairs is carried out by accepting both solutions for p^o for each $p^s \in \mathcal{D}(q_a)$. Then, the selected imaging surface contains the energy reflected from the interface above which the velocity of propagation is c_0. Since both solutions of p^o are accepted, the mean value of the selected data is obtained as

$$\tilde{\tilde{Q}}^{sct}(p^s, q_a, \omega) = \frac{1}{2}\tilde{\tilde{P}}^{sct}(p^{o+}, p^s, \omega) + \frac{1}{2}\tilde{\tilde{P}}^{sct}(p^{o-}, p^s, \omega) . \qquad (3.2.7)$$

Substitution of equation 3.2.1 into 3.2.7 results in

$$\widetilde{\widehat{Q}}^{sct}(p^s,q_a,\omega) = E'\widehat{W}(\omega)\int_{-\infty}^{\infty} F(x;p^s,q_a)exp\left\{i\omega\left[q_a z - p^s x\right]\right\}dx \quad , \tag{3.2.8}$$

where

$$F(x;p^s,q_a) = \frac{1}{2}E(x;p^{o+},p^s) + \frac{1}{2}E(x;p^{o-},p^s) \; . \tag{3.2.9}$$

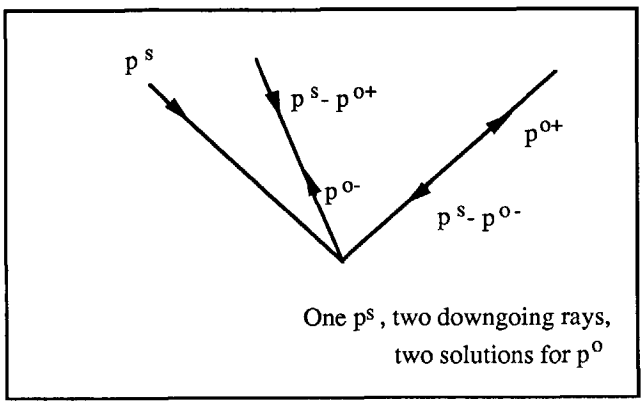

Fig.3.2.3: The same value of p^s is shared between two down-going rays; thus, two possible reflected rays p^o exist for this p^s.

It follows from equation 3.2.9 that, for a chosen q_a, the new amplitude F is a function of x and an algebraic function of p^s; it does not depend on p^o any more. Also, like the amplitude function E, it does not depend on ω. For the high frequency approximation, when $\omega \to \infty$, the main contribution to the integral on the right hand side of equation 3.2.8 comes from the stationary point. The value of p^s at the stationary point follows from the stationary phase condition, which states that the first derivative of the phase in equation 3.2.8 needs to be equal to zero

$$q_0\frac{\partial z}{\partial x} - p^s = 0 \; . \tag{3.2.10}$$

Using the value of p^s at the stationary point, a new function $\overline{F}$ is defined at the stationary point as

$$\overline{F}(x,q_a) = F\,|_{p^s = q_a\frac{\partial z}{\partial x}} \; . \tag{3.2.11}$$

This function, which does not depend explicitly on p^s, exists only if the value of p^s at the stationary point is contained in the domain $\mathcal{D}(q_a)$. With these changes, the scattered field given by equation 3.2.8, for the selected q_a, is replaced by

$$\tilde{\hat{Q}}^{sct}(p^s,q_a,\omega) = E^{'}\hat{W}(\omega)\int_{-\infty}^{\infty}\overline{F}(x;q_a)\exp\left(i\omega q_a z\right)\exp\left(-i\omega p^s x\right)dx \quad , \qquad (3.2.12)$$

for $\omega \to \infty$ and for $p^s \in \mathcal{D}(q_a)$. This integral vanishes for points p^s outside domain $\mathcal{D}(q_a)$, because of the assumption that the p^s is related to the stationary point. Since the function $\overline{F}$ does not depend on p^s any more, equation 3.2.12 is now recognized as a forward spatial Fourier transformation with respect to the coordinate x, with transform parameter $-\omega p^s$. To obtain the image of the interface, the inverse Fourier transform is therefore applied as

$$\hat{Q}^{sct}(x^s,q_a,\omega) = \frac{\omega}{2\pi}\int_{p^s \in \mathcal{D}(q_a)}\tilde{\hat{Q}}^{sct}(p^s,q_a,\omega)\exp\left(i\omega p^s x\right)dp^s \quad . \qquad (3.2.13)$$

Combining the equations 3.2.12 and 3.2.13, the application of the inverse Fourier transform leads to

$$\hat{Q}^{sct}(x^s,q_a,\omega) = E^{'}\hat{W}(\omega)\,\overline{F}(x;q_a)\exp\left(i\omega q_a z\right) \quad , \text{ for } \omega \to \infty \, . \qquad (3.2.14)$$

This expression, when inverse Fourier transformed to the time domain, gives the time image of the function z, which is the interface h as observed from the source level x_3^s. The time image of the interface follows from the phase shift in equation 3.2.14

$$T_a(x;q_a) = q_a\left(h(x) - x_3^s\right). \qquad (3.2.15)$$

The obtained time image is still dependent on the value q_a chosen for the vertical slowness function. The imaging procedure has been initiated by fixing q_0 at some constant value, where

$$q_0 = \frac{a}{c_0} = q_a. \qquad (3.2.16)$$

The maximum possible value of q_0 follows from equation 3.2.6, since only real solutions for p^s are acceptable, as

$$q_0 \leq \frac{2}{c_0} \,. \tag{3.2.17}$$

When the limiting value of q_0 is substituted into the travel time expression, equation 3.2.15, it gives the two-way travel time to the interface h. As shown in Figure 3.2.4, for the limiting case $a = 2$, the imaging line reduces to a point in the origin.

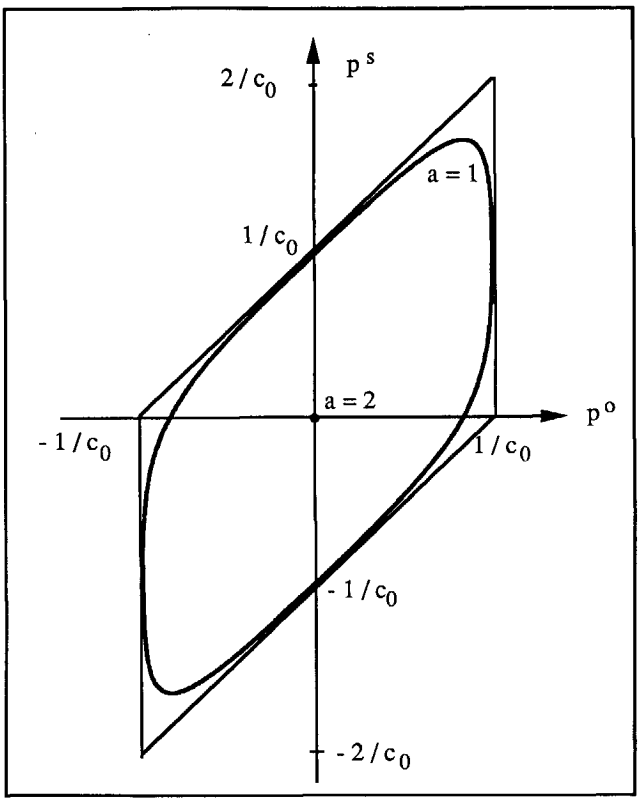

Fig.3.2.4: The limiting values for q_0 in the p^o-p^s plane: $q_a = 1/c_0$ and $q_a = 2/c_0$

The energy reflected from the interface h can only be imaged *after* it has been reflected, and the imaged time has to be not less than the one-way travel time. This implies that the lower limit of parameter a to be used in the imaging is $a = 1$, and the lower limit for q_0 then becomes

$$q_0 \geq \frac{1}{c_0} \,. \tag{3.2.18}$$

The lower limit of q_0 in equation 3.2.18, for $a = 1$, gives the one-way travel time to the interface when substituted in the travel time expression in equation 3.2.15. For $a = 1$, the imaging line approaches asymptotically the limits of the p^o and p^s range, as shown in Figure 3.2.4.

The true time image can now be obtained by resampling the data from the scaled time T_a (given by equation 3.2.15) to the true two-way travel time T

$$T(x) = \frac{2}{a} T_a(x; q_0) \quad , \tag{3.2.19}$$

giving the laterally changing two-way travel time to the interface h from the source level x_3^s.

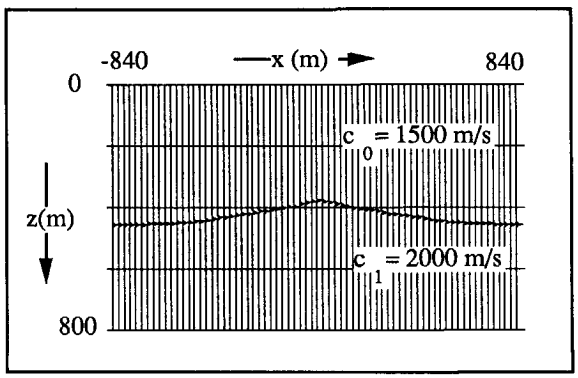

Fig.3.2.5: The depth-velocity model of the triangle-shaped interface, used to create the synthetic data set

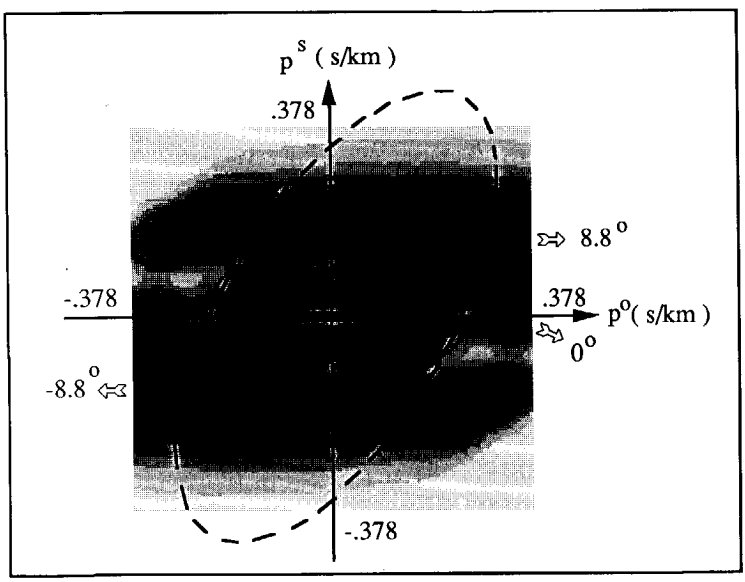

Fig.3.2.6: The energy density distribution in the p^o-p^s plane for the triangle-shaped interface of Figure 3.2.3, and the imaging line q_a for a=1.85 (dashed line)

The result of the imaging procedure is shown on a simple synthetic example. In Figure 3.2.5, the depth model used to create the synthetic data is shown. The triangle-shaped interface is 380 m deep at its shallow point, and 450 m at its flat parts, with the two flanks dipping at $\pm 8.8^0$. The velocity to the interface is 1500 m/sec. Using finite differences, a data set was created consisting of 128 shots and 128 receivers in a split-spread geometry, with $\Delta x^s = \Delta x^r =$ 12 m. This data set was subsequently double transformed to the Radon domain, with $\Delta p^o = \Delta p^s = 6 \cdot 10^{-6}$ sec/m, with 127 p^o-traces and 127 p^s-traces. To examine the data in the p^o - p^s domain, the energy density plot was generated by summing the squared amplitudes along the time axis, and is displayed in Figure 3.2.6. The data were selected along the imaging line using equation 3.2.7, for a particular value of q_0, where the chosen value was $a = 1.85$, and displayed in Figure 3.2.5. These data were then inverse Radon transformed, according to equation 3.2.13, transformed back to time, and scaled to two-way travel time, using equation 3.2.19. The resulting time image, displayed in Figure 3.2.8, closely resembles the input model.

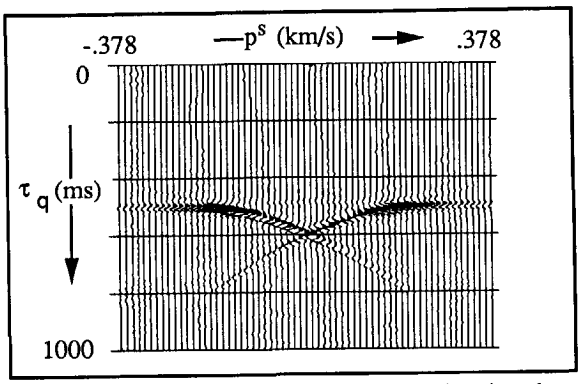

Fig.3.2.7: The reflected energy in the selected imaging plane (projected onto the $p^o = 0$ axis for plotting purpose). The horizontal axis is p^s, and the vertical axis is the vertical travel time t, scaled with the chosen q_a

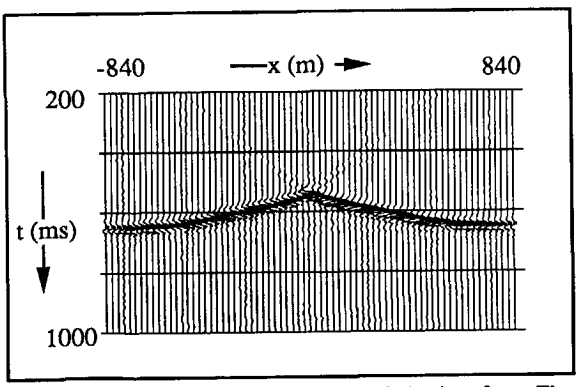

Fig.3.2.8: The resulting time image of the interface. The vertical axis is the two-way travel time.

3.3 MULTI-INTERFACE: RMS VELOCITY

Imaging described in the previous section is valid for the one-interface case. Also, the expressions for the scattered field derived in chapter 2 are valid for the field scattered from *one* interface, and the velocity c_0 used in the slowness function, equation 3.2.2, is the velocity of propagation in the medium above the interface. This theory can be extended to a multi-interface case, by assuming that the total scattered response is the superposition of M independent contributions as

$$p_{tot}^{sct}(x^r,x^s) = \sum_{m=1}^{M} p_m^{sct}(x^r,x^s) \quad , \tag{3.3.1}$$

where $p_m^{sct}(x^r,x^s) = p^{sct}(x^r,x^s)$. The assumption that the individual contributions are independent, that is, that there is no interaction between the individual fields, implies that multiple reflections and free surface effects are ignored, which is the common assumption in the theory of migration.

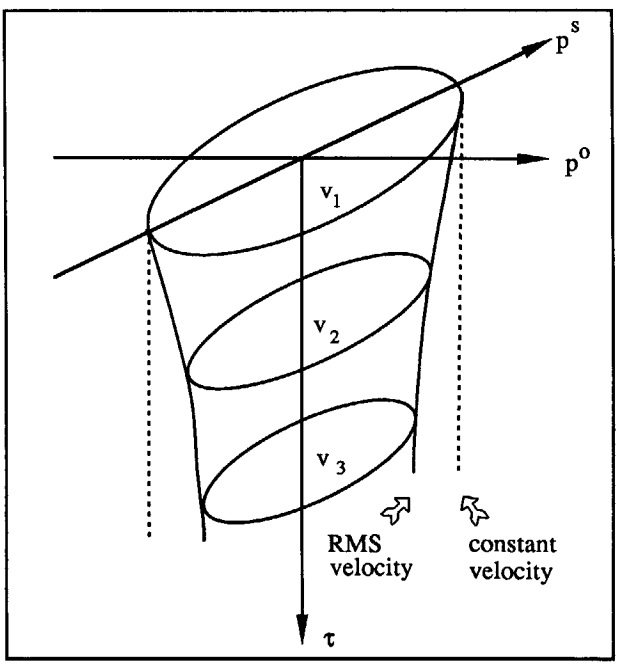

Fig.3.3.1: The imaging lines changing along the time axis, as a function of the *RMS* velocity distribution.

The superposition of the individual contributions is also valid in the double Radon domain, and the double Radon transformed total scattered field is written as

$$\tilde{\tilde{p}}^{sct}_{tot}(p^o,p^s) = \sum_{m=1}^{M} \tilde{\tilde{p}}^{sct}_{m}(p^o,p^s) \quad , \tag{3.3.2}$$

where $\tilde{\tilde{p}}^{sct}_{m}(p^o,p^s) = \tilde{\tilde{p}}^{sct}(p^o,p^s)$. With the assumption of linear superposition of individual fields, the interval velocities are replaced by the RMS velocities. In the equation 3.2.2, the interval velocity is substituted by the RMS velocity in the expression for the slowness function as

$$q_{RMS} = \sqrt{\frac{1}{c^2_{RMS}} - (p^o)^2} + \sqrt{\frac{1}{c^2_{RMS}} - (p^s - p^o)^2} \quad . \tag{3.3.3}$$

The introduction of the RMS velocity makes it possible to apply the imaging procedure to situations more realistic than the one interface case. The imaging lines change at every time sample, according to the RMS velocity function, as indicated in Figure 3.3.1: As the RMS velocities increase with time, the imaging lines become smaller. The data selection along the imaging lines is carried out in the time domain, and only the selected data are Fourier transformed to the frequency domain for the imaging. After this, the imaging procedure is the same as for the one interface case, as was outlined in the previous section.

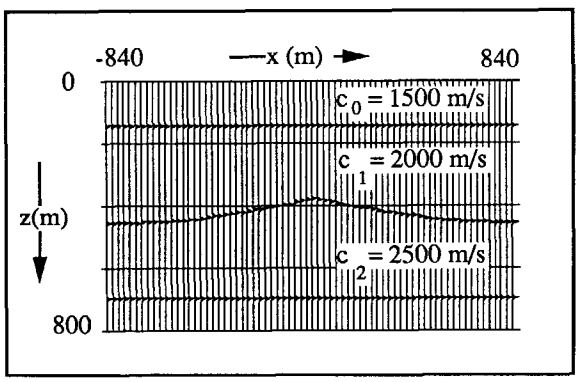

Fig.3.3.2: The depth-velocity multi-interface model

Imaging with the RMS velocities is illustrated with a simple synthetic example. Figure 3.3.2 shows the depth model, where the familiar triangle shaped interface is sandwiched between two flat interfaces. The same configuration for the synthetic data simulation by finite differences was used as for the one-interface example. The energy density plot shown in Figure 3.3.3 indicates that the energy reflected from horizontal interfaces dominates the data. Imaging with the known RMS velocity function produces the time image shown in Figure 3.3.4. Since this is a time migration, the propagation effects are not removed from the bottom interface, but it is positioned correctly. The free surface reflection is still present in the data at about 400 msec,

since nothing was done to remove it, and it is migrated as a primary reflection. This is a common problem with all migration algorithms, especially when they are applied prior to stack, which indicates that the free surface effects have to be removed first.

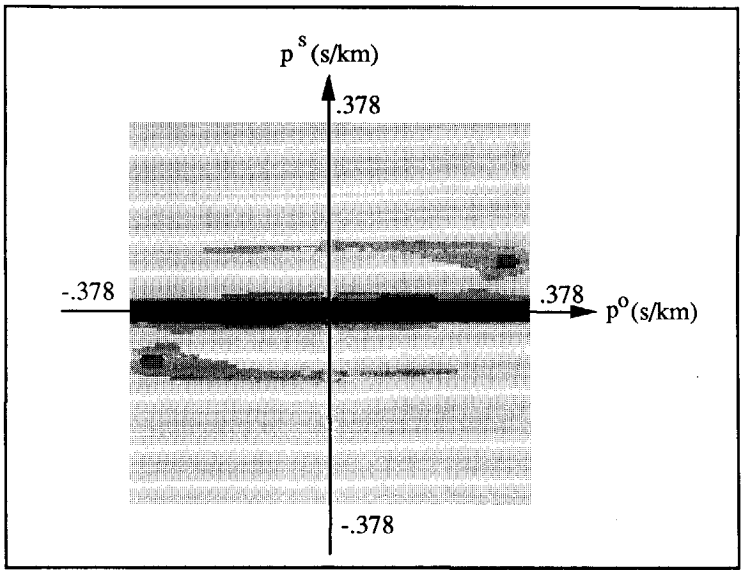

Fig.3.3.3: The energy density distribution in the p^o-p^s plane for the multi-interface model

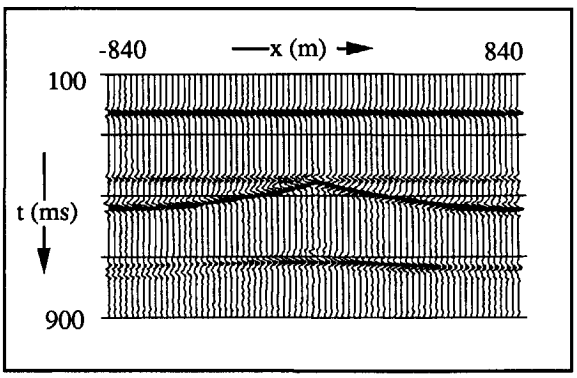

Fig.3.3.4: The resulting time image of the multi-interface model, with the multiple migrated as a primary

3.4 VELOCITY ANALYSIS IN THE $\tau - p$ DOMAIN

3.4.1 Data discretization

One of the consequences of transforming the data into the double Radon domain is the data discretization according to the local dip of the interface. This is shown by examining equation

3.2.10 and replacing the gradient of the interface by the tangent of the dip angle θ. Then, equation 3.2.10 can be rewritten to express lines of constant dip as

$$\tan\theta = \frac{p^s}{q}, \tag{3.4.1}$$

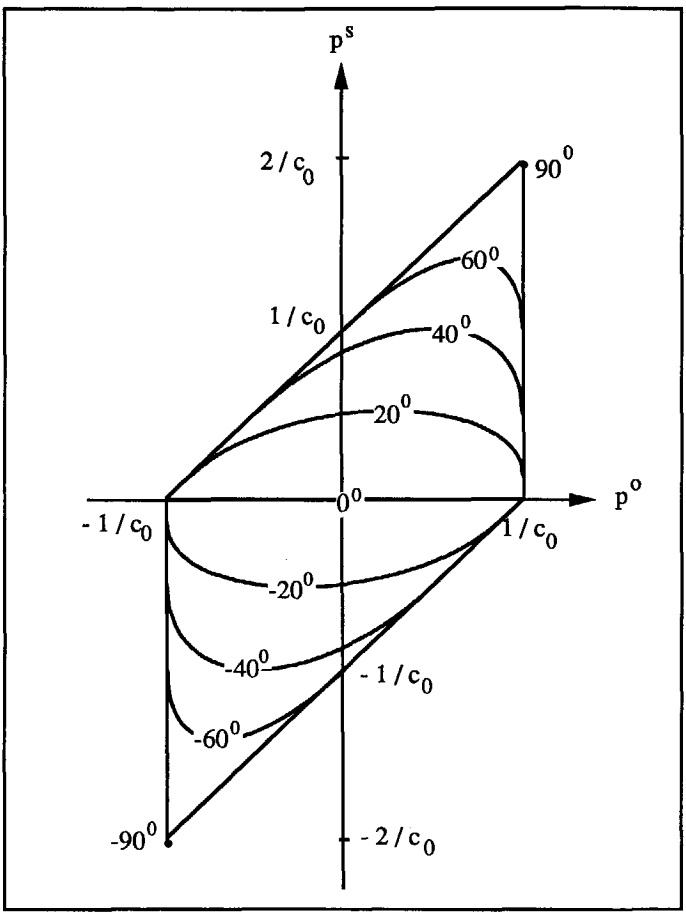

Fig.3.4.1: Lines of constant dip in the p^o-p^s plane

where q denotes either q_0 or q_{RMS}. The dip angle θ can be either the true dip of the interface, when q_0 is given by the interval velocity c_0, or the time dip when q_{RMS} is defined by the RMS velocity c_{RMS}. Equation 3.4.1 shows how the dip of the interface is related to the ray parameters in the p^o - p^s domain: the spatial complexity of the interfaces is manifested through the data distribution along the p^s-axis in the double Radon transformed domain. The expression for lines of constant dip (either true dip or time dip), when solved explicitly for p^s, is rewritten as

$$p^s = \frac{2p^o \tan^2\theta + 2\tan\theta\sqrt{\frac{1}{c_0^2} - (p^o)^2}}{1+\tan^2\theta}. \qquad (3.4.2)$$

These lines, for a particular value of velocity in the slowness function, are displayed in Figure 3.4.1. It follows from equations 3.4.1 and 3.4.2, and Figure 3.4.1, that in the $p^s = 0$ plane, only energy reflected from horizontal segments of the interfaces is present. This is an important conclusion, indicating the best approach for velocity analysis in the double Radon domain.

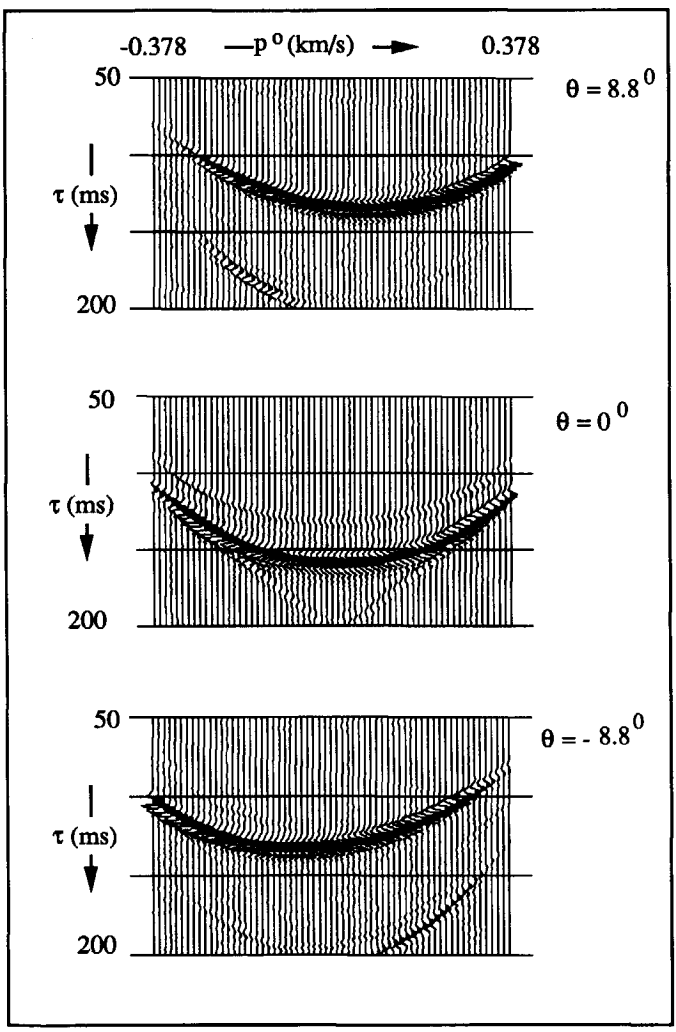

Fig.3.4.2: The data in the planes of constant dip for the triangle-shaped interface (projected onto the $p^s = 0$ axis)

The energy reflected from interfaces dipping at steeper dips maps at higher p^s values. In the limiting case of a vertical reflector, $\theta = 90^0$, all reflected energy maps into a line along the τ-axis at the point $p^s = 2/c_0$. Energy reflected from the interface dipping at positive dips maps along the positive p^s-axis, and energy reflected from interfaces dipping at negative dips maps along negative p^s-axis.

The dip-dependent data discretization in the p^o - p^s domain is also exhibited in Figure 3.2.6, which shows the energy density plot for the triangle-shaped interface. The high energy density concentration along three principal lines indicates the presence of the three interface segments, two dipping at 8.8^0 and -8.8^0, and the flat parts at $p^s = 0$. The energy along these three principal lines in Figure 3.2.6 is interconnected by the energy scattered from the point diffractors at the edge of the triangle. To show the shape of the τ-p curves resulting from the three interface segments, the data are intersected along the three principal lines and displayed in Figure 3.4.2. As expected, the intersection at $p^s = 0$, for the horizontal segment, shows an exactly elliptical τ-p response. Intersection for the interface dipping at 8.8^0, along the line $p^s = 0.15q$, shows the quasi-elliptical shape of the τ-p curve, with its apex shifted to the positive p^o values, while the intersection for -8.8^0, that is along $p^s = -0.15q$, shows the τ-p response anti-symmetrical to the previous one, with its apex shifted to the negative p^o values. It will be shown in chapter 4 that the apex p^o values correspond to the rays normal to a single interface, which in this case are $p^o = \pm 0.1$ sec/km.

3.4.2 Curve fitting

In the $p^s = 0$ plane, due to the data discretization, all τ-p curves are elliptical, since only the energy reflected from horizontal components of the subsurface is present. This means that velocity analysis by curve fitting is best achieved in this plane, because the theoretical elliptical travel time curves fit the data much better than they do in conventional CMP gathers using the hyperbolic assumption. Also, the output of such a velocity analysis is the RMS velocity function, rather than the stacking velocity.

The method used for the velocity analysis in the $p^s = 0$ plane is based on measuring the coherency of the best elliptical fit (Vincentie, 1989), analogous to velocity analysis in the t-x domain, where the coherencies are measured for the best hyperbolic fit (Yilmaz, 1987). The coherencies are calculated along elliptical curves in the τ-p domain

$$\tau^2(p^o) = \tau_0^2\left[1 - (p^o)^2 v_{RMS}^2\right] , \qquad (3.4.3)$$

where $\tau(p^o)$ is the two-way vertical travel time in the $p^s = 0$ plane as a function of the ray parameter p^o, and τ_0 is the normal two-way vertical travel time at $p^o = 0$.

For a number of trial (τ_0,v_{RMS}) pairs, the coherency is measured along the corresponding ellipse, as shown in Figure 3.4.3. The most often used measure for coherency is the semblance S, defined as the normalized ratio of coherent energy to the total energy (Neidell and Taner, 1971; Yilmaz, 1987)

$$S = \frac{1}{N} \frac{\sum_{\tau=1}^{w} \left(\sum_{i=1}^{N} A_{i,\,\tau(i)} \right)^2}{\sum_{\tau=1}^{w} \sum_{i=1}^{N} A_{i,\,\tau(i)}^2}, \tag{3.4.4}$$

where N is the number of the p^o - traces, $A_{i,\tau(i)}$ is the amplitude on the i-th p^o -trace at the time $\tau(i)$, and w is the length of the time window in which the amplitudes are summed for each trial (τ_0, v_{RMS}) pair.

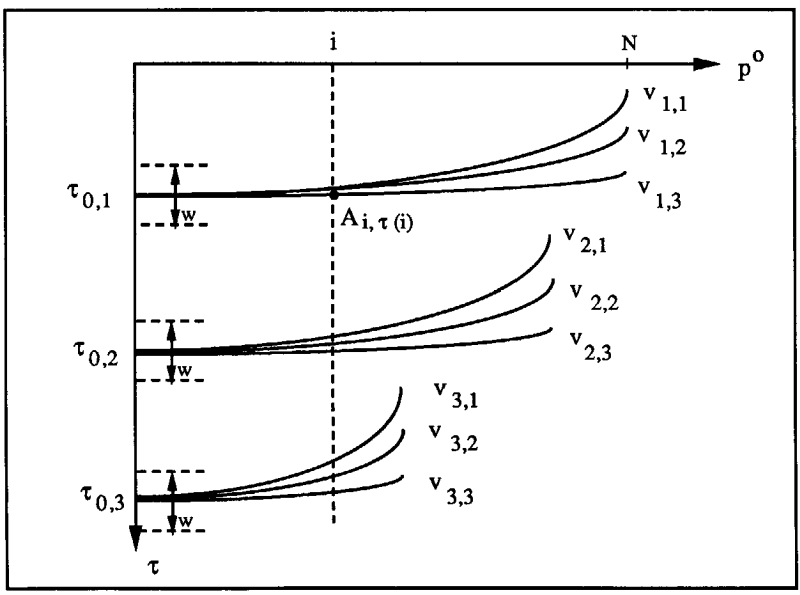

Fig.3.4.3: The principle for velocity analysis in the $p^s = 0$ plane

The output of such a velocity analysis procedure is a contour plot of coherencies in the time-velocity coordinate system, which then requires velocity picking, that is, choosing the velocities which produce the highest coherencies along the time axis. The procedure is illustrated in Figure 3.4.4. The velocity producing the highest coherency is accepted as the RMS velocity at the particular time τ_0, and the final v_{RMS} function is obtained by linear interpolation between the picked values.

3.5 FREQUENCY SCALING METHOD

Another approach to migration applied in the p^o- p^s domain, as described by Vissinga (1992), is to perform frequency scaling of the data discretized in planes of constant dip. For that purpose, equation 3.2.1 is rewritten as

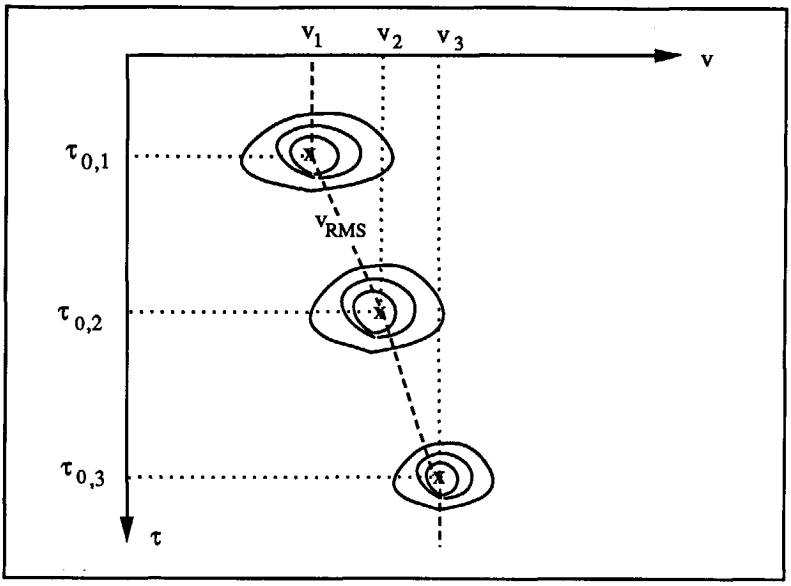

Fig.3.4.4: A contour plot of the calculated coherencies and the corresponding velocity picking

$$\tilde{\tilde{p}}^{sct}(p^o,p^s,\omega) = E'\,\widehat{W}(\omega)\int_{-\infty}^{\infty} E\,exp\left\{i\omega\left[\psi_0 T_0 - p^s x\right]\right\} dx \quad , \tag{3.5.1}$$

where the normalized vertical slowness $\psi_0 = \psi_0(p^o,p^s)$ is given as

$$\psi_0(p^o,p^s) = \frac{c_0}{2}\left[\sqrt{\frac{1}{c_0^2}-\left(p^o\right)^2} + \sqrt{\frac{1}{c_0^2}-\left(p^s-p^o\right)^2}\right], \tag{3.5.2}$$

and T_0 is defined as the two-way travel time from the source level to the interface

$$T_0(x) = \frac{2}{c_0}\left(h(x) - x_3^s\right). \tag{3.5.3}$$

The data discretization in the p^o- p^s domain is exploited by selecting the (p^o, p^s) pairs which belong to the domain $\mathcal{D}(p^d)$, defined as

$$\mathcal{D}(p^d) \;:\; p^s = p^d \psi_0 \,. \tag{3.5.4}$$

From equation 3.5.4, it follows that the parameter p^d is equivalent to the ray parameter p^s, scaled by the normalized slowness function ψ_0, and, as such, it is called the dip slowness. The relation of the dip slowness to the dip of the interface will be shown after the stationary phase condition has been applied. For now, it suffices to say that the domain $\mathcal{D}(p^d)$ is the domain of a constant dip. The scattered field, restricted to the $\mathcal{D}(p^d)$ domain is written as

$$\tilde{\tilde{\tilde{Q}}}^{sct}(p^o,p^s,\omega) = E^{'}\widehat{W}(\omega)\int_{-\infty}^{\infty} E\, exp\left\{i\omega\,\psi_0\left[T_0 - p^d x\right]\right\} dx \quad , \tag{3.5.5}$$

for $(p^o\text{-}p^s) \in \mathcal{D}(p^d)$. For a fixed value of p^d, the term in the brackets $[T_0 - p^d x]$ is completely determined by the properties of the interface, and does not depend on the $p^o\text{-}p^s$ values, while the function ψ_0 depends entirely on the ray parameters p^o and p^s, for the given interface. For energy reflected from a horizontal interface, which is mapped into the $p^d = p^s = 0$ plane, it follows from equation 3.5.2 that the function ψ_0 represents elliptical move-out, and when combined with the function T_0 in the expression for phase (equation 3.5.1) gives the elliptical τ-p response from horizontal layers. The shape of the τ-p curve is determined by the p^d (or p^s) value, and becomes quasi-elliptical in all planes where $p^s \neq 0$.

If the correction for the quasi-elliptical shape is applied to the data discretized into constant p^d planes to produce the elliptical response, the result is equivalent to dip moveout (DMO). By carrying the correction procedure one step further and applying the complete move-out correction to flatten the τ-p curve for the phase differences, the actual migration is achieved.

In each $\mathcal{D}(p^d)$, the move-out correction is performed by scaling each frequency component by the corresponding function ψ_0. The procedure is repeated in each $\mathcal{D}(p^d)$, and the mean value of all move-out corrected data leads to

$$\tilde{\tilde{\tilde{Q}}}^{sct}(p^d,\omega) = \int_{-\infty}^{\infty} \widehat{F}_0(x,p^d,\omega)\; exp\left\{i\omega\left[T_0 - p^d x\right]\right\} dx \quad , \tag{3.5.6}$$

where

$$\widehat{F}_0(x,p^d,\omega) = \frac{\displaystyle\iint_{(p^o,p^s)\,\in\,\mathcal{D}(p^d)} E^{'}\widehat{W}\left(\frac{\omega}{\psi_0}\right) E\, dp^o\, dp^s}{\displaystyle\iint_{(p^o,p^s)\,\in\,\mathcal{D}(p^d)} dp^o\, dp^s} \quad . \tag{3.5.7}$$

From here on, the procedure is identical with the imaging procedure described in section 3.2. The main contribution to the integral in equation 3.5.7, for $\omega \rightarrow \infty$, comes from the

stationary points. The value of p^d follows from the stationary phase condition at the stationary point

$$p^d = \frac{2}{c_0} \tan\theta. \tag{3.5.8}$$

When the explicit value of p^d is substituted in equation 3.5.6, the amplitude becomes a function of (x,ω) only, rather than being a function of (x, p^d,ω). This leads to the recognition of the forward Radon transform, and the application of the inverse Radon transform leads to

$$\hat{P}^{sct}(x,\omega) = \hat{\hat{F}}_0(x,\omega)\ exp\left(i\omega T_0\right), \text{ for } \omega \to \infty. \tag{3.5.9}$$

Again, an inverse Fourier transform with respect to time leads to the time image T_0 of the interface h_0.

The data set created for the triangle-shaped interface was migrated using the frequency scaling method. The resulting time image of the reflector is shown in Figure 3.5.1, as a function of two-way travel time. For this simple model, the result does not differ from the image obtained by the imaging method, shown in Figure 3.2.8.

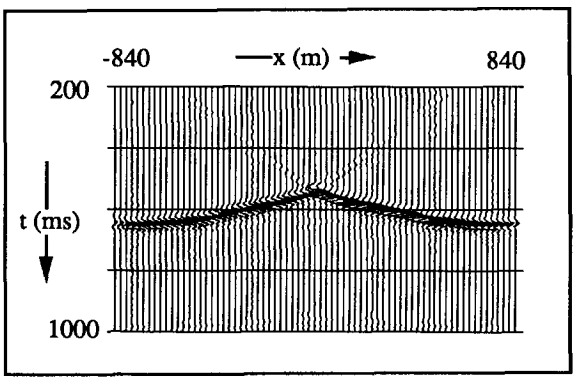

Fig.3.5.1: The time image of the triangle shaped interface model of Figure 3.2.5, obtained by the frequency scaling method.

This method is extended to the multi-interface case by repeating the complete frequency scaling procedure with a number of constant velocities, and allowing the selected dip lines to change with each selected velocity. The final image is created by selecting the corresponding window for each interface, according to the velocity distribution. However, it would not be practical for a rapidly changing velocity medium, where a large number of scaling procedures would have to be repeated in small windows, each of constant velocity.

4

PRACTICAL CONSIDERATIONS

4.1 INTRODUCTION

The p^o - p^s domain is unfamiliar to most geophysicists, and migration in the p^o - p^s domain is even more unfamiliar. It is certainly an unconventional way to handle seismic data. The unknown aspects of the p^o - p^s domain are described in this chapter. First, its connection with the more familiar, conventional τ-p transform is established. For that purpose, the geometrical aspects of the travel time response in the t-x domain and the τ-p domain are described, for both the CMP geometry and the common shot geometry. It is shown that the dip information becomes hidden in the CMP geometry in both the t-x and τ-p domains, while the shot geometry preserves the dip information in both domains. This conclusion is extended to the double Radon transformed domain by showing the connection between the τ-p response over plane dipping layers in the conventional Radon transformed domain and τ-p response in the planes of constant dip in the p^o - p^s domain.

The quality of the Radon transform is higher when applied to data with split-spread geometry, since negative offsets also carry valuable information. It is shown how the reciprocity principle can be applied to t-x data to improve the result of the double Radon transformation.

Even though the theoretical limits for the ray parameters p^o and p^s are established as $1/c_0$ and $2/c_0$ respectively, they cannot be achieved in the double Radon transformed data due to the limitations of the recorded offsets. Apart from this limitation, which is imposed by the data acquisition parameters, there is also a limit to the highest dip to be migrated, imposed by the migration algorithm itself. However, it is shown that dips higher than 60^o, which is the theoretical limit, can be recovered from the diffraction energy.

The migration in the double transformed Radon domain causes distortions of the seismic wavelet. These changes are caused by interpolation, integration, and selective filtering, which are all inherent to the Radon transformation. These changes, except for the interpolation effects,

can be corrected for, and the original waveform can be recovered to a certain extent. However, regardless of the changes to the wavelet, the interfaces are properly positioned after migration.

Finally, it is shown how the data collected over long lines can be segmented into smaller subsets which can be migrated individually. The final output is composed of individual segments, producing the result which is consistent with one-pass migration.

4.2 GEOMETRICAL ASPECTS

The data discretization according to the local dip of the interface in the p^o - p^s domain was described in section 3.4.1 of this thesis. The time response in planes of constant dip can be compared with the τ-p response over plane horizontal and dipping interfaces. For that purpose, the geometrical aspects in both the t-x domain and in the τ-p domain are investigated, for both CMP and shot geometry.

4.2.1 The t-x response

CMP gathers

The CMP geometry, for one source and one receiver position, over an interface dipping at an angle θ, is shown in Figure 4.2.1. The distance between the source and the receiver is $x^o = x$, and the thickness of the layer at the midpoint location is z, while the velocity of propagation through the layer above the dipping interface is c. The travel time response t for a complete CMP gather, as derived by Levin (1971), is given by

$$t^2 = t_0^2 + \frac{x^2}{c^2} cos^2\theta \,, \tag{4.2.1}$$

where t_0, the normal incidence travel time appearing at the zero offset trace, is given by

$$t_0 = \frac{2z\,cos\theta}{c} \,. \tag{4.2.2}$$

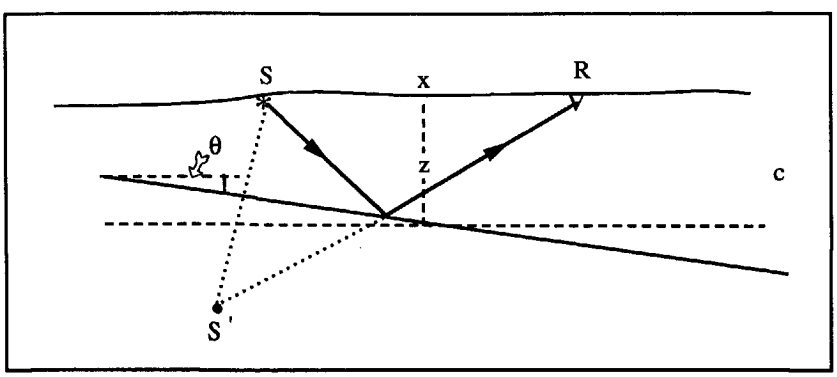

Fig.4.2.1: The common mid-point (CMP) geometry over a dipping layer

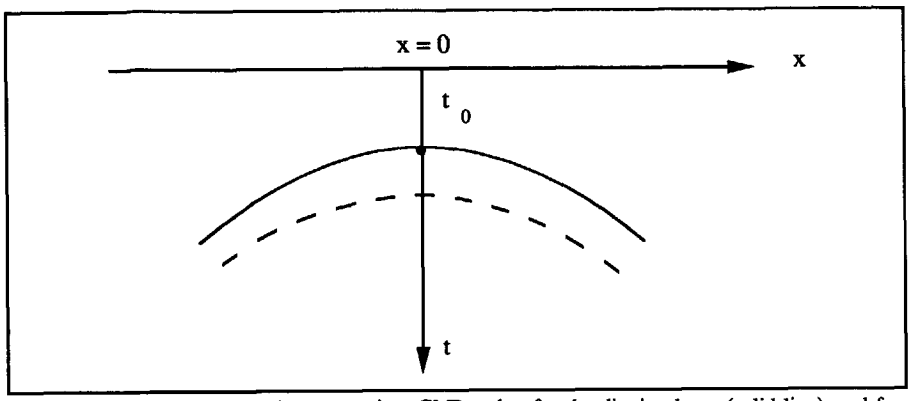

Fig.4.2.2: The time-space (t-x) response in a CMP gather for the dipping layer (solid line), and for the horizontal layer (dashed line)

The travel time hyperbola, given by equation 4.2.1 and shown in Figure 4.2.2 (solid line), is symmetrical with respect to $x = 0$, and has its apex at the same point. For a horizontal interface, that is $\theta = 0$ in equation 4.2.1, the travel time response is also a symmetrical hyperbola. The τ-p response for a dipping interface shown in Figure 4.2.2 with the solid line is equivalent to the travel time response over a horizontal interface at depth $z \cdot cos\ \theta$, and velocity of propagation of $c/cos\ \theta$. The dashed line in Figure 4.2.2 corresponds to the travel time over the horizontal interface at depth z and velocity of propagation c, which is shown in Figure 4.2.1 by the horizontal dashed line. Whether the interface is horizontal or dipping, the t-x response is a symmetric hyperbola in CMP gathers.

Shot gathers

A shot gather over the same layer as in the previous experiment, with split-spread shooting geometry, is shown in Figure 4.2.3. The thickness of the layer z is measured at the shot position. The corresponding travel time curve for a complete shot gather (Slotnick, 1959; Tatalovic, 1988) is given by

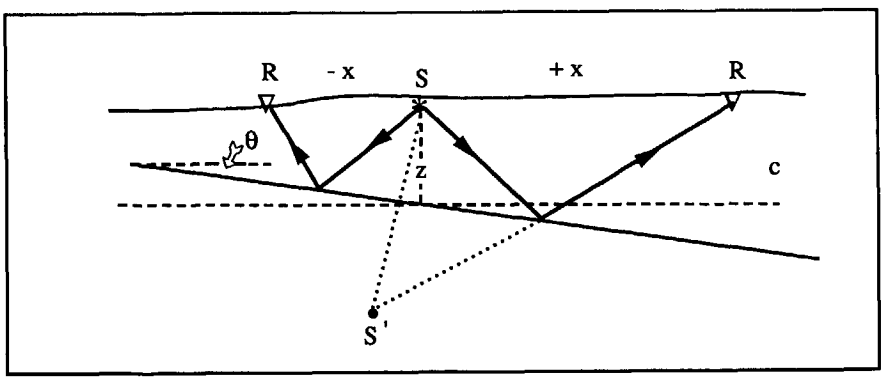

Fig.4.2.3: The split-spread shot geometry over a dipping layer

$$t^2 = t_0^2 \cos^2\theta + \frac{\left(x + 2z \cos\theta \sin\theta\right)^2}{c^2} . \qquad (4.2.3)$$

This is again an equation of an hyperbola in t-x space, as shown in Figure 4.2.4 by the solid line. The apex of this hyperbola is shifted up-dip, towards negative x-values for the positive dip. The minimum travel time t_a at the apex of the hyperbola is recorded at offset x_a, and is given by

$$\begin{aligned} t_a &= \frac{2z \cos\theta}{c} \cos\theta \\ x_a &= -2z \cos\theta \sin\theta . \end{aligned} \qquad (4.2.4)$$

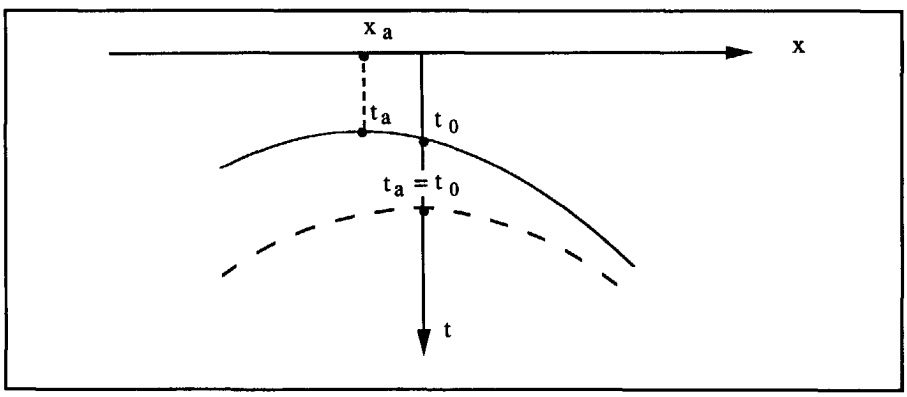

Fig.4.2.4: The t-x response in a shot gather for the dipping layer (solid line), and for the horizontal layer (dashed line)

The equivalent horizontal interface (for $\theta = 0$) is shown by the dashed line in Figure 4.2.3. The travel time response from a horizontal interface, a symmetric hyperbola with apex at $x_a = 0$, is shown in Figure 4.2.4 by the dashed line. The travel time at the apex is the same as the travel time at the zero-offset trace.

In shot gathers, the travel time response over a dipping interface is a hyperbola shifted along the x-axis, up-dip from the shot position, whereas the travel time response from either horizontal interfaces or dipping interfaces is a symmetrical hyperbola in the CMP oriented data. The symmetrical shape of the travel time curves in the CMP oriented data has been used to justify the assumption of a horizontally layered earth, commonly exploited in conventional data processing. The asymmetry of the travel time curves in shot gathers made the shot-oriented data processing unattractive; however, when the data are treated correctly, some valuable information can be recovered with shot-oriented processing.

4.2.2 The τ-p response

CMP gathers

The derivation of the τ-p response from a dipping interface starts from the basic equation for the vertical travel time for a single layer (Diebold and Stoffa, 1981)

$$\tau = z\left(q^d + q^u\right), \tag{4.2.5}$$

where the vertical slowness of the downgoing rays q^d is identical with the vertical slowness at source q^s, and the vertical slowness of the upgoing rays q^u is identical with the vertical slowness at receiver q^o, that is

$$\begin{aligned} q^d &= q^s = \sqrt{\frac{1}{c^2} - \left(p^s - p^o\right)^2} \\ q^u &= q^o = \sqrt{\frac{1}{c^2} - \left(p^o\right)^2} \end{aligned} \tag{4.2.6}$$

The downgoing and upgoing rays are characterized by the ray parameters p^d and p^u, which are related to the source and receiver ray parameters p^s and p^o as

$$\begin{aligned} p^d &= p^s - p^o \\ p^u &= p^o \end{aligned} \tag{4.2.7}$$

In terms of the incidence angle i^d and emergence angle i^u which are formed relative to the vertical by the downgoing and upgoing rays, as shown in Figure 4.2.5, the vertical slownesses are defined as

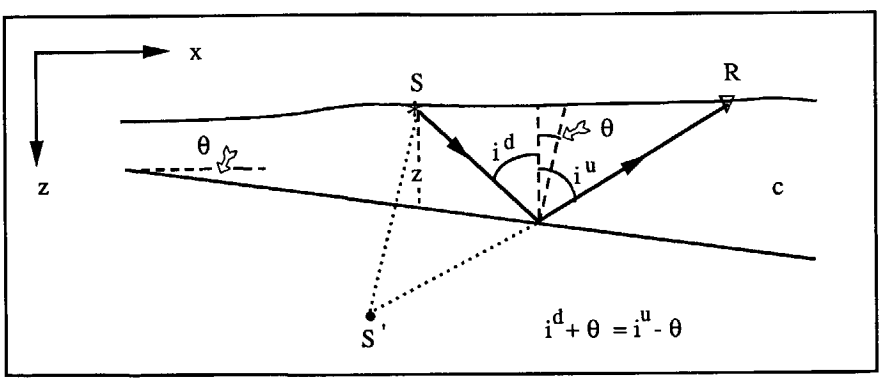

Fig.4.2.5: The geometrical relations formed by downgoing and upgoing rays

$$q^d = \frac{\cos i^d}{c}$$
$$q^u = \frac{\cos i^u}{c} . \tag{4.2.8}$$

Substitution of equations 4.2.8 into the travel time equation 4.2.5, and algebraic manipulation of the geometrical relations of the angles i^d, i^u, and θ, leads to the following expressions for the vertical travel time

$$\left(\tau^d\right)^2 = \tau_a^2 - \tau_a^2 \sin^2\left(i^d + \theta\right)$$
$$\left(\tau^u\right)^2 = \tau_a^2 - \tau_a^2 \sin^2\left(i^u - \theta\right) . \tag{4.2.9}$$

In these equations, τ^d is the vertical travel time in terms of downgoing rays, as observed in a common receiver gather, and τ^u is the vertical travel time in terms of upgoing rays, as observed in a common shot gather. The vertical travel time τ_a in equation 4.2.9 is equal to the travel time t_0 for the zero offset trace in the t-x domain

$$\tau_a = \frac{2z \cos\theta}{c} . \tag{4.2.10}$$

As explained by Diebold and Stoffa (1981), the ray parameters for the downgoing and upgoing rays are averaged in the CMP geometry, as

$$p = \frac{p^d + p^u}{2} = \frac{\sin i^d + \sin i^u}{2c} . \tag{4.2.11}$$

Again, using the geometrical relations of the angles i^d, i^u, and θ, equation 4.2.11 can be rewritten as

$$p = \frac{\cos\theta}{c} \cdot \sin\left(i^d + \theta\right) = \frac{\cos\theta}{c} \cdot \sin\left(i^u - \theta\right) . \tag{4.2.12}$$

Substitution of equations 4.2.12 into either of equations 4.2.9 leads to the τ-p response over a dipping interface in a CMP gather as

$$\tau^2 = \tau_a^2 \left(1 - p^2 \frac{c^2}{\cos^2\theta}\right) . \tag{4.2.13}$$

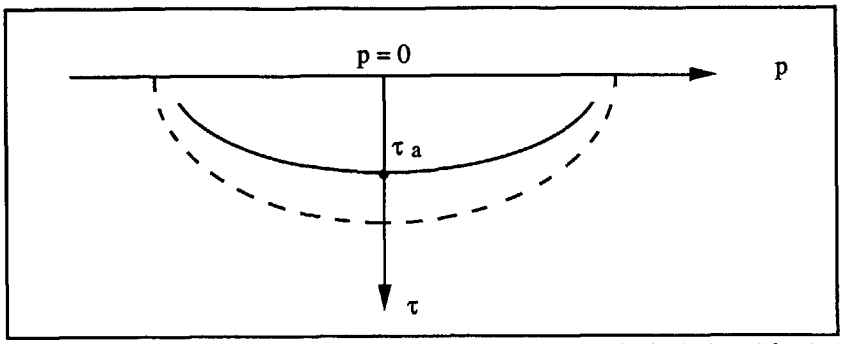

Fig.4.2.6: The τ-p response in a CMP gather for the dipping layer (solid line), and for the horizontal layer (dashed line)

The elliptical τ-p response for a CMP gather over a dipping interface is shown in Figure 4.2.6 as a solid line. For a horizontal interface, that is for $\theta = 0$, equation 4.2.13 becomes identical with equation 3.4.3 for elliptical τ-p curves in the $p^s = 0$ plane, since for horizontal layers $p = p^d = p^u$. The dashed line in Figure 4.2.6 shows the elliptical τ-p response over the horizontal interface shown in Figure 4.2.1. The τ-p response in CMP gathers is elliptical, whether the interface is horizontal or dipping.

Shot gathers

Starting with equation 4.2.9 for vertical travel times in shot gathers, and using trigonometric relations for angles i^d, i^u, and θ, the travel time curve in terms of ray parameters for the upgoing rays becomes

$$\left(\tau^u\right)^2 = \tau_0^2 \left[1 - c^2\left(p^u\right)^2\left(1 - tan^2\theta\right) + 2\,p^u q^u tan\,\theta\right], \tag{4.2.14}$$

where the vertical travel time

$$\tau_0 = \frac{2z\,cos\,\theta}{c}\,cos\,\theta \tag{4.2.15}$$

equals the travel time at the apex t_a in the t-x domain; it is observed at the ray emerging at the vertical to the receiver, that is at $p^u = 0$.

The curve described by equation 4.2.14 is no longer elliptical. It is the last term in equation 4.2.14, containing the vertical slowness, which deforms the ellipse into a quasi-ellipse. The τ-p curve in a shot gather over a dipping interface is shown in Figure 4.2.7 by the solid line. The apex of the quasi-elliptical curve is shifted downdip, to the trace with ray parameter value

$$p_a^u = \frac{\sin\theta}{c} \quad . \tag{4.2.16}$$

For a horizontal layer, that is for $\theta = 0$, the quasi-elliptical response in equation 4.2.14 reduces to the elliptical response as was given in equation 3.4.3: the terms containing $tan\theta$ become equal to zero, and $\tau_a = \tau_0$ for horizontal layers. The τ-p response of the horizontal layer of Figure 4.2.3 is shown as a dashed line in Figure 4.2.7.

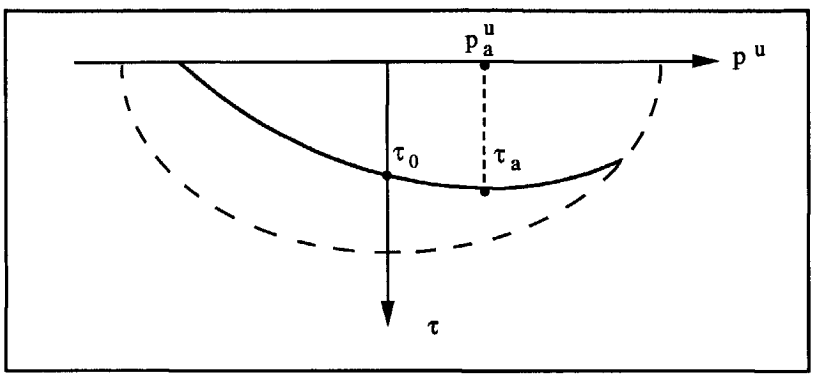

Fig.4.2.7: The τ-p response in a shot gather for the dipping layer (solid line), and for the horizontal layer (dashed line)

Equation 4.2.14 is derived for plane dipping layers. Since the application of the double Radon transform causes the discretization of the data into planes of constant dip, it follows that the vertical travel time in planes of constant dip in the p^o - p^s - τ domain can also be expressed in terms of ray parameters, the dip of the interface and the velocity through the layer. Since $p^o = p^u$ (equation 4.2.7), and $q^o = q^u$ (equation 4.2.6), equation 4.2.14 for vertical travel time from plane dipping layers is also valid as expression for vertical travel time in planes of constant dip in the p^o - p^s - τ domain. The phase factor in the expression for the double Radon transformed data, equation 3.2.1, also gives the vertical travel time in the p^o - p^s domain. The main difference between the travel time described by the phase function in equation 3.2.1 and the vertical travel time in equation 4.2.14 is that equation 4.2.14 holds in the planes of constant dip only, while equation 3.2.1 gives the travel time at any point in p^o - p^s space, from any arbitrarily shaped interface. As such, it also contains the coordinates of the interface.

Comparison of the theoretical τ-p response shown in Figure 4.2.7 with the data sections along the lines of constant dip in Figure 3.4.2 confirms these conclusions.

The apex of the quasi-elliptical curves in planes of constant dip is given by equation 4.2.16 for the p^o coordinate. To determine at which p^s value the apex occurs, equation 4.2.16 is substituted into the expression for the constant dip lines, equation 3.4.1. This leads to

$$p_a^s = \frac{2 \sin \theta}{c} . \qquad (4.2.17)$$

It follows from equations 4.2.16 and 4.2.17 that the apexes of the quasi-elliptical travel time curves, when projected on to the p^o - p^s plane, are distributed along the line

$$p^s = 2p^o . \qquad (4.2.18)$$

The same line connects the apexes of the constant dip lines, given by equation 3.4.2. This can be shown by finding the value p^o at which the first derivative of the function given by equation 3.4.2 equals zero, that is $\partial p^s/\partial p^o = 0$. This leads to

$$p^o = \frac{\sin \theta}{c} , \qquad (4.2.19)$$

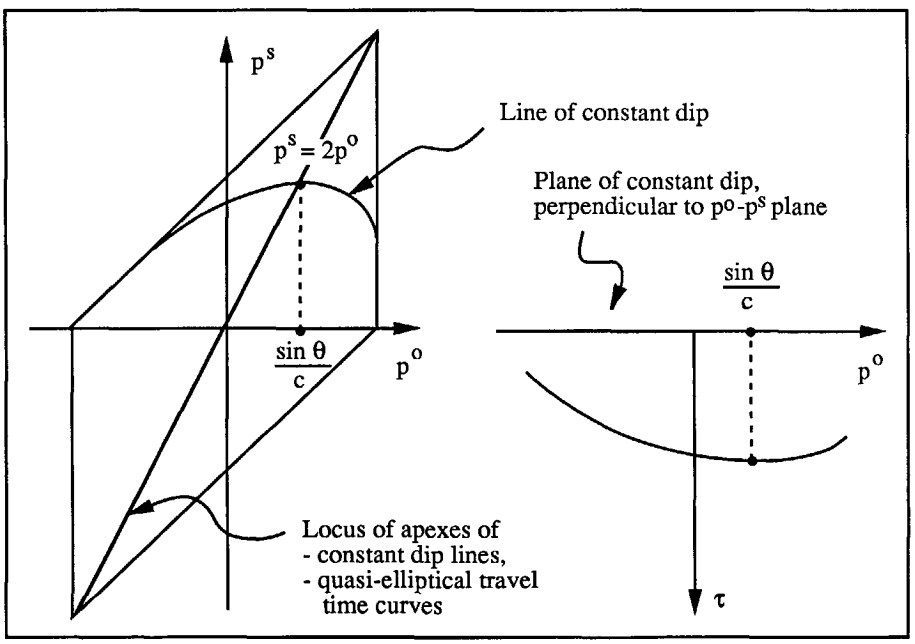

Fig.4.2.8: The constant dip line has its apex on the $p^s = 2p^o$ line (left). The τ-p response in the constant dip plane (right) has its apex at the same p^o value, and at the same p^s value when projected onto p^o-p^s plane.

which is the same value p^o at which the quasi-elliptical τ-p response curves have their apexes. Thus, the projection of the line which connects the apexes of the quasi-elliptical curves onto the p^o - p^s plane, given by equation 4.2.18, also connects the maxima of the lines of constant dip in

the p^o - p^s plane. This is shown in Figure 4.2.8, for a constant dip line in the p^o - p^s coordinates, and the corresponding constant dip plane in the τ-p coordinates.

By repeating the same procedure to find the apexes of the imaging lines, given by equation 3.2.2, it is found that the imaging lines have their apexes along the same line given by equation 4.2.18.

4.3 RECIPROCITY AND THE EFFECT OF MISSING OFFSETS

The reciprocity principle states that, if the source and the receiver were interchanged, the same trace would be recorded. In terms of ray parameters, this implies the following substitutions, as shown in Figure 4.3.1

$$\begin{aligned} p^o &\rightarrow p^s - p^o \\ p^s - p^o &\rightarrow p^o \ . \end{aligned} \tag{4.3.1}$$

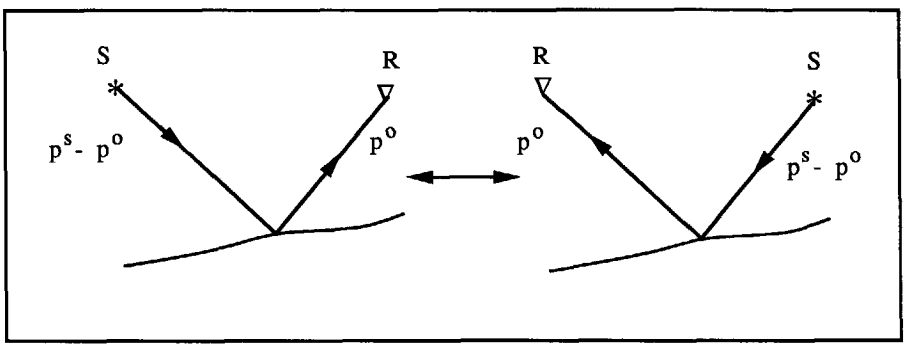

Fig.4.3.1: The upgoing and downgoing rays can be interchanged according to the reciprocity principle.

By equating p^o to $(p^s - p^o)$ in equation 4.3.1, it is recognized that the obtained line of symmetry, $p^s = 2p^o$, is the same as the line in equation 4.2.18, which connect the apexes of the important curves in the p^o - p^s domain. Figure 4.3.2 illustrates the symmetry of the p^o - p^s domain with respect to line $p^s = 2p^o$, and lists all the features of the p^o - p^s domain connected to this line. Thus, the reciprocity principle can be applied to the double Radon transformed data. For a particular value of p^s, the vertical slowness function q (equation 3.2.2) does not change when p^o is substituted by $(p^s - p^o)$. Similarly, the double Radon transformed data, equation 3.2.1, do not change when, for a fixed value of p^s, p^o is substituted by $(p^s - p^o)$. It can now be recognized that accepting both solutions for p^o in the imaging equation 3.2.5, is actually obeying the reciprocity principle and allowing sources and receivers to be exchanged.

The reciprocity principle is exploited in the t-x domain rather than in the p^o - p^s - τ domain, because the use of reciprocity can help obtain a higher quality of transformation. This is achieved by recovering, to a certain extent, missing offsets. As shown in section 4.2.1, traces at

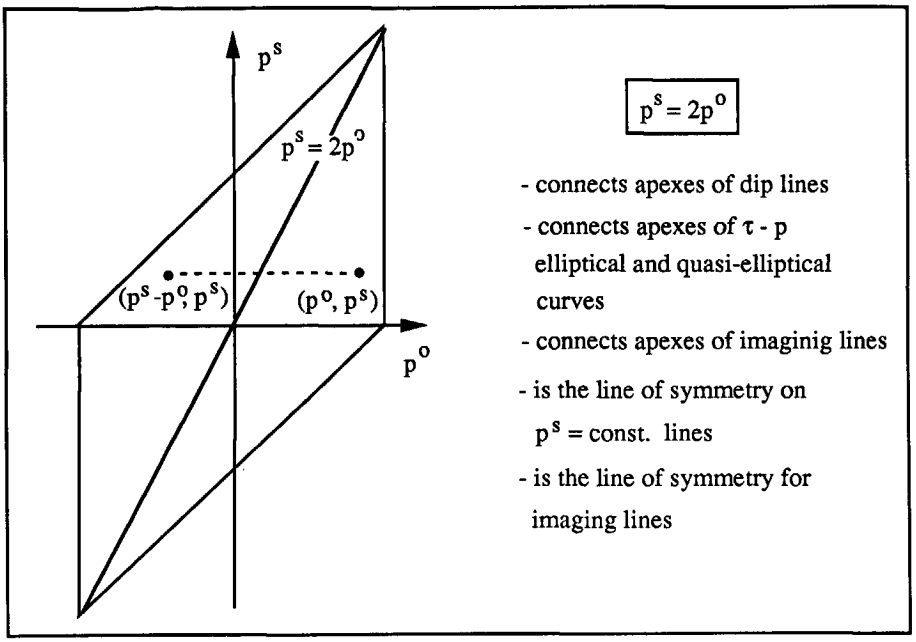

Fig.4.3.2: The symmetry of the p^o-p^s space with respect to the $p^s = 2p^o$ line

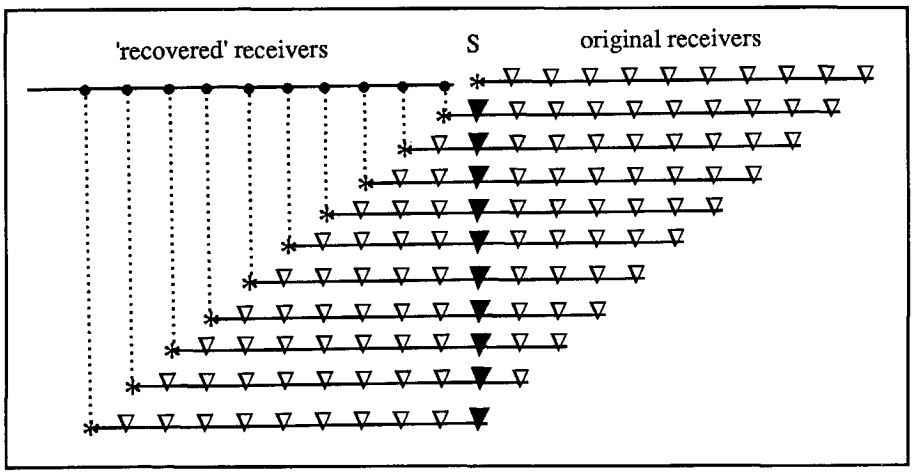

Fig.4.3.3: Recovery of missing negative offsets based on the reciprocity principle

negative offsets as well as traces at positive offsets contain valuable information in the shot-oriented data. When spatially transforming "non-causal" spatial functions, it is wrong to assume that the value of the function is zero at negative offsets; although, due to lack of the data at negative offsets (especially for marine data), this is often done. The reciprocity principle can be applied to the data prior to the double Radon transform to overcome this problem. The procedure is explained in Figure 4.3.3. The original shot gathers have receivers only at positive offset

locations. Using reciprocity, the first receiver with negative offset is recovered from the second shot gather and its first receiver, the second recovered receiver follows from the third shot gather and its second receiver, and so on.

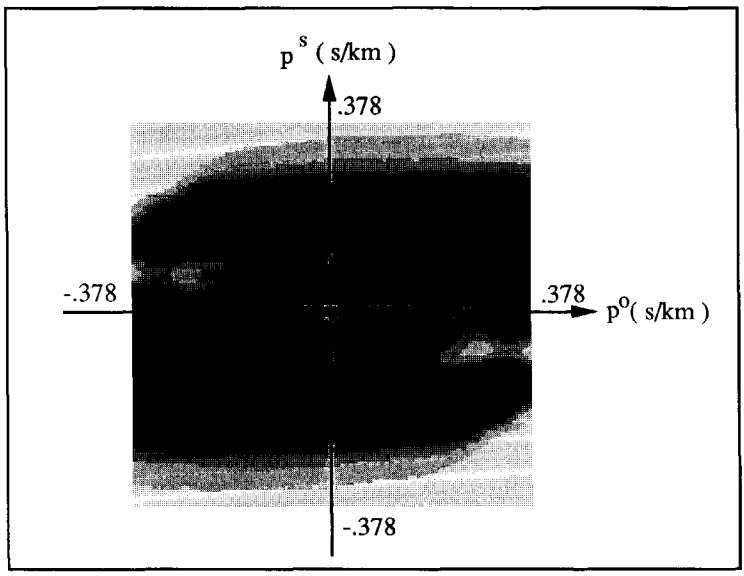

Fig.3.2.6: The energy density distribution for the triangle-shaped interface with split-spread geometry

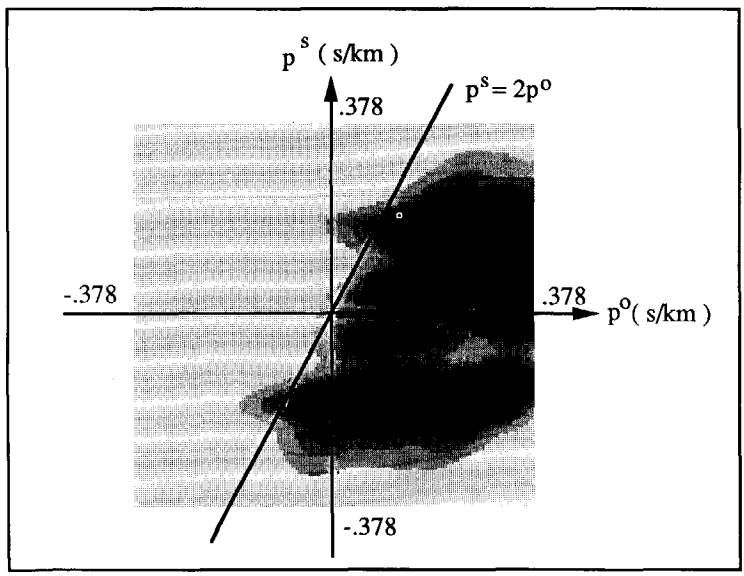

Fig.4.3.4: The energy density distribution for the triangle-shaped interface (shown in Figure 3.2.5), when the negative offsets were excluded from the data set prior to transformation

The shot gathers at the extreme end of the profile cannot be recovered completely, since there are no corresponding data. Also, missing near offsets obviously cannot be recovered.

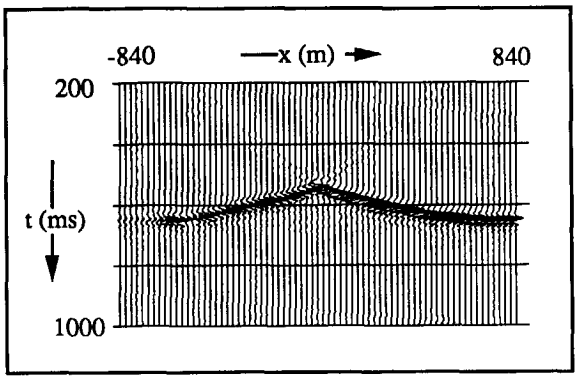

Fig.4.3.5: The image of the interface obtained from the data set modelled for the triangle-shaped interface (shown in Figure 3.2.5) without negative offsets

The influence of missing offsets on imaging is illustrated with a simple synthetic data set recorded over the triangle shaped interface which was shown in chapter 3, Figure 3.2.5. The energy density plot in Figure 3.2.6 (which is repeated here for convenience) was created for split-spread data which were double Radon transformed. When negative offsets are excluded from the synthetic data, and the data set with the end-off shooting geometry is double Radon transformed, the amount of information on the resulting energy density plot, as shown in Figure 4.3.4, is considerably decreased. Not only is the energy to the left of the $p^s = 2p^o$ line missing, but also the energy which is present to the right of this symmetry line is decreased. The little energy that is still present on the left is caused by transformation noise. The image of the interface obtained from this data set has also lost some information compared with the image

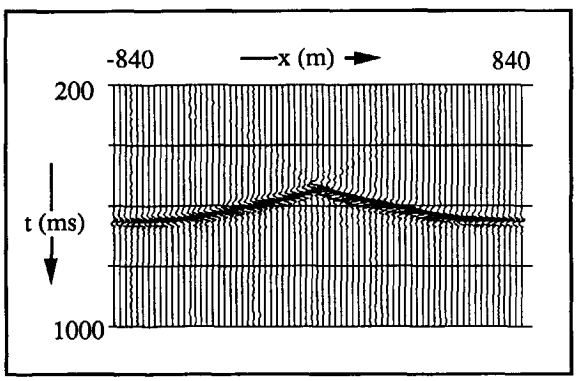

Fig.3.2.8: The image of the triangle-shaped interface, obtained from the data set modelled with the split-spread geometry

obtained from the full data set, as can be seen by comparing Figure 4.3.5 with Figure 3.2.8 (Figure 3.2.8 is also repeated here for convenience). This is especially pronounced at the extreme negative x^s positions, where the only information about the interface was at the negative offsets. Nevertheless, the image is rather good, even though the negative offsets were completely excluded from the data.

4.4 RESOLUTION ASPECTS

4.4.1 Limits of the p^o - p^s range

It was shown in chapter 3 that the values for p^o and p^s are limited to the range given by equation 3.2.3, which was derived by imposing the condition that the vertical slowness function needs to be real. The Radon transformation, as explained in chapter 2, was derived with the assumption that the offsets of the data recording, x^r and x^s, were infinite. Thus, the limits given by equation 3.2.3 can be considered as theoretical limits, which cannot be achieved in practice. A more realistic allowable range can be determined by taking into account the limited offsets of the data.

The limiting value of p^o in equation 3.2.3 implies that the emergence angle needs to be $i^u = 90^o$, to produce $sin\ i^u = 1$. This, in turn, means that the upgoing ray will be recorded by a receiver positioned at infinity. From the geometry of Figure 4.4.1 it is clear that, when the last receiver in a shot gather is at the maximum distance x^r, the limit for p^o becomes

$$|p^o| \leq \frac{|x^r - x|}{c\sqrt{(x^r - x)^2 + z^2}}. \qquad (4.4.1)$$

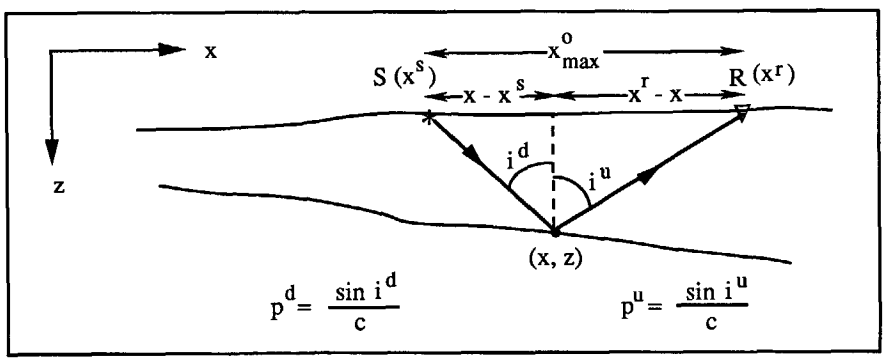

Fig.4.4.1: The geometry showing the limits on p^o and p^s values

By introducing the offset coordinate instead of the absolute receiver coordinate, as was done in equation 2.5.3 and as follows from Figure 4.4.1, the limit for the receiver ray parameter p^o becomes dependent on the maximum offset x^o_{max} as

$$|p^o| \leq \frac{\left|x^o_{max} - (x - x^s)\right|}{c\sqrt{\left[x^o_{max} - (x - x^s)\right]^2 + z^2}}. \tag{4.4.2}$$

The same reasoning applies for the downgoing ray, and the limiting value for p^d, derived from the geometry of Figure 4.4.1 is

$$|p^d| \leq \frac{|x - x^s|}{c\sqrt{(x - x^s)^2 + z^2}}. \tag{4.4.3}$$

By recalling the relation between p^d and p^s, given by equation 4.2.7, the limit for p^s becomes

$$|p^s| \leq |p^o| + \frac{|x - x^s|}{c\sqrt{(x - x^s)^2 + z^2}}. \tag{4.4.4}$$

The sum of the two numerators in inequalities 4.4.2 and 4.4.4 equals the maximum recorded offset x^o_{max}. Thus, the limiting value for both p^o and p^s depends on the maximum recorded offset, as well as on the depth to the interface and the seismic velocity. Since the maximum recorded offset is the only controllable parameter, it follows that long offsets need to be recorded if deep steep interfaces are to be imaged.

The limitation on p^o and p^s values in practical situations is caused by the lack of near offsets as well. Missing near offsets are common in marine data, but not always in land data. In the absence of near offsets, the small values of p^o and p^s, around zero, are also unreliable. The range of reliable low values can be calculated by using near trace offset x^o_{min} instead of maximum offset x^o_{max} in inequalities 4.4.2 and 4.4.4.

4.4.2 Limits of imaging

The imaging equations derived in chapter 3 were based on the high frequency approximation, using the method of stationary phase. This method states that the main contribution to the integral comes from the points at which the phase is stationary, that is when its first derivative equals zero. Using this condition, the stationary point was determined and given by equation 3.2.10, which is repeated here as

$$p^s = q_0 \frac{\partial z}{\partial x}. \tag{4.4.5}$$

Thus, to obtain a complete image of an interface, the domain $\mathcal{D}(q_a)$ defined in equation 3.2.6 as $\mathcal{D}(q_a) : (p^s)^2 \leq 4/c_0^2 - q_a^2$, and selected by choosing a particular value of q_0, has to contain *all* the stationary points given by equation 4.4.5. This also means that the imaging line has to intersect all the constant dip lines in which there is some energy reflected from the

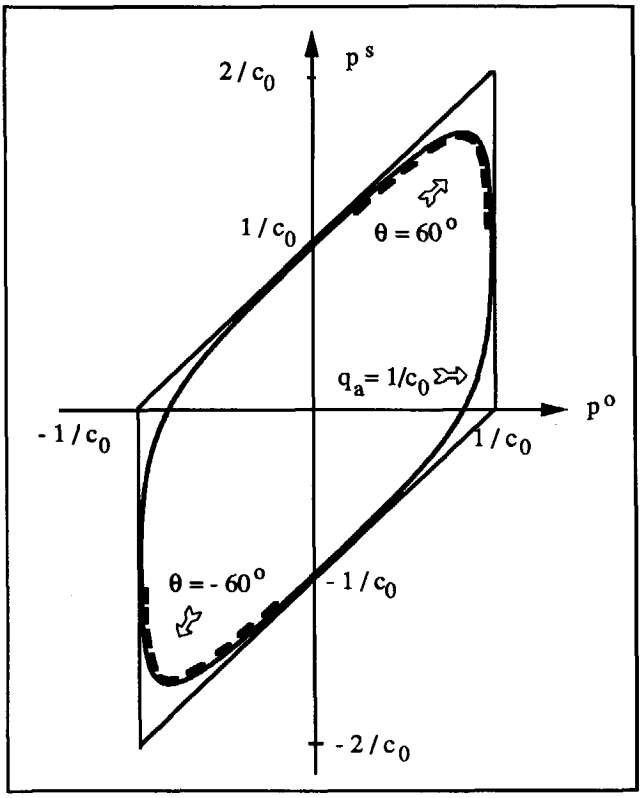

Fig.4.4.2: The imaging line with the limiting value of parameter a, $q_a = 1/c_0$ (solid line) overlaps the constant dip lines for $q = \pm 60^o$ (dashed lines)

particular interface. Substitution of the stationary point p^s into equation 3.2.6 which defines the domain $\mathcal{D}(q_a)$ leads to

$$\left(\frac{\partial z}{\partial x}\right)^2 \leq \frac{4}{c_0^2 q_a^2} - 1 . \qquad (4.4.6)$$

It follows from equation 4.4.6 that the chosen q_a should be as low as possible, in order to image interfaces with high gradients, that is, interfaces dipping at large angles. The lower limit of q_a was determined to be $1/c_0$ in equation 3.2.18. Substituting this limiting value for q_a in equation 4.4.6, the steepest interface to be imaged is determined by the limit of its gradient as

$$\left|\frac{\partial z}{\partial x}\right| \leq \sqrt{3}\,, \tag{4.4.7}$$

indicating that the maximum dip can be 60°. This is also shown in Figure 4.4.2, by displaying the dip lines for $\theta = \pm 60^{o}$ (dashed line), and the imaging line for $q_a = 1/c_0$ (solid line). The two dip lines are completely overlapped by the imaging line, and the dip lines for dips higher than 60° can not be intersected by the imaging line.

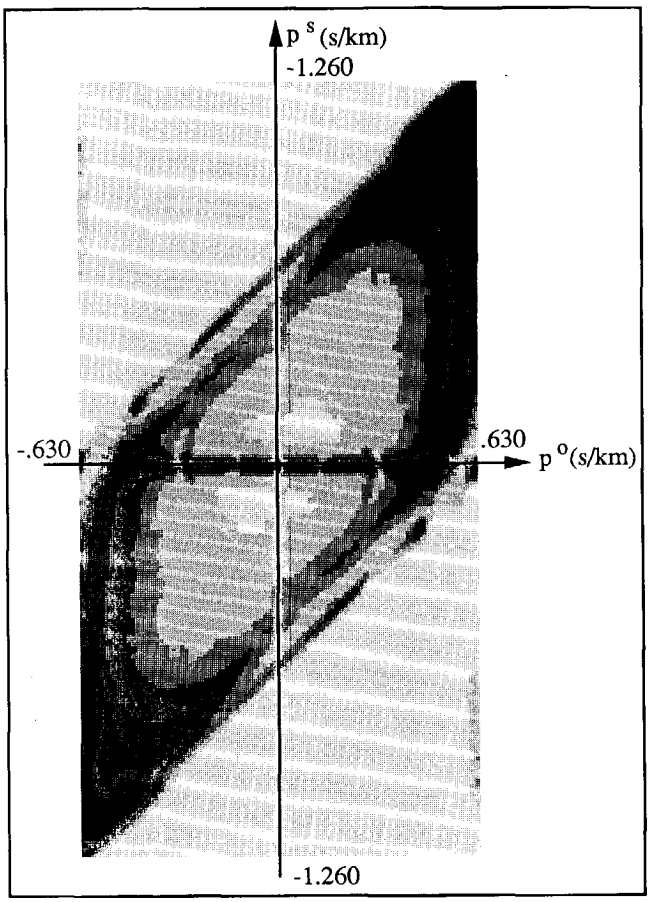

Fig.4.4.3: The energy density distribution for the syncline model of Figure 1.1.3.

In practice, some of the image of the steeply dipping reflectors is recovered by summing the diffraction energy from the steeply dipping events, which appears inside the limiting image line in p^o - p^s space. This is shown by an example of the syncline model discussed in chapter 1, which has steeply dipping flanks. The energy density plot in the p^o - p^s plane, shown in Figure 4.4.3, indicates the presence of energy reflected from a very steeply dipping interface, with dips

approaching $\pm 90^{o}$. To image this interface, the data selection into imaging planes was repeated several times, with a number of values of q_a. The resulting image which was displayed in Figure 1.1.3d (which is repeated here for convenience), obtained by summing these partial images, indicates a clear picture of the syncline.

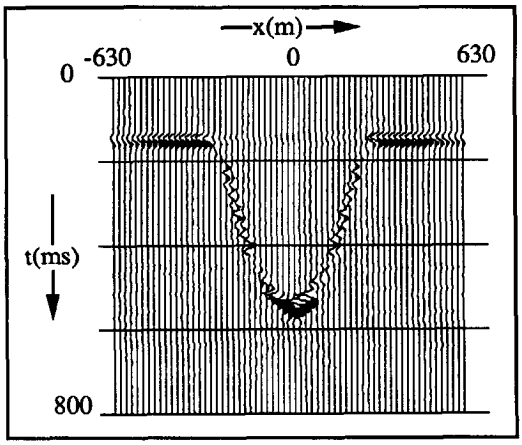

Fig.1.1.3d: The migrated section of the syncline model

As long as the energy reflected from a discontinuity is present in the data, it can be imaged. But a very steep reflector, for example a fault plane with dip approaching 90^{o}, will be represented on a migrated section as a disruption in the continuity of the reflectors, rather than a reflector itself. Taking into account the limits of the p^{o} and p^{s} values given by equations 4.4.2 and 4.4.4, it is likely that the energy reflected from steep fault planes will *not* be present in the data.

4.5 WAVELET DISTORTION

The data transformation from the t - x domain to the τ - p domain causes distortions of the original waveform. The factors causing these changes include interpolation, integration, and selective filtering effects.

4.5.1 The interpolation effect

As described in section 2.6.2 of this thesis, there are three steps to be performed to obtain the τ - p data from the t - x data:

1) $t \rightarrow \omega$, the temporal Fourier transform,
2) $x \rightarrow K_x$, the spatial Fourier transform, and
3) $K_x \rightarrow p$, where $p = K_x / \omega$, mapping to the regular p-grid.

After the first two steps, that is after the two Fourier transforms, the data still can be recovered exactly. However, the third step requires interpolation, which in effect introduces new information. Both the temporal and the spatial Fourier transforms are orthogonal transforms; it is

the third step that makes the Radon transform *non*-orthogonal. The changes to the waveform caused by the interpolation are irrecoverable.

Since interpolation is an important step in the procedure for the Radon transform (as it is in most seismic processes) the question is raised of what interpolation to use. The interpolation problems have been extensively studied in the literature. The comparison of interpolation methods related to the Radon transform can be found in Benoliel et al. (1987) and Vissinga (1992). When comparing the results of recovering a wavelet by linear interpolation and the cubic spline interpolation (Vissinga, 1992), the cubic spline doubtless produces results with higher accuracy at greater expense. However, when the interpolation is incorporated into the Radon transform algorithm, the advantage of the more expensive, higher order interpolation is lost. This conclusion applies even more strongly to field data (Benoliel et al., 1987).

To take the best of the low cost and high accuracy, a three-point polynomial interpolation, which follows from Lagrange's interpolation formula (Froberg, 1965) is implemented in the double Radon transform algorithm. The function $f(x)$ to be recovered at position x, is known at three points x_1, x_2, and x_3, such that $x_3 > x > x_2 > x_1$. If $w = x - x_2$, and $\Delta x = x_3 - x_2 = x_2 - x_1$, the function is recovered by applying

$$f(x) = \frac{w^2}{2(\Delta x)^2}\left(f(x_3) - 2f(x_2) + f(x_1)\right) + \frac{w}{2\Delta x}\left(f(x_3) - f(x_1)\right) + f(x_2). \qquad (4.5.1)$$

This three-point interpolator is only a fraction more expensive than linear interpolation and significantly less expensive than the cubic spline interpolator. On the other hand, when implemented with Fourier transforms its accuracy approaches that of the third-order interpolators.

4.5.2 Integration effect

To obtain the data in a regular p-grid, division of constant K_x values by frequency ω is required. This operation causes changes in both the amplitude and the phase of the input wavelet, and as a consequence, the waveform in the τ - p domain is changed compared with the waveform in the t - x domain. When the τ - p transformation is considered as a slant stack, where the summation of the amplitudes along the slant lines is performed, the described waveform change caused by $1/\omega$ corresponds to integration of the wavelets. Thus, the application of the inverse operation, that is differentiation, can be applied to the τ - p transformed data to correct for this wavelet change.

4.5.3 Filtering effect

To avoid aliasing during the mapping from the K_x-grid to the p-grid, the anti-aliasing criterion has to be satisfied

$$\omega p \leq K_x^N = \frac{2\pi}{2\Delta x}. \tag{4.5.2}$$

As shown in Figure 4.5.1, the equation of the $K_x = constant$ line in ω - K_x space becomes an equation of hyperbola in ω - p space. To satisfy the inequality 4.5.2, all the data which appear outside the limits of the hyperbola are replaced by zeros. As a consequence of this selective filtering, another distortion of the wavelet is introduced. This effect also contributes to the non-orthogonality of the Radon transform, and cannot be compensated for. The amount of distortion depends on both the ray parameter and frequency values, and it is observed in the τ - p data as the waveform change which is particularly noticeable on traces with high p-values.

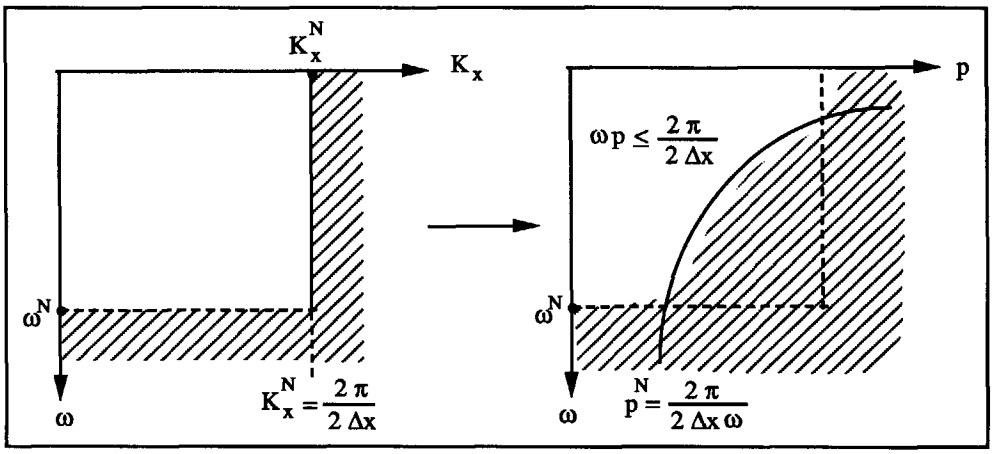

Fig.4.5.1: The anti-aliasing condition when mapping from K_x-ω space to p-ω space

In addition to the limits of the p^o - p^s range discussed in section 4.4.1, the inequality 4.5.2 imposes another limitation on the maximum p^o and p^s values. To minimize this effect, both Δx^s and Δx^r need to be small, in agreement with the resolution required.

4.5.4 The double Radon domain

After the data have been double Radon transformed, there are still two more interpolations to be performed during imaging: first, when the data are selected into the imaging surfaces, and second, when the time is scaled into two-way travel time after the image in the time domain has been obtained. For consistency, the three-point polynomial interpolation defined in equation 4.5.1 is used.

It was explained that transforming the data to the τ - p domain has an integration effect on the data, which can be corrected for by multiplication by ω during the inverse transform. Imaging in the double Radon transformed domain involves two forward Radon transforms and one inverse transform. Thus, there is an additional correction for the integration to be performed.

The frequency scaling filter, as explained in chapter 2, arises when the data are double Radon transformed, and differs with the given configuration as

$$\begin{aligned} &\text{3D} \quad : \quad -4\,i\,\omega\,c_0\,q_0^r\,q_0^s \\ &\text{2.5D} \quad : \quad 8\pi\sqrt{-i\,\omega\,c_0\,q_0^r\,q_0^s} \\ &\text{2D} \quad : \quad -8\pi\,i\,\omega\sqrt{q_0^r\,q_0^s} \quad . \end{aligned} \tag{4.5.3}$$

In the 2D and 3D configurations, the $i\omega$ factor corresponds to the differentiation operator, which corrects for the integration effect of the forward Radon transform. The $\sqrt{-i\omega}$ factor in the 2.5D configuration is the half-differential operator, and similarly to the 2D and 3D configurations, it has the function of differentiation.

The synthetic example showing a horizontal strip before and after migration, Figure 1.1.1, was modelled by summing diffractions from all point scatterers along the interface, and as such represents the 2.5D case. A detail from Figure 1.1.1, displayed in Figure 4.5.2, illustrates the wavelet before migration (trace 1) and after migration with all proper corrections (trace 2), as well as the difference between the two (trace 3). The resemblance between the wavelets before and after migration is quite good, in spite of their rather large difference, which is probably due mostly to interpolation effects.

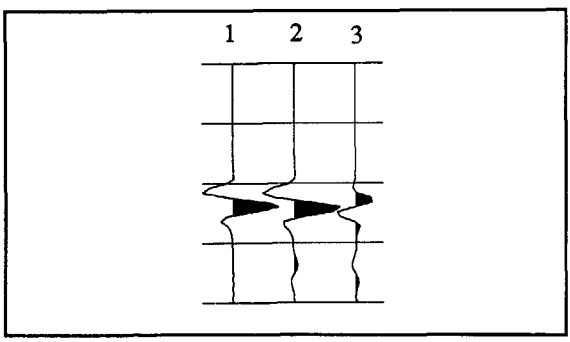

Fig.4.5.2: A detail from the section over the horizontal strip of Figure 1.1.1(c) before migration (1), after migration (2), and the difference between the two (3)

In summary, regardless of the wavelet changes in the double Radon transform, the interfaces are still properly imaged. The most important influence on the phase, the integration effect, can be corrected for, and the onset of the wavelet indicates the position of the interface. Further, the result of the imaging does not depend on the amplitude of the wavelet. This also implies that the impedance contrast does not influence the imaging, since only the phase information is utilized in imaging.

In the frequency scaling method, which was described in section 3.5, the wavelet suffers greater changes, which can be compared to the normal moveout (NMO) wavelet stretching

(Dunkin and Levin, 1973). Each frequency component is scaled by the normalized slowness function ψ, which is less than 1, meaning that the frequencies are compressed. The compression of the frequency spectrum corresponds to stretch in the time domain. Due to this additional waveform deformation, the frequency scaling method is less effective when it is desirable to preserve the wavelet during migration.

4.6 SEGMENTATION AND CONSISTENCY

The coordinate system for the double Radon transform is usually chosen such that the origin is positioned in the middle of the survey area. The p^o - p^s coordinate system is then also symmetrical with respect to the survey area, and its origin is connected to the origin of the x^o - x^s coordinate system. However, it is not necessary to set the coordinate system in this way. The data line can also be broken into segments so that each segment is separately transformed and imaged, and the total image is composed at the end from the individual segments. If the seismic line is very long, this would make not only the data handling easier, but would also improve the resolution of individual segments.

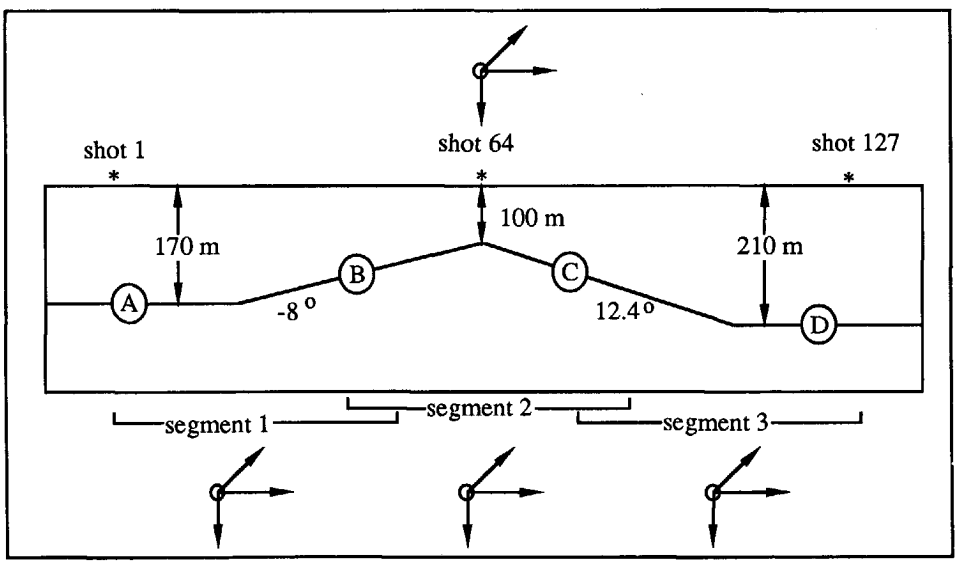

Fig.4.5.3: The asymmetric triangle-shaped interface, consisting of four segments A, B, C, and D. The seismic line is divided into three segments, 1, 2, and 3.

This procedure is illustrated with synthetic data, created by the diffraction summation from the asymmetrical triangle-shaped interface shown in Figure 4.5.3. The data set consists of 127 shots with Δx^s = 12 m, each shot gather consisting of 127 traces with split-spread geometry and Δx^r = 12 m. The whole data set is double Radon transformed, and its energy density plot in the p^o - p^s plane is displayed in Figure 4.5.4a, and the contents of the imaging plane is shown in Figure 4.5.5a. Both of these plots contain all four segments of the interface, as well as the migrated time image shown in Figure 4.5.6a.

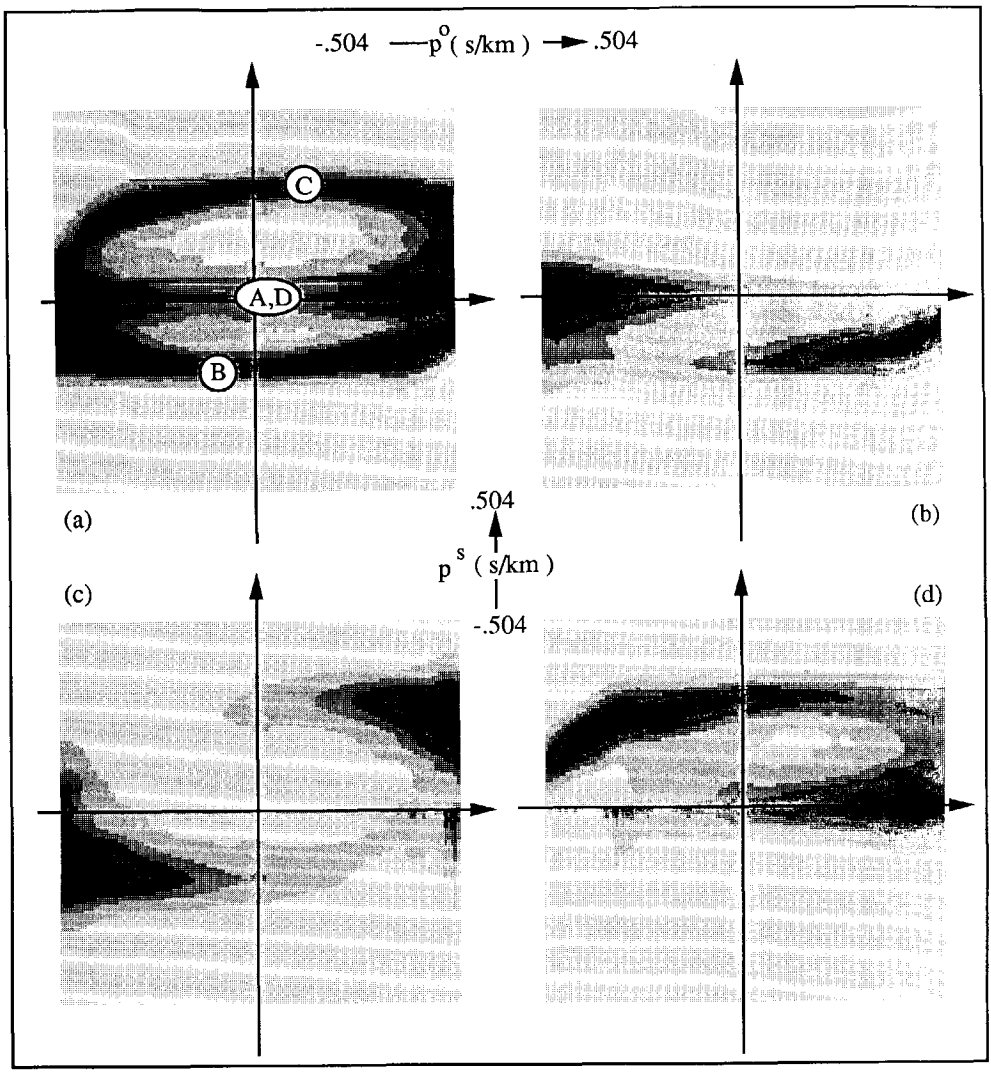

Fig.4.5.4: The energy density distribution for the asymmetric triangle-shaped interface of Figure 4.5.3 for (a) the whole line, (b) segment 1, (c) segment 2, and (d) segment 3. All four interface segments A, B, C, and D are recognized on plot (a)

To illustrate the consistency of the method, the original *t-x* data set is divided into three partially overlapping segments, as shown in Figure 4.5.3. The first segment contains shots 1-45, the second one 42-86, and the third one 83-127. Each of these segments is double Radon transformed with its own coordinate system. The resulting energy density plots are shown in Figure 4.5.4b - 4.5.4d. Each of the segments contains only a part of information contained in

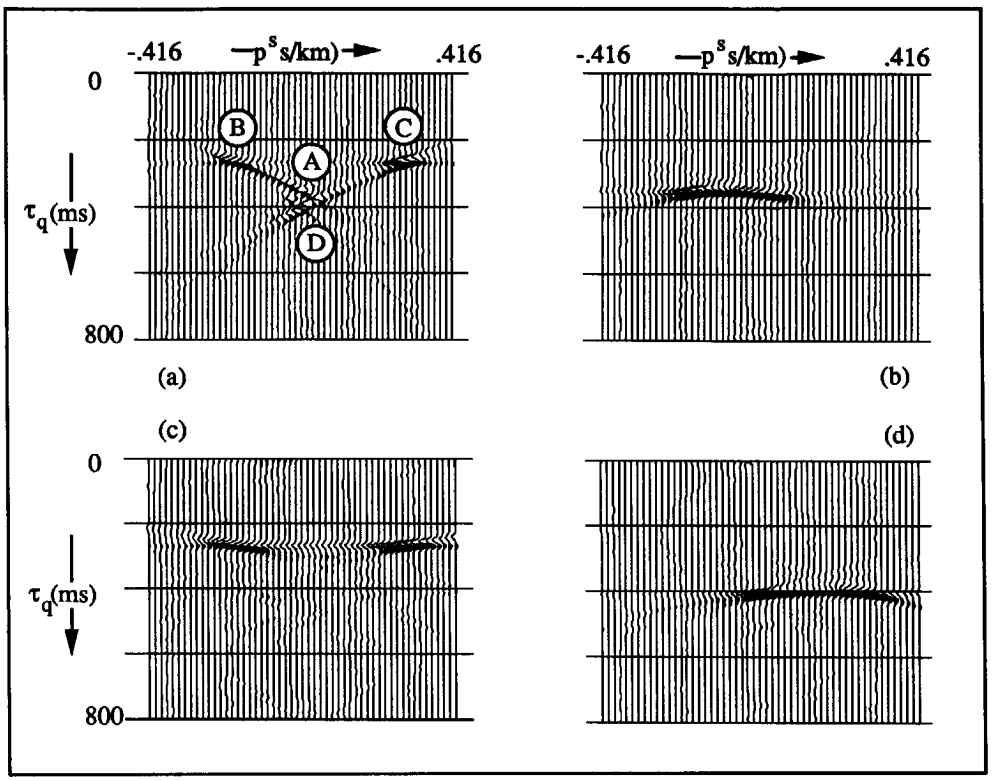

Fig.4.5.5: The energy contained in the imaging surfaces for the asymmetric triangle-shaped interface of Figure 4.5.3 for (a) the whole line, (b) segment 1, (c) segment 2, and (d) segment 3. All four interface segments A, B, C, and D are present on plot (a)

the whole data set in Figure 4.5.4a.

Imaging was applied to each of the segments, and the contents of the imaging plane for each of the segments are displayed in Figure 4.5.5b- 4.5.5d. Again, it is clear that each segment contains only part of the total energy. When transforming the contents of the imaging planes back to *t-x* space, the coordinate systems were adjusted to the original setting. The images obtained from each of the segments are displayed in Figure 4.5.6b - 4.5.6d. Finally, the total image is created by summing these partial images, and is displayed in Figure 4.5.7. This migrated image is identical to the image obtained from the whole data set, except that the end parts, containing the flat interface, are somewhat better resolved in the composite image of Figure 4.5.7. This is probably because the wraparound effect, which can be seen in Figure 4.5.6a, is avoided in Figure 4.5.7. since the large amount of zero traces in individual segments (Figure 4.5.5) act as a strong taper.

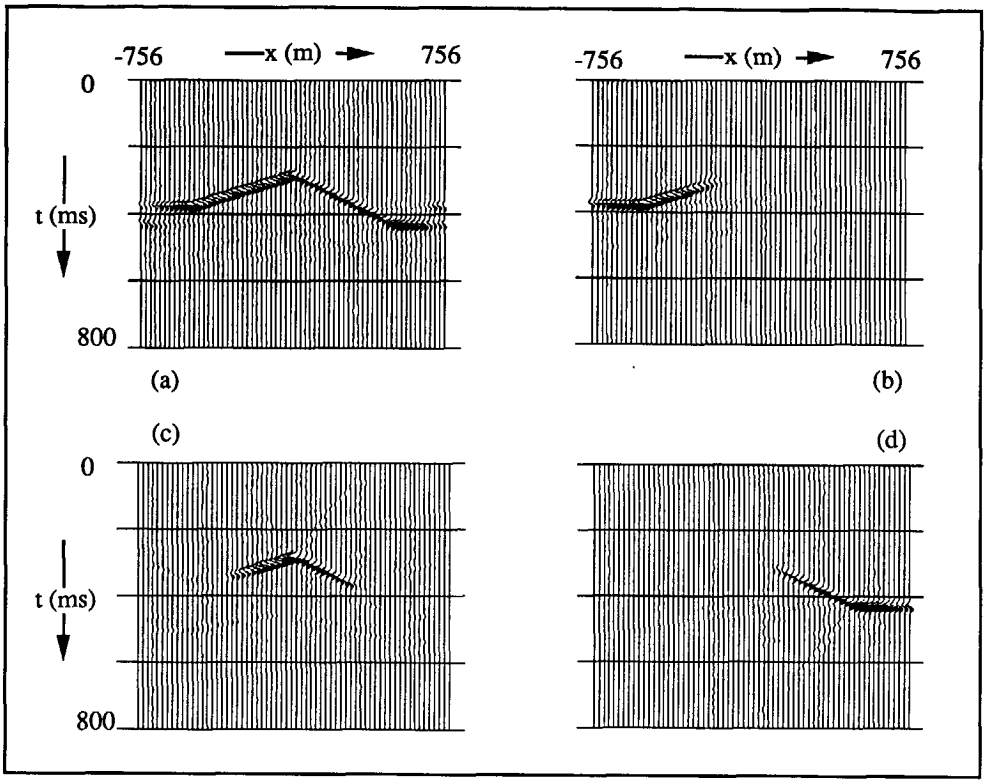

Fig.4.5.6: The interface image obtained for the asymmetric triangle-shaped interface of Figure 4.5.3 for (a) the whole line, (b) segment 1, (c) segment 2, and (d) segment 3

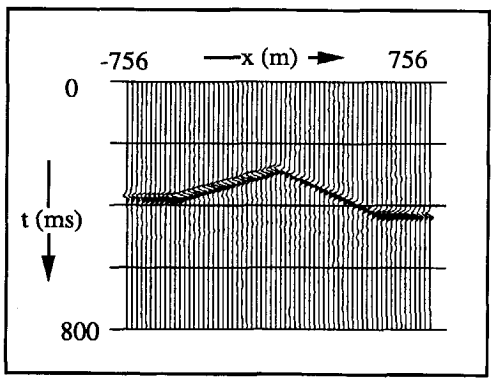

Fig.4.5.7: The composite time image for the asymmetric triangle-shaped interface of Figure 4.5.3, obtained by summing partial images for segments 1, 2, and 3

5

DATA EXAMPLES

5.1 INTRODUCTION

Most of the features of the p^o - p^s domain, and the migration performed in this domain, have been explained. To get the complete picture of the method, the performance of the algorithm on complex data needs to be examined. For that purpose, two data sets have been chosen: first, a complex synthetic example, the Marmousi data set, where the geology has the complexity which could be expected in the real world, but the experiment still has controlled geometry; and second, a field data set (Tubbergen data) acquired near Almelo, in the eastern part of Holland, which has the unpleasant features of real data, such as missing offsets, large shot intervals, noise, and so on.

5.2 MARMOUSI SYNTHETIC DATA SET

The Marmousi data set was created for the blind test of the workshop organized by P. Lailly and R. Versteeg at the 1990 EAEG meeting in Copenhagen (Versteeg and Lailly, 1991; Versteeg and Grau, 1991). Since its generation, this model has been highly popular to test new processing algorithms. The model, consisting of 160 layers, was created to simulate the complex geology of Angola. The major structural elements of the model are shown in Figure 5.2.1. This model was input to a 2D acoustic finite difference modelling programme. The resulting data set, simulating marine data acquisition with end-off shooting geometry, has the following parameters:

- 240 shots
- 96 traces per shot
- Spatial sample interval $\Delta x^s = \Delta x^r = 25$ m
- Near-offset trace at 200 m, far-offset trace at 2575 m
- Recording time 2.9 sec
- Time sample interval 4 msec

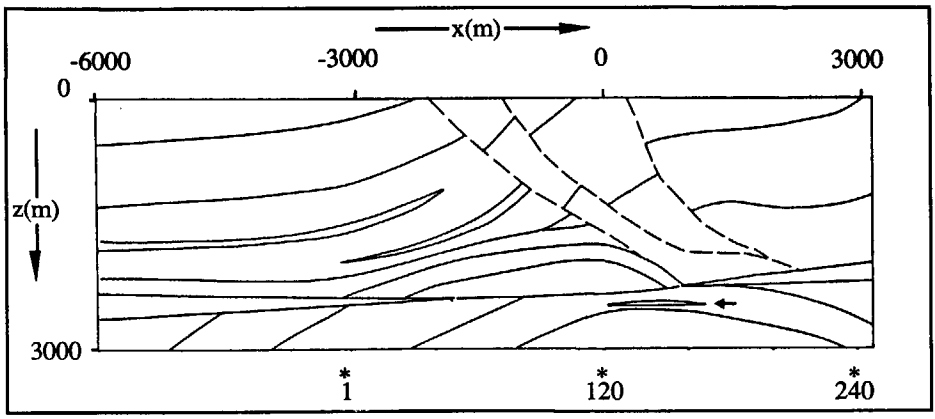

Fig.5.2.1: The depth model of the Marmousi synthetic data (with permission from EAEG)

The source was modelled as 6 independent identical waterguns at 8 m intervals, resulting in an array of 40 m length. The shot point position is in the middle of the source array, and the source depth was modelled at 8 m. The hydrophone group was modelled as 5 identical hydrophones at 4 m intervals, resulting in a receiver array of 16 m length. The streamer depth was modelled as 12 m. The positions of the first, middle and the last shots are indicated in the Figure 5.2.1. Because of the 2D geometry, the individual sources and receivers were lines, rather than points.

As explained in section 4.3, split-spread shooting geometry is prefered to end-off shooting for the spatial transformation. Thus, the reciprocity principle was applied to the Marmousi data, resulting in a split-spread data set. The shot gather at the shot position 1, with its positive offsets recovered using reciprocity, is shown in Figure 5.2.2. Due to the geometry of the Marmousi data acquisition, only negative offsets were available, and the positive offsets had to be recovered. The traces at far negative offsets in shot 1 are recorded over relatively smooth, slightly dipping layers. The traces at positive offsets already cover the complex middle part of the model, which is exhibited through the more complicated travel time curves. The overall appearance of this shot gather indicates that the global geology model is dipping at negative dips, since the apexes of the travel time hyperbolas are shifted to the positive offsets.

This split-spread data set was input to the double Radon transform programme with the following parameters:

- 127 p^o-traces
- 255 p^s-traces
- Trace increment $\Delta p^o = \Delta p^s = 0.008$ sec/km
- Maximum p^o value 0.504 sec/km
- Maximum p^s value 1.016 sec/km

The energy density plot for this double Radon transformed data set is displayed in Figure 5.2.3. The dominating energy is concentrated in the lower part of the p^o - p^s plane, indicating again that the trend geology is dipping at negative angles.

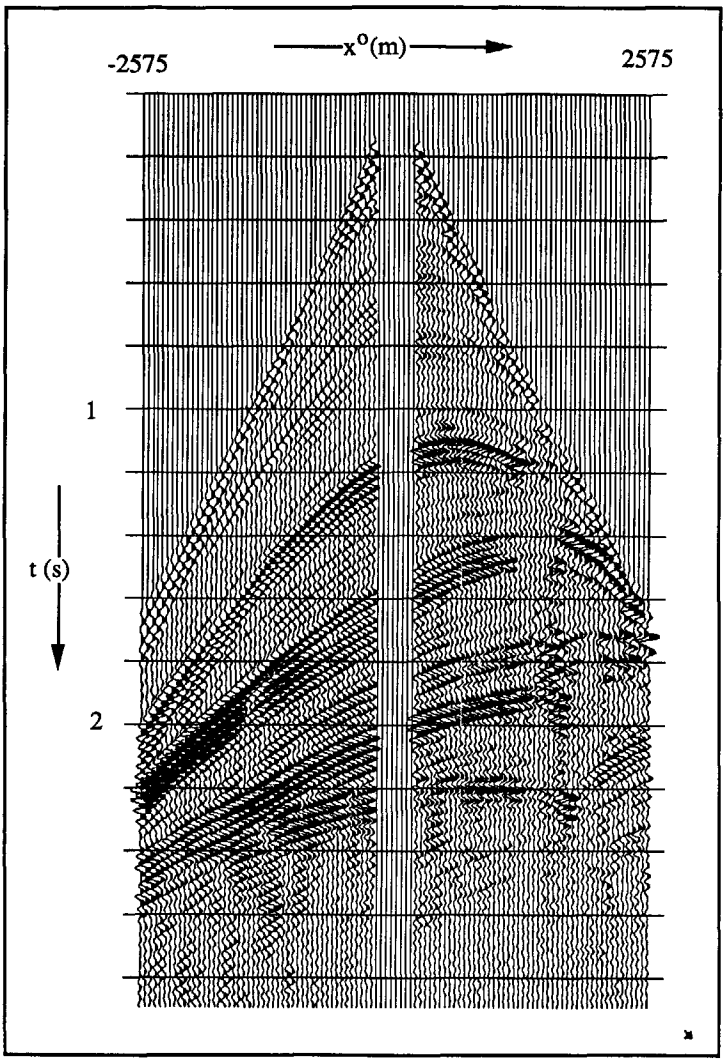

Fig.5.2.2: Shot gather 1, with its positive offsets recovered using the reciprocity principle

For the purpose of velocity analysis, the data in the $p^s = 0$ plane were extracted from the p^o - p^s data volume. This data set, displayed in Figure 5.2.4, was input to the τ-p velocity analysis program, and the resulting contour plot is shown in Figure 5.2.5. The velocity trend is quite clear from the contour plot, especially when the complexity of the input model is taken into account. Due to the dip separation in the p^o - p^s domain, reflections from horizontally layered structures are isolated in the $p^s = 0$ plane. The resulting velocity analysis is this simple, easy to pick, velocity contour plot. This estimated RMS velocity function was input to the imaging algorithm, with the double Radon transformed data. The imaging was repeated with a number of selected imaging lines. The contents of one of the imaging planes, displayed in Figure 5.2.6,

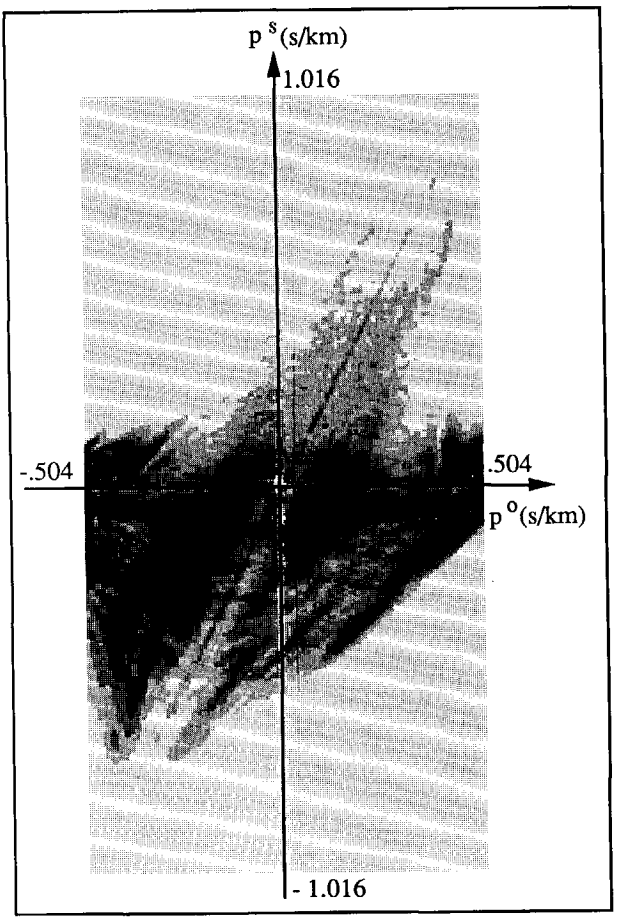

Fig.5.2.3: The energy density distribution in the p^o-p^s plane for the Marmousi data

indicate the complexity of the data. The available energy range decreases with increasing time, as the RMS velocity increases. This is in accordance with Snell's law: with increasing velocity, the range of maximum possible p-values (both p^o and p^s) decreases.

The data in each selected imaging plane were inverse Radon transformed and scaled to two-way travel time. The final output displayed in Figure 5.2.7 was obtained by summing the individual images.

The main reflectors, visible in the model in Figure 5.2.1, are all present in the resulting image. The three steep faults in the middle of the model are also recognized in the image, not as clear reflections, but rather as disruptions in the reflector continuity. Since this is a time migration, the propagation effects are not removed from the image of the lower reflections. This is especially noticeable in the image of the unconformity, which extends through the most of the depth model at about 2500 m as an almost horizontal interface, but in the time image appears as a dipping reflector at 2200 msec at the left end of the profile and at about 1700 msec at the right

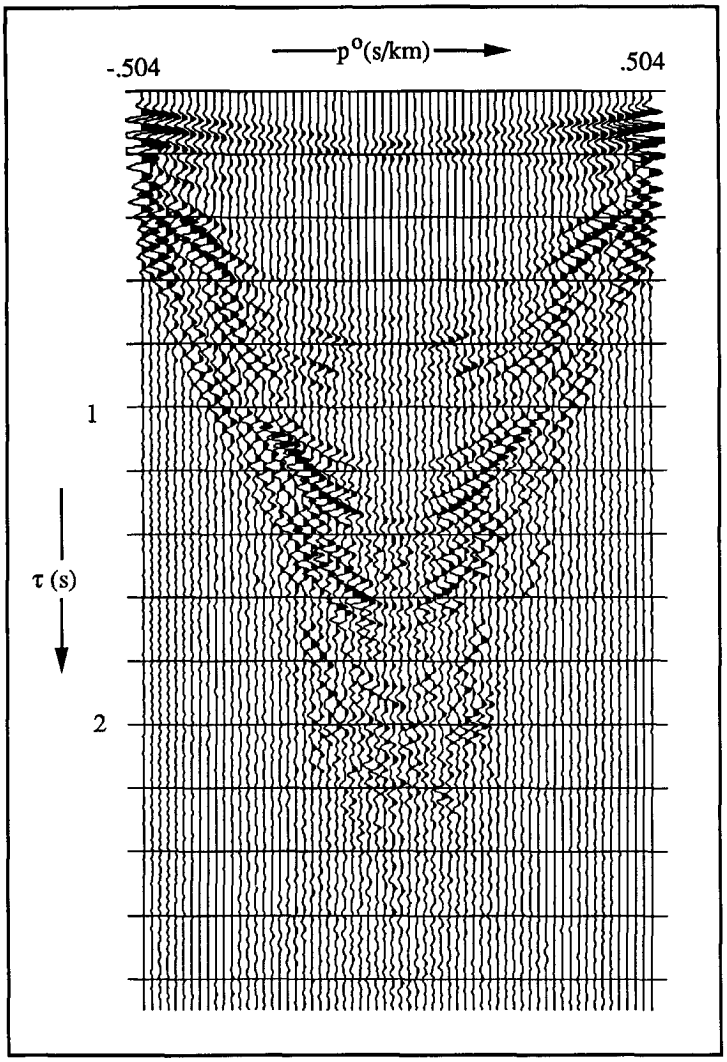

Fig.5.2.4: The data in the $p^s = 0$ plane

end, as indicated in Figure 5.2.7. Overall, the main features of the geological model are recovered.

For comparison, the result of the pre-stack depth migration, obtained with the *known exact* velocity model (Versteeg and Lailly, 1991) is presented in Figure 5.2.8. As could be expected, this is a very good image of the input structure, and without doubt, it is a better image than the one produced by the time migration in the double Radon domain. One serious drawback, however, makes it unattractive: to obtain this image, the *exact* velocity model was required as input to the migration. In other words, to obtain the image of the model, the model had to be known. On the other hand, the time image in Figure 5.2.7 was generated with a

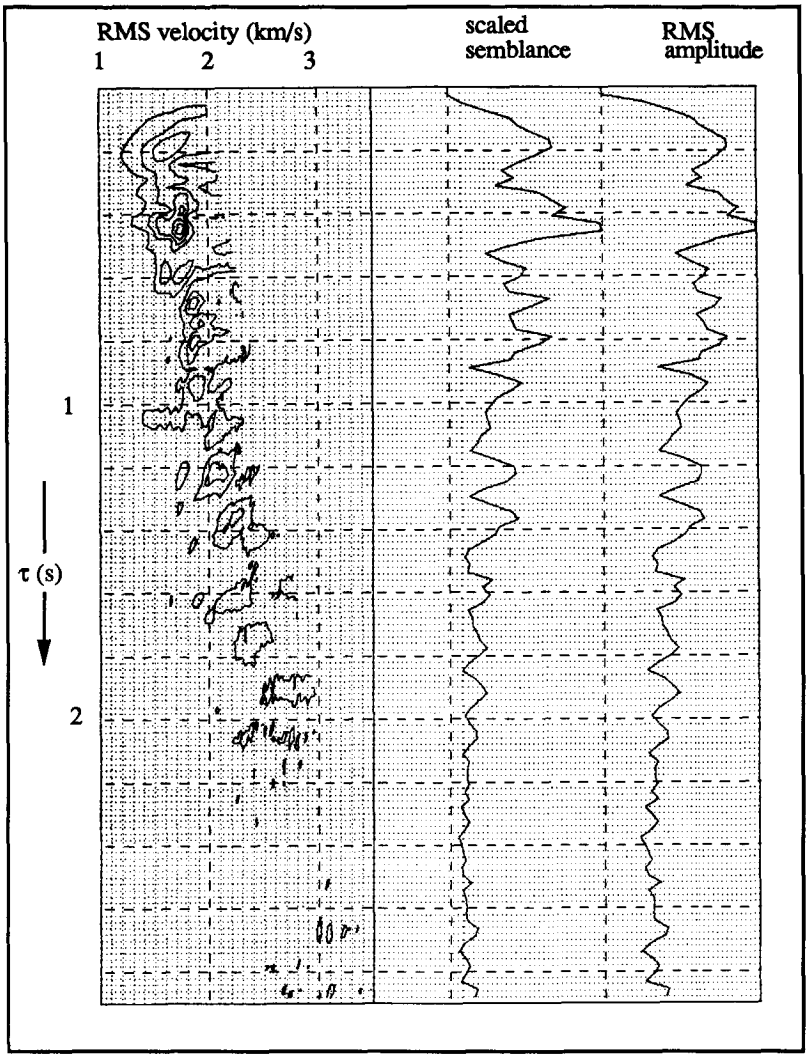

Fig.5.2.5: The contour velocity plot obtained from the τ-p velocity analysis on data in the $p^s = 0$ plane

background velocity model estimated *from the data.* Another advantage of the time image is the low cost required for its creation. To double Radon transform the Marmousi data set, the required time was 58 CPU minutes on a Convex 120 (with more than half of this time used for input/output). The time required for each imaging was about 10 CPU minutes, and this procedure was repeated eight times to obtain the final image displayed here. The pre-stack depth migration is a rather costly procedure; even more expensive is the velocity estimation for the depth migration, which requires a number (usually a large number) of trial migration runs. In this sense, the result of the pre-stack time migration, as presented here, could be used as a very

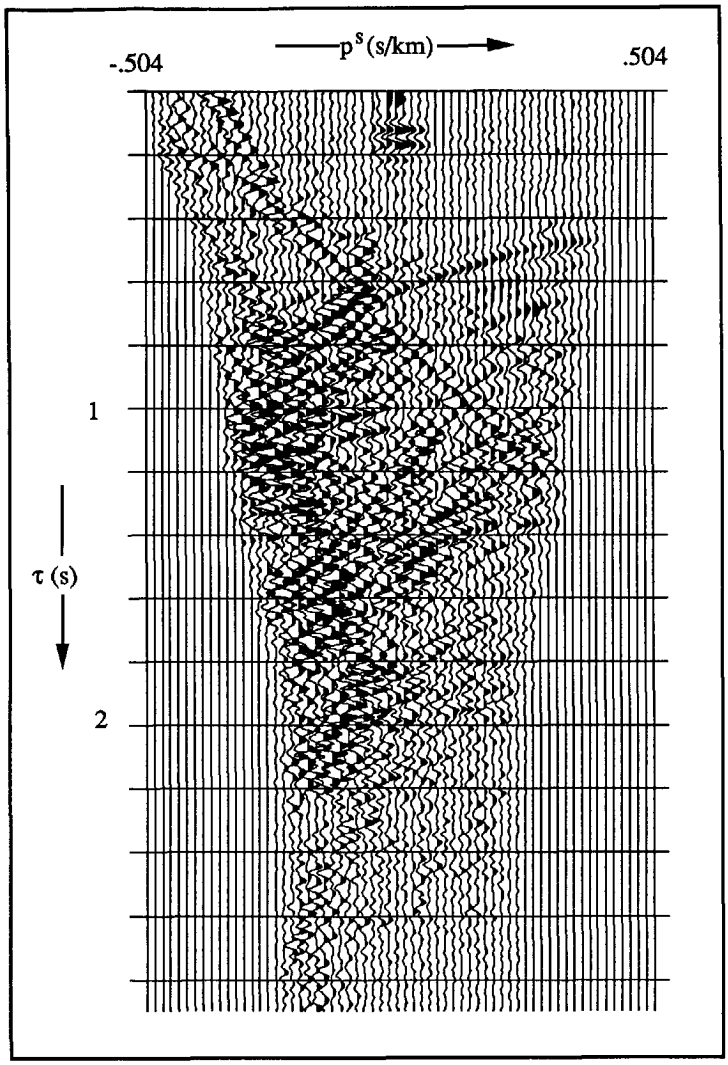

Fig.5.2.6: The energy contained in the imaging surface for the imaging line with a = 1.85. The amount of information decreases with with increasing RMS velocity. The edges are slightly tapered

good starting model for the depth migration, which should decrease the number of trial runs for the velocity estimation.

The migrated time section displayed in Figure 5.2.7 has a rather narrow band-pass filter applied to it, with the cut-off frequencies 0-10-15-25 Hz. When the section is displayed with the original frequency range of 0-10-30-45 Hz (Figure 5.2.9), some noise can be seen, especially in the middle, complex part of the model. According to the anti-alias criterion (equation 4.5.2), the

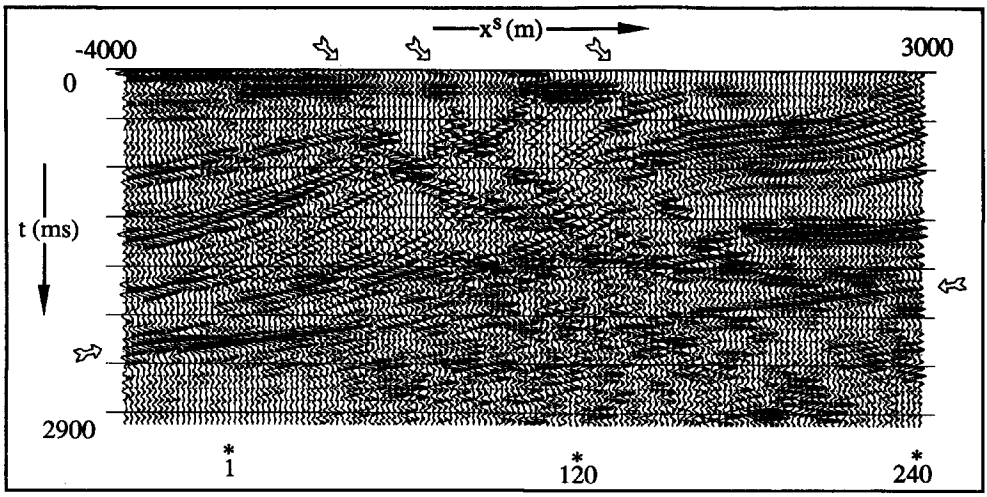

Fig.5.2.7: The result of imaging with time migration of the Marmousi data, band-pass filtered to 5-20 Hz.

maximum allowable frequency for $\Delta x = 25$ m and the maximum value of $p^s = 1.016$ sec/km is 20 Hz. In the middle of the model, where the steeply dipping interfaces are present, most of the information comes from the high p^s values. Thus, this information can be extracted from a limited range of frequencies. During the Radon transformation, the anti-alias filter is applied to reduce this type of noise. However, in order to allow all possible information to be passed, very short tapers are applied in both the time and space directions. The noise still present in the data can then be removed by a high-cut filter after the data have been imaged.

The reciprocity principle is valid when both sources and receivers can be approximated by points (or, for this 2D synthetic data set, lines). This is not the case for the Marmousi data set,

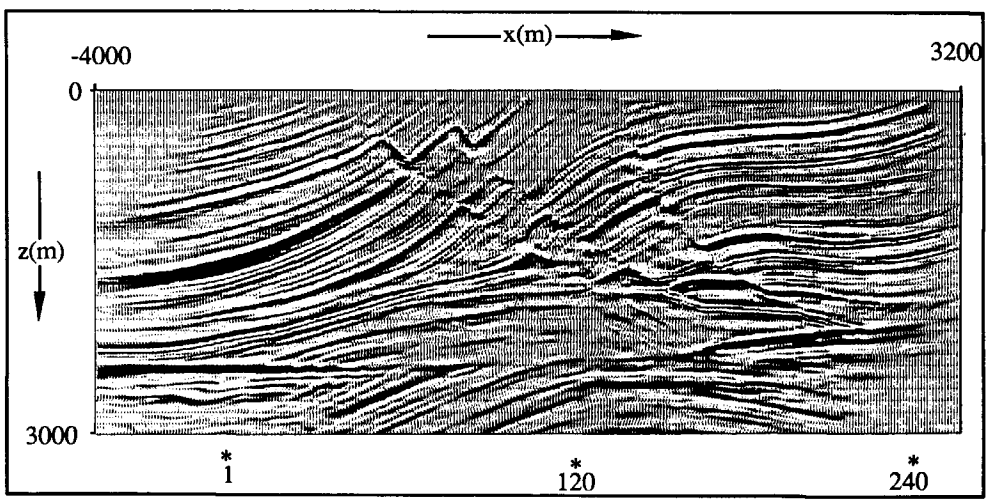

Fig.5.2.8: The result of depth migration of the Marmousi data, with the *exact* velocity model (with permission from EAEG)

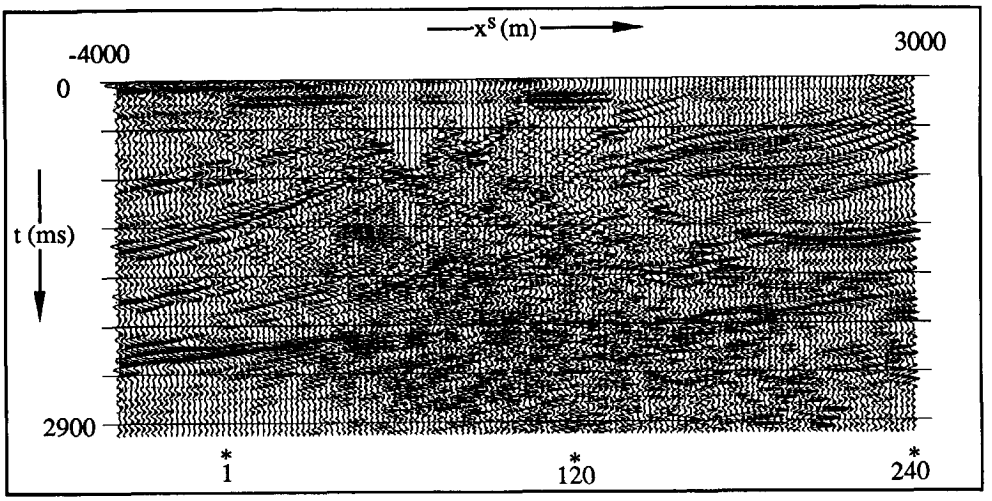

Fig.5.2.9: The result of imaging with time migration of the Marmousi data, with the original frequency content of 5-40 Hz.

with 40 m long source arrays and 16 m long receiver arrays. The source and the receiver directivity could then make the interchanging of the sources and the receivers invalid, which could be the cause for the higher frequency noise in the middle of the model. The directivity becomes important when the array size is of the order of the wavelength or greater (Ziolkowski, 1984). With the velocity of wave propagation in water of 1500 m/sec, the source directivity becomes important for frequencies higher than about 37 Hz, and the receiver directivity becomes important at a frequency of 94 Hz. Thus, for the frequency range utilized for the Marmousi data set, the size of the source and the receiver arrays does not cause directivity problems.

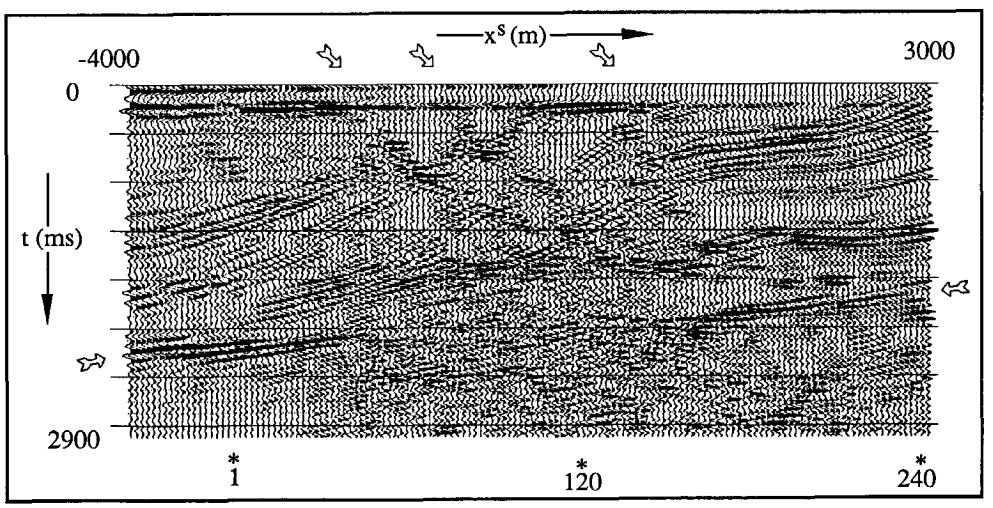

Fig.5.2.10: The result of imaging with time migration of the preprocessed Marmousi data (free surface effects removed), band-pass filtered to 5-20 Hz.

With source and receivers positioned at different water depths, the part of the wavelet caused by the source and receiver ghosts is not reciprocal. Also, the reverberations within the water layer make the wavelet rather long and ringy, which could be another reason for the noise in the middle of the Marmousi model. To test this possibility, the Marmousi data set which was preprocessed and described by Berkhout et al. (1990), was input to the imaging procedure. The preprocessing scheme used includes removal of the surface related multiple, as well as reverberations within the thin layer at both the source and receiver sides. The resulting migrated section, displayed in Figure 5.2.10, which appears with a rather compressed wavelet, still had to by narrow-band filtered, similarly to the section in Figure 5.2.7.

To satisfy the anti-alias criterion during inverse Radon transform (equation 4.5.2), Δp^s had to be kept sufficiently small for higher frequencies. Due to the size of the Marmousi data, Δp^s was chosen rather high, 0.008 sec/km, which was sufficient to pass frequencies up to about 20 Hz, which might be the reason for noise visible in Figure 5.2.7. Thus, a test run was performed for the Marmousi data set, with $\Delta p^s = 0.004$ sec/km and 509 p^s-traces, while all the other parameters were kept the same. However, the resulting time image, shown in Figure 5.2.11, still has the noisy appearance similarly to the image shown in Figure 5.2.7, and has to be narrow band-pass filtered.

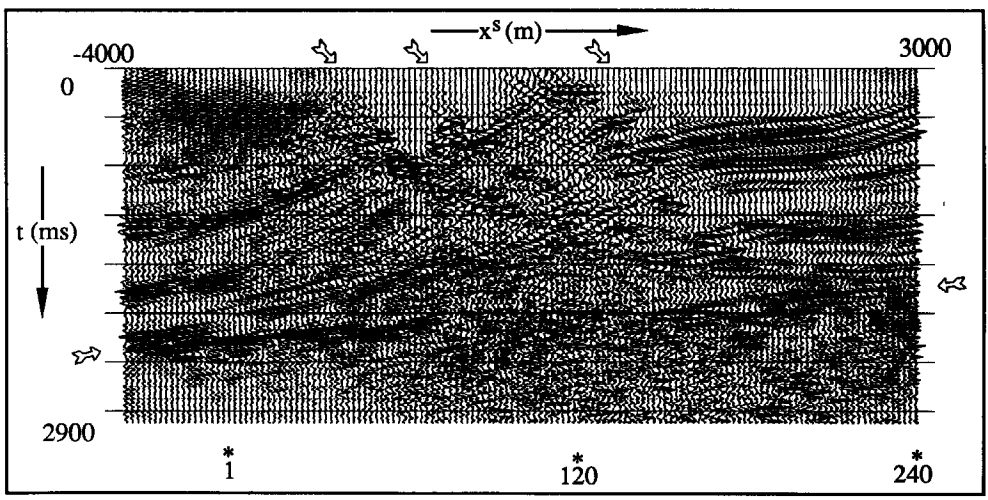

Fig.5.2.11: The result of imaging with time migration of the Marmousi data, with $\Delta p^s = 0.004$ sec/km, and original frequency content 5-40 Hz.

This leads to the conclusion that the noise in the middle of the Marmousi model probably originates from the violations of some basic assumptions, made in chapter 2. In particular, the locally plane layer assumption is specially violated in the middle, complex part of the model. Further, in this complex geology there is much more wave scattering other than the primary reflections, unlike the primaries-only assumption made in chapter 2 to develop this theory. This

scattered energy then maps into wrong places, which might be an additional cause of the noise in the middle of the model.

5.3 TUBBERGEN FIELD DATA SET

The Tubbergen data set was acquired as a part of the EEC sponsored project "The Inversion of Land Seismic Data". The experiment was designed to test and extend the theory developed for the one-dimensional inversion of seismic data (Koster, 1991), and to test the scaling law for determination of the signature of a dynamite source (Ziolkowski and Bokhorst, 1992).

The field experiment resulted in a data set with split-spread geometry, and the following parameters:

- 90 shots
- 240 traces per shot
- Shot sampling interval $\Delta x^s = 50$ m
- Receiver sampling interval $\Delta x^r = 10$ m
- Near-offset trace at $\pm$ 5 m, far-offset trace at $\pm$ 1195 m
- Recording time 4 sec (2 sec processed)
- Time sampling interval 2 msec

At each shot position, 4 shots with different charge sizes were fired in order to estimate the source signature using the scaling law. For the purpose of this thesis, only one shot per shot position was processed. Thus, the source for the Tubbergen data consists of 250 g dynamite placed in a single hole, 10 m deep. The receiver group consists of 12 geophones spread over 20 m length.

The main challenge for processing the Tubbergen data with a spatial-transform method comes from its irregular geometry. To avoid various obstacles in the field, the data set resulted in skipped shots and shot distances often bigger or smaller than 50 m. Furthermore, at both ends of the line, the split-spread configuration was replaced by the end-off shooting. The geometry of the data acquisition for the Tubbergen data, displayed in Figure 5.3.1, shows these irregularities. The gaps in the data resulting from the skipped shots could be filled in either by interpolating between the shots, or by using the reciprocity principle. It was decided to use reciprocity and thus use all the information that already exists in the data, rather than introduce new information by interpolating between shots. Reciprocity is applied after the static corrections had been applied and the ground roll removed by *f-k* filtering, and a 15-60 Hz band-pass filter to avoid aliasing during transforms. A typical recorded shot gather, from the middle of the line, is displayed in Figure 5.3.2, and one of the recovered shots is displayed in Figure 5.3.3. The quality of the recovered shot is not as good as the quality of the recorded shot, mainly because not all the traces in the shot gather could be recovered (the traces displayed in Figure 5.3.3 are not at the equal distances, and missing traces are replaced by zeros), since the shots were fired only at every fifth receiver group position. Nevertheless, some of the

information still could be recovered, and the new data set, resulting in 117 shots at a regular interval of 50 m, was input for the double Radon transform.

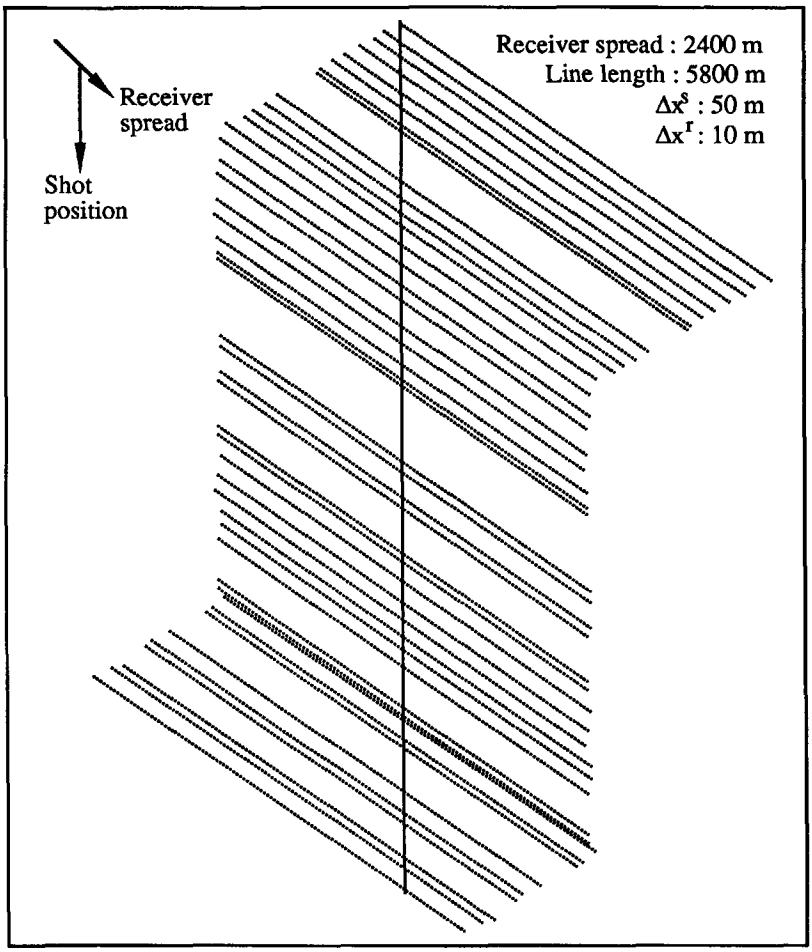

Fig.5.3.1: The geometry of the data acquisition for the Tubbergen data: the solid line represents the seismic line, and the dotted lines indicate the receiver spread

From conventional processing of the data it was clear that there are no steeply dipping interfaces in the Tubbergen data. Therefore, the complete p^o-p^s range is not needed. The data were transformed with the following parameters:

- 127 p^o-traces
- 127 p^s-traces
- p^o-trace increment $\Delta p^o = 0.004$ sec/km
- p^s-trace increment $\Delta p^s = 0.006$ sec/km
- Maximum p^o value 0.252 sec/km
- Maximum p^s value 0.378 sec/km

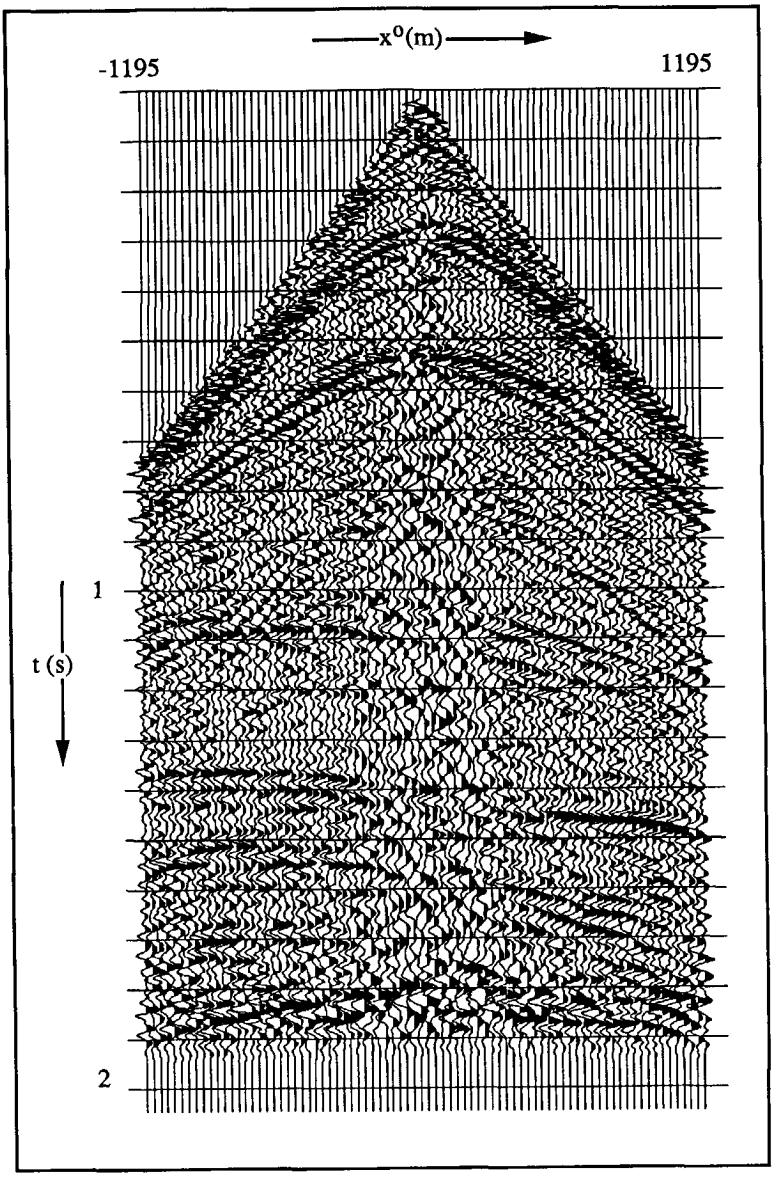

Fig.5.3.2: A typical shot gather recorded in the middle of the line

The energy density plot for this double Radon transformed data set is displayed in Figure 5.3.4. The energy distribution indicates relatively smooth subsurface geology. The RMS velocity function was estimated from the $p^s = 0$ plane, similarly to the procedure applied to the Marmousi data. This estimated RMS velocity function was used to migrate the data. The imaging was repeated several times, and the final output, displayed in Figure 5.3.5, was obtained by summing the result of each imaging.

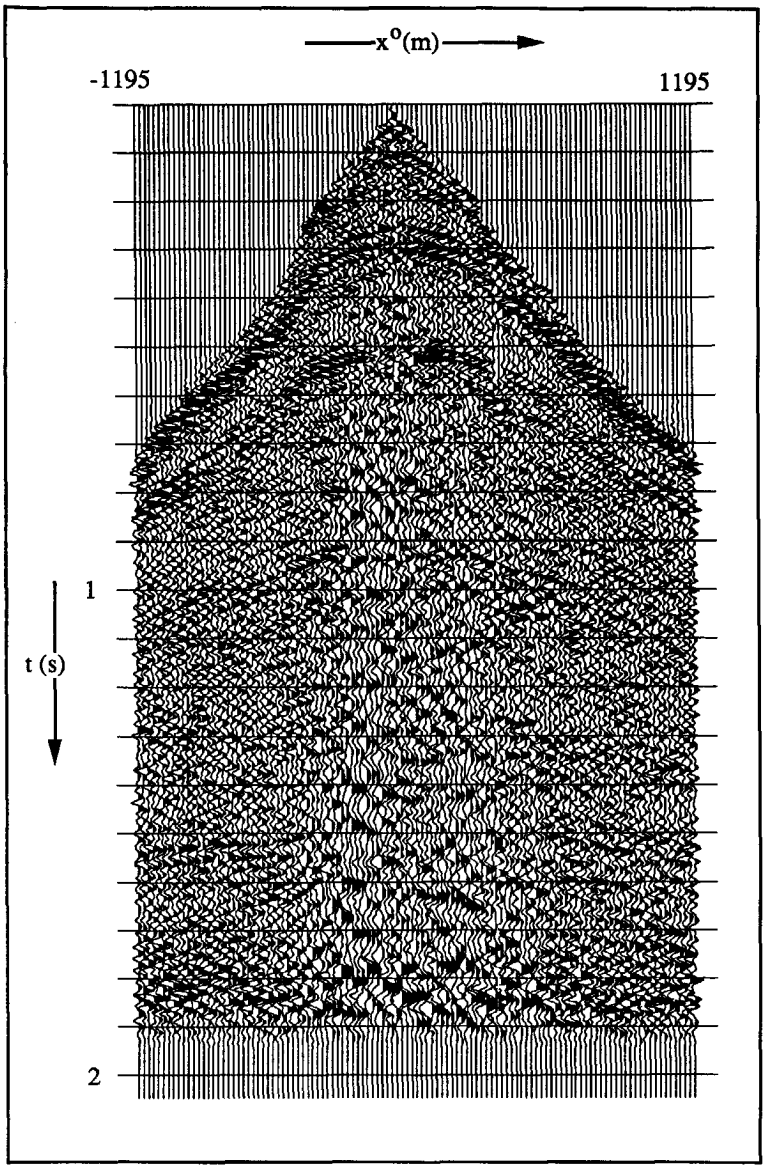

Fig.5.3.3: A shot gather recovered using the reciprocity principle (missing traces are not shown)

Due to a rather large shot distance, $\Delta x^s = 50$ m, the data had to be band-pass filtered up to 50 Hz prior to transformations. Further, with reciprocity only part of the data could be recovered, and a large amount of zeros instead of real data values was input to transformations. Because of this, it was decided to recover the missing data with spline interpolation, as well as to decrease the shot distance from 50 m to 25 m. This was done after the first Radon transformation, in planes of constant p^o, by interpolating with a spline function the real and the

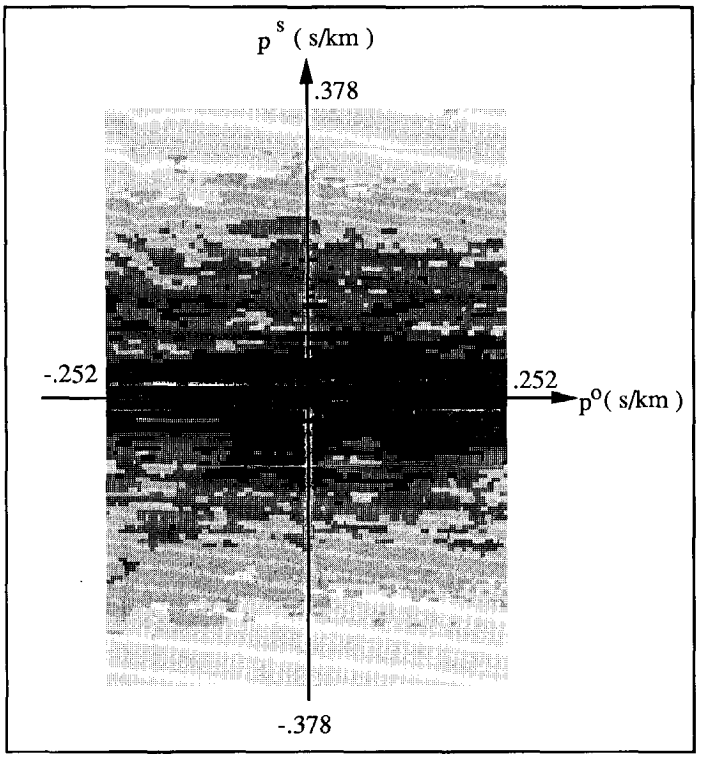

Fig.5.3.4: The energy density plot for the Tubbergen data

imaginary part of the complex trace separately (Ziolkowski and Bokhorst, 1992). After this, the procedure was the same as for the data recovered by reciprocity principle. Even though a higher frequency content was preserved with smaller Δx^s, the resulting time image, shown in Figure 5.3.6, has a resolution similar to the time image shown in Figure 5.3.5. In both of these images, some noise is visible at shallow parts which increases towards the ends of the sections. This is caused by the irregular offsets in shots at the beginning and the end of seismic line.

For comparison with the conventional processing, the stacked section is displayed in Figure 5.3.7. Post-stack migration was performed on this section using the *f-k* algorithm, and the result is displayed in Figure 5.3.8. The velocity function used for the *f-k* migration was derived from the stacking velocities, independently of the RMS velocity derived from the p^o - p^s data. The *f-k* migration does not perform satisfactorily at about 1.5 sec and -900 m lateral distance, where the velocity changes abruptly. Hence, finite difference migration was applied with the interval velocities derived also from the stacking velocities, and the result is displayed in Figure 5.3.9. Since the finite difference migration is not sensitive to high velocity contrasts, it produced a migrated section which is of better quality than the result produced by the *f-k* migration. Also, the not too complex geology of the Tubbergen area allows a rather good quality stacked section to be be produced (Figure 5.3.7), which is the main prerequisite for post-stack migration to perform satisfactorily.

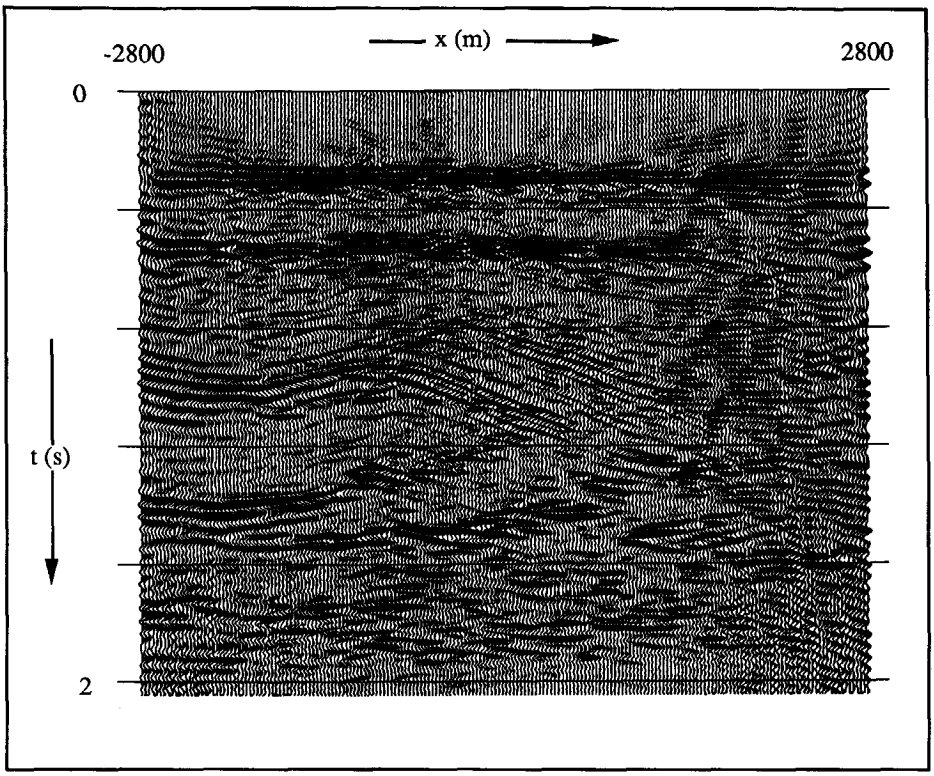

Fig.5.3.5: The result of imaging the Tubbergen data (reciprocity principle)

On the other hand, processing with the spatial transform over shot coordinates has the disadvantage in the case of Tubbergen data, due to its irregular shooting geometry. This problem can be overcome using either the reciprocity principle or spline interpolation. In spite of this major difficulty, it was possible to migrate this data set in the double Radon domain, and produce a result comparable with the conventional processing.

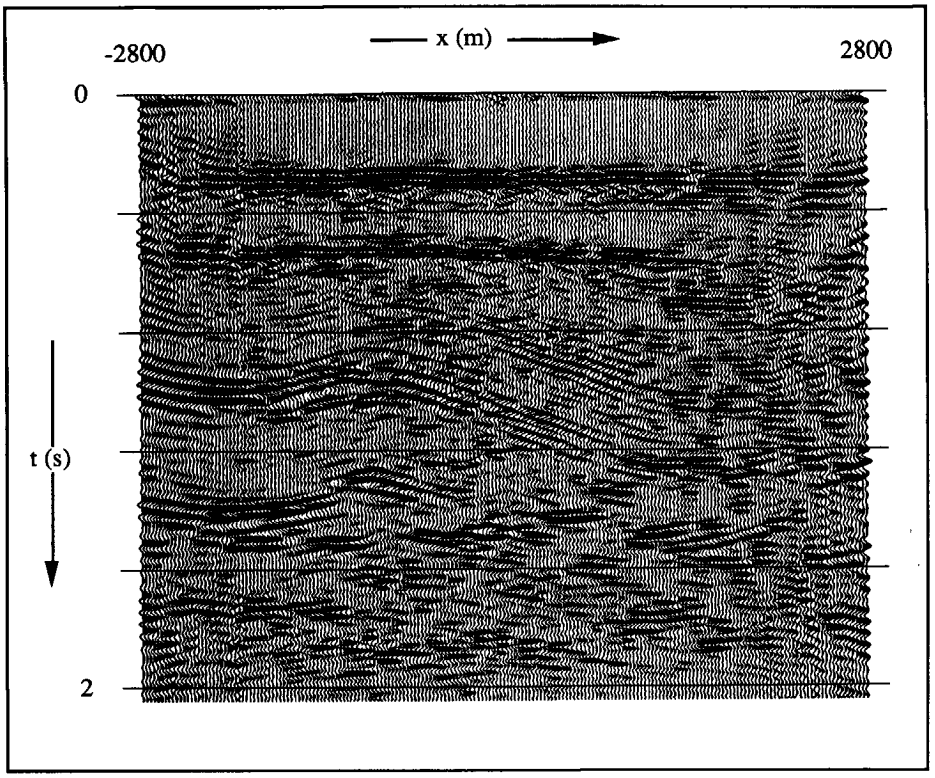

Fig.5.3.6: The result of imaging the Tubbergen data (spline interpolation)

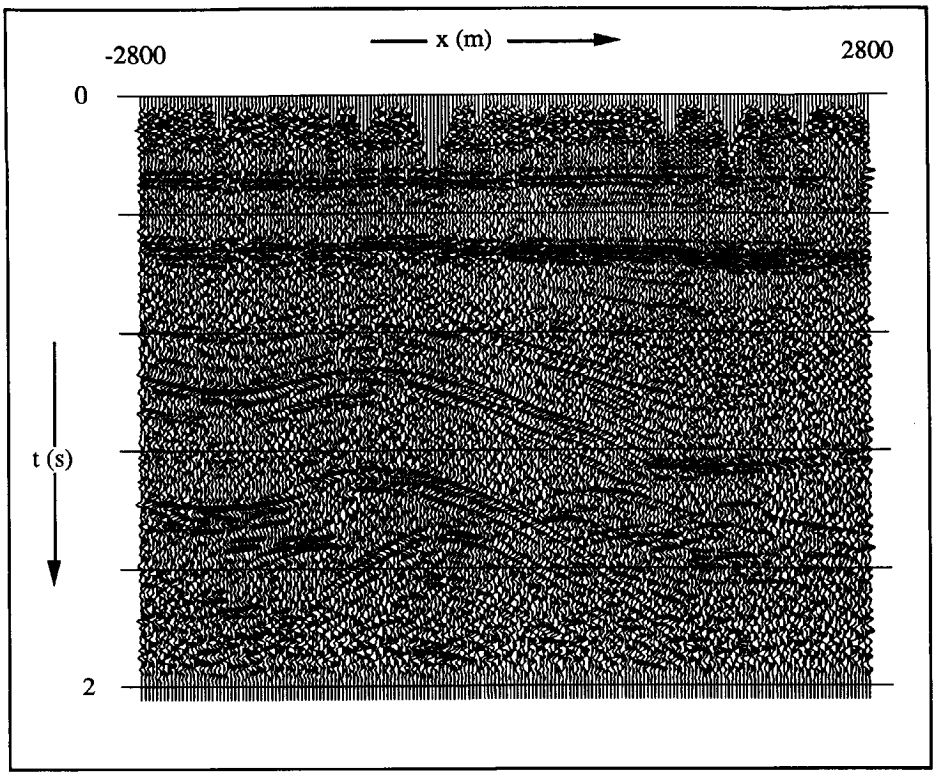

Fig.5.3.7: The conventional stacked section of the Tubbergen data

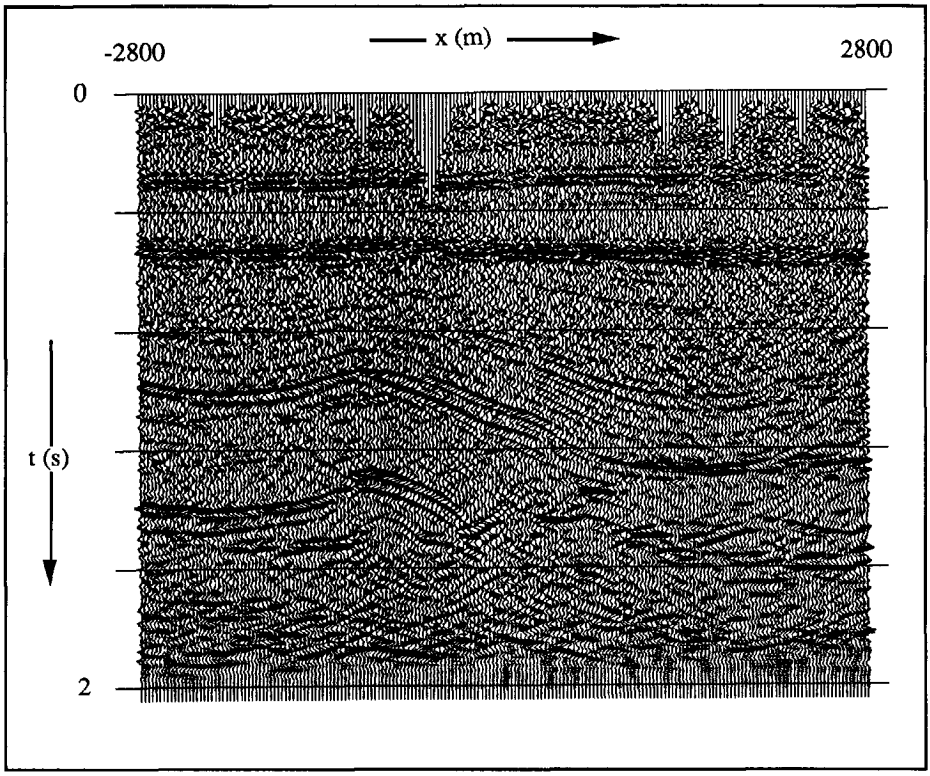

Fig.5.3.8: The *f-k* migration of the conventionally stacked Tubbergen data

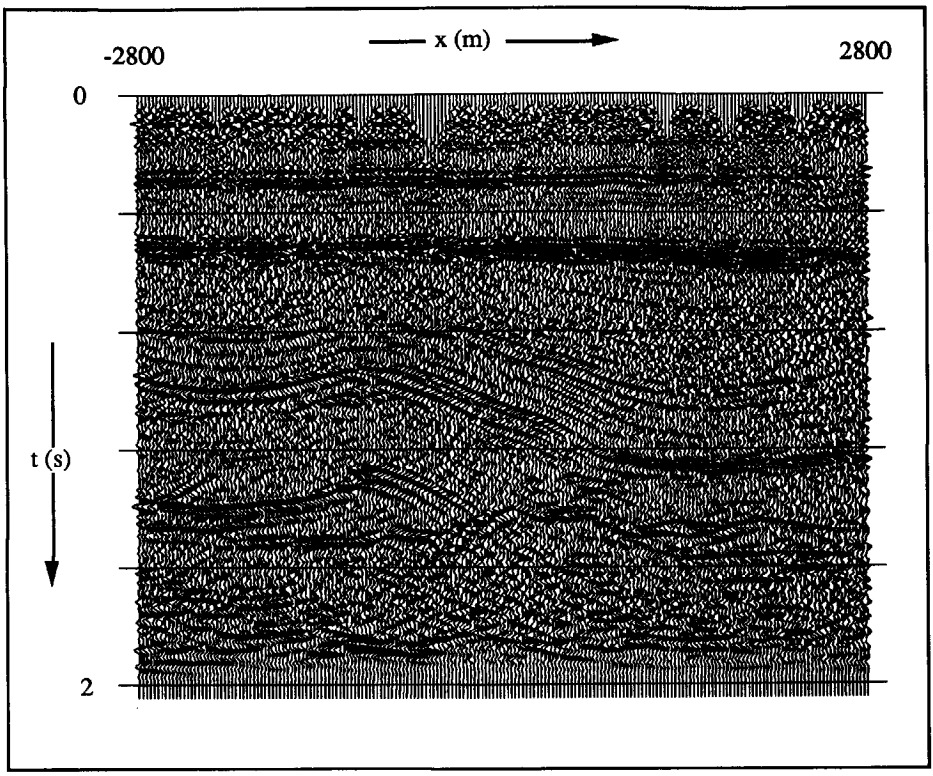

Fig.5.3.9: The finite-difference migration of the conventionally stacked Tubbergen data, band-pass filtered to 15-60 Hz

6

CONCLUSIONS

In the introduction of this thesis, the aim of migration was stated as the need to reveal the true geometry of subsurface reflectors, which consists of discontinuities in the acoustic impedance of the earth. It was also explained that all existing migration methods require the velocity structure of the earth to be known, in order to produce a reliable image of the reflectors. That is, the answer which is expected from migration, is required to be known in order to *do* the migration. This velocity paradox has inspired the present study, in which a pre-stack time migration algorithm has been developed. This migration method also needs the velocity function as an input parameter, but only as a background RMS velocity model rather than a detailed interval velocity model, and it also provides a way of obtaining a reliable RMS velocity.

Further, this migration method is applied prior to stack, thus the mis-stacking in areas of complex geology is avoided. Yet, a stack of individual migrated panels is carried out, which, like the conventional stack, improves the signal-to-noise ratio.

This new migration algorithm is developed as a time migration, which has both advantages and disadvantages. Time migration methods do not require a detailed velocity model, but neither do they produce a clear depth picture of the subsurface. On the other hand, depth migration methods produce more reliable and more detailed images of the subsurface, but only when an accurate input velocity model is available. Ultimately, it is a depth migration method which is required to produce the best image of the discontinuities in acoustic impedance.

Thus, for the full advantage of a pre-stack depth migration, an accurate knowledge of velocity is needed. With this in mind, the time migration algorithm presented here can be viewed as an important step in obtaining a good background velocity model for a subsequent depth migration. At the same time, it is more than a mere velocity estimation procedure, since it also produces a rather good time picture of the subsurface.

The new migration algorithm has been applied to simple synthetic models to illustrate the method. It was also applied to two challenging data sets. In the case of the Marmousi model

with a rather complex geology many of the assumptions made in the theory are violated. Yet, a quite acceptable time migrated section was produced. A practical drawback of the method is that it requires regular shooting geometry, in both source and receiver coordinates. This problem was overcome by using either reciprocity or spline interpolation and the method was successfully applied in the case of the real data from Tubbergen.

The highest dip possible to be imaged is limited, theoretically, to 60°. However, it was demonstrated with the simple syncline model, as well as with the Marmousi model, that dips higher than this still can be "seen", as long as their reflections are present in the data. There are migration methods which theoretically can migrate dips up to 90°, and even beyond 90° if the rays are bending with changing velocities. However, the real limitations to any migration methods come from the practical issues and from the data contents themselves.

A novel feature of operating in the double Radon domain is the possibility to perform the Radon transformation on data which originate from non-horizontal layers. The conventional Radon transform can be applied to a horizontally layered earth only, and for that reason it has been applied to the CMP-oriented data. It is the second Radon transform, which is performed with respect to the horizontal source coordinate, that makes it possible to apply the scheme to the shot - oriented data, without the assumption of horizontally layered earth. In this respect, the double Radon transform can be compared with the double Fourier transform methods.

An important property of the double Radon domain is the data discretization and separation according to the local time dip of the interfaces. This property enabled the development of a rather robust velocity estimation scheme in the $p^s = 0$ plane by curve fitting, where only energy contributions from horizontal segments are present. Thus, the estimated velocity is indeed the RMS velocity function, rather than a stacking velocity which is influenced by the dip of the reflectors.

The theory of the double Radon domain described in this thesis has been developed for the 3D case. Since the migration for 2D earth has been successfully applied here, the imaging theory can now also readily be extended to 3D. The need for 3D data and 3D migration schemes becomes obvious in areas where the assumption that the geology does not vary in the direction perpendicular to the seismic line is violated. Then, side scattering introduces a considerable amount of energy which cannot be properly migrated within a single seismic line.

Another possible extension of this theory is to include an extrapolation step which would correct for the ray bending at the interfaces, which in turn would lead to a depth migration algorithm. Then the time image and its velocity model, obtained by the pre-stack time migration as explained in this thesis, could be used as a starting model. The depth migration scheme would probably have to be organized as a layer-oriented operation, where imaging of the entire data could be performed in one step, followed by extrapolation to the first major reflector, correction for the ray bending, and only then the extrapolation to the next reflector. The data discretization into the planes of constant dip which occurs in the double Radon domain should be utilized for such an layer-oriented depth migration scheme. To be able to vary velocity laterally, which is

necessary in a depth migration, a combination between transform domain and space domain would have to be utilized, as in the split-step algorithm of Stoffa et al. (1990a, 1990b).

For the depth migration, the velocity analysis could be extended from estimation of a background velocity to estimation of interval velocities by a layer stripping scheme. In the τ-p domain (or in the p^S=0 plane), only the travel time curve from the first interface is elliptical, and all the underlying curves are distorted into pseudo-ellipses. After the interval velocity to the first interface is estimated, its distorting effect can be removed from all underlying interfaces, allowing estimation of the interval velocity of the next layer (Schultz, 1982). For dipping interfaces, the time dip separation in the double Radon domain can also be utilized for estimation of interval velocities, and the layer-stripping could then, in principle, proceed in the same way as for the horizontal interfaces.

APPENDIX

A.1 POLAR COORDINATES AND VARIABLES y^r, z^r

The Jacobian for the transformation $x^r_1, x^r_2 \rightarrow y^r, z^r$ is found as

$$dx^r_1\, dx^r_1 = \begin{vmatrix} \dfrac{\partial x^r_1}{\partial y^r} & \dfrac{\partial x^r_1}{\partial z^r} \\ \dfrac{\partial x^r_2}{\partial y^r} & \dfrac{\partial x^r_2}{\partial z^r} \end{vmatrix} dy^r\, dz^r. \tag{A.1}$$

The partial derivatives in equation A.1 are found as

$$\begin{aligned} \frac{\partial x^r_1}{\partial y^r} &= i\cos\theta^r & \frac{\partial x^r_1}{\partial z^r} &= \sin\theta^r \\ \frac{\partial x^r_2}{\partial y^r} &= i\sin\theta^r & \frac{\partial x^r_2}{\partial z^r} &= -\cos\theta^r \end{aligned} \tag{A.2}$$

Substitution of these derivatives into equation A.1 gives the Jacobian

$$dx^r_1\, dx^r_2 = -i\, dy^r\, dz^r. \tag{2.3.6}$$

To complete the transformation, the following calculations are needed

$$\begin{aligned}
\left(x_1 - x_1^r\right)^2 &= -\left(y^r\right)^2 cos^2\left(\theta^r\right) + \left(z^r\right)^2 sin^2\left(\theta^r\right) - 2\, i\, y^r\left(z^r\right) cos\,\theta^r sin\,\theta^r \\
\left(x_2 - x_2^r\right)^2 &= -\left(y^r\right)^2 sin^2\left(\theta^r\right) + \left(z^r\right)^2 cos^2\left(\theta^r\right) + 2\, i\, y^r\left(z^r\right) cos\,\theta^r sin\,\theta^r \\
\left(x_1 - x_1^r\right)^2 &+ \left(x_2 - x_2^r\right)^2 = \left(z^r\right)^2 - \left(y^r\right)^2
\end{aligned} \tag{A.3}$$

Using equations A.3, the distance $| x - x^r |$ becomes

$$\left| x - x^r \right| = \left[\left(z^r\right)^2 + \left(x_3 - x_3^r\right)^2 - \left(y^r\right)^2\right]^{\frac{1}{2}}. \tag{A.4}$$

Combining equations 2.3.4 and 2.3.5, the following expression is obtained

$$i\,\alpha_1^r\left(x_1 - x_1^r\right) + i\,\alpha_2^r\left(x_2 - x_2^r\right) = k^r y^r. \tag{A.5}$$

Substitution of equations A.4 and A.5, as well as Jacobian from equation 2.3.6 into equation 2.3.3, and changing $-i = 1/i$, the expression for $\widetilde{B}$ in equation 2.3.8 is obtained

$$\widetilde{B} = \frac{1}{4\pi i}\int_{-\infty}^{\infty} dz^r \int_{-i\infty}^{i\infty} \frac{\widehat{A}}{R^r}\, exp\left\{-is\left[k^r y^r + \frac{R^r}{c_0}\right]\right\} dy^r. \tag{2.3.8}$$

A.2 THE JACOBIAN FOR THE STEEPEST DESCENT ARGUMENTS

To calculate the Jacobian for the transformation from y^r to τ^r, expression for y^r in equation 2.3.12 is differentiated with respect to τ^r, leading to

$$\frac{\partial y^r}{\partial \tau^r} = \frac{k^r}{\left(k^r\right)^2 + \frac{1}{c_0^2}} + i\,\frac{\frac{\tau^r}{c_0}}{\left[\left(k^r\right)^2 + \frac{1}{c_0^2}\right]\sqrt{\left(\tau^r\right)^2 - \left(T^r\left(z^r\right)\right)^2}}. \tag{A.6}$$

On the other hand, equation 2.3.11 is rewritten to express R^r as

$$R^r = \tau^r c_0 - k^r y^r c_0 \,. \tag{A.7}$$

Substitution of parametric expression for y_1^r, given by equation 2.3.12, into equation A.7, leads to

$$R^r = \frac{\frac{\tau^r}{c_0}}{\left[\left(k^r\right)^2 + \frac{1}{c_0^2}\right]} - i\frac{k^r\sqrt{\left(\tau^r\right)^2 - \left(T^r(z^r)\right)^2}}{\left(k^r\right)^2 + \frac{1}{c_0^2}}. \tag{A.8}$$

Combining equations A.6 and A.8, the expression for Jacobian is recognized as

$$\frac{\partial y_1^r}{\partial \tau^r} = i\,\frac{R^r}{\sqrt{\left(\tau^r\right)^2 - \left(T^r(z^r)\right)^2}} \,. \tag{2.3.14}$$

A.3 HIGH FREQUENCY APPROXIMATION

A.3.1 Normal derivative

The normal derivative $\partial_n\left|x - x^r\right|$ has three components

$$\partial_n\left|x - x^r\right| = \frac{\partial\left|x - x^r\right|}{\partial x_1} n_1 + \frac{\partial\left|x - x^r\right|}{\partial x_2} n_2 + \frac{\partial\left|x - x^r\right|}{\partial x_3} n_3. \tag{A.9}$$

Taking each partial derivative and substituting back to A.9 leads to

$$\partial_n\left|x - x^r\right| = \frac{\left(x_1 - x_1^r\right) n_1 + \left(x_2 - x_2^r\right) n_2 + \left(x_3 - x_3^r\right) n_3}{\left|x - x^r\right|} \,. \tag{A.10}$$

The unit normal $\boldsymbol{n}$ of a function f is defined as

$$\boldsymbol{n} = \frac{\partial_1 f + \partial_2 f + \partial_3 f}{\sqrt{\left(\partial_1 f\right)^2 + \left(\partial_2 f\right)^2 + \left(\partial_3 f\right)^2}} \,. \tag{A.11}$$

In this case, the function f is given by equation 2.2.1, that is $f = x_3 - h\,(x_1, x_2) = 0$. Then the partial derivatives follow as

$$\frac{\partial f}{\partial x_1} = -\frac{\partial h}{\partial x_1} = \partial_1 h$$
$$\frac{\partial f}{\partial x_2} = -\frac{\partial h}{\partial x_2} = \partial_2 h \qquad \text{(A.12)}$$
$$\frac{\partial f}{\partial x_3} = 1 \quad .$$

Substitution of partial derivatives, equation A.12, into the unit normal in equation A.11 leads to

$$n = \frac{-\partial_1 h \; -\partial_2 h \; +1}{\sqrt{\left(\partial_1 h\right)^2 + \left(\partial_2 h\right)^2 + 1}} \; . \qquad \text{(A.13)}$$

Combining this equation with equation A.10 leads to the expression for $\partial_n \left| x - x^r \right|$ as

$$\partial_n \left| x - x^r \right| = \frac{-\partial_1(h)\left(x_1 - x_1^r\right) - \partial_2(h)\left(x_2 - x_2^r\right) + \left(x_3 - x_3^r\right)}{\left|x - x^r\right| \sqrt{\left(\partial_1 h\right)^2 + \left(\partial_2 h\right)^2 + 1}} \; . \qquad \text{(2.3.30)}$$

A.3.2 Expression for R^r

To derive equation 2.3.32, start from expression for R^r in equation A.8 and substitute $\tau^r = T_0^r$

$$R^r = \frac{\dfrac{T_0^r}{c_0}}{\left[\left(k^r\right)^2 + \dfrac{1}{c_0^2}\right]} \; . \qquad \text{(A.14)}$$

Substitution of equations 2.3.17 for T_0^r, and equation 2.3.27 for γ_0^r, leads directly to

$$R^r = \frac{x_3 - x_3^r}{c_0 \gamma_0^r} \; . \qquad \text{(2.3.32)}$$

A.3.3 Solution for $\hat{A}$

To calculate the expression for $\hat{A}$ in equation 2.3.33, the following calculations are needed. From equation 2.3.5, for $z^r = 0$,

$$x_1 - x_1^r = -i\, y_1^r \cos\theta^r, \tag{A.15}$$

and from 2.3.4, substituting $\cos\theta^r$,

$$x_1 - x_1^r = -i\, y_1^r \frac{\alpha_1^r}{k^r}. \tag{A.16}$$

The expression for y^r is obtained from equation 2.3.12, by substituting $\tau^r = T_0^r$ and using expression for T_0^r in equation 2.3.28 as

$$y_1^r = \frac{\gamma_0^r \left(x_3 - x_3^r\right) k^r}{\left(k^r\right)^2 + \frac{1}{c_0^2}}. \tag{A.17}$$

Using equation 2.3.27 for γ_0^r and equations 2.3.31 and 2.3.32 for R^r, this is written as

$$y_1^r = k^r c_0 \left| x - x^r \right|. \tag{A.18}$$

Substituting this expression into equation A.16 leads to

$$\frac{x_1 - x_1^r}{\left| x - x^r \right|} = -i\, c_0\, \alpha_1^r\ . \tag{A.19}$$

The equivalent expression is obtained for x_2, x_2^r as

$$\frac{x_2 - x_2^r}{\left| x - x^r \right|} = -i\, c_0\, \alpha_2^r\ . \tag{A.20}$$

Combining equations 2.3.31 and 2.3.32 for R^r, the following expression for x_3, x_3^r coordinates is obtained

$$\frac{x_3 - x_3^r}{\left| x - x^r \right|} = c_0\, \gamma_0^r\ . \tag{A.21}$$

Substitution of equations A.19, A.20, and A.21, into equation 2.3.29, leads to the expression for $\hat{A}$ given by equation 2.3.33

$$\widehat{A}_{|z^r=0,\,\tau^r=T_0^r}=c_0\eta\,\frac{i\,\alpha_1^r\partial_1 h+i\,\alpha_2^r\partial_2 h+\gamma_0^r}{\sqrt{\left(\partial_1 h\right)^2+\left(\partial_2 h\right)^2+1}}-\zeta\,\partial_n\left|x-x^s\right|. \tag{2.3.33}$$

REFERENCES

Baysal, E., Kosloff, D.D., and Sherwood, J.W.C., 1983, Reverse time migration: Geophysics, 48, 1514-1524.

Benoliel, S.D., Schneider, W.A., and Shurtleff, R.N., 1987, Frequency wavenumber approach of the τ-p transform: Some applications in seismic data processing, Geophysical Prospecting, 35, 517-538.

Berkhout, A.J., 1980, Seismic migration - Imaging of acoustic energy by wave field extrapolation: Elsevier Scientific Publishing Company.

Berkhout, A.J., and van Wulfften Palthe, D.W., 1979, Migration in terms of spatial deconvolution: Geophysical Prospecting, 27, 261-291.

Berkhout, A.J., Cox, H, Verschuur, E., and Waapenaar, K., 1991, The DELPHI approach to macro model estimation: in The Marmousi experience, Proceedings of the 1990 EAEG workshop on Practical Aspects of Seismic Data Inversion, EAEG, Zeist.

Bleistein, N., 1984, Mathematical methods for wave phenomena, Academic Press Inc., Orlando, London.

Bleistein, N., 1986, Two-and-one-half dimensional in plane-wave propagation: Geophysical Prospecting, 34, 686-703.

Claerbout, J.F., 1970, Coarse grid calculations of waves in inhomogeneous media with application to delineation of complicated seismic structure: Geophysics, 35, 407-418.

Claerbout, J.F., 1985, Imaging the earth's interior: Blackwell Scientific Publications.

Claerbout, J.F., and Doherty, S.M., 1972, Downward continuation of moveout corrected seismograms, Geophysics, 37, 741-768.

Claerbout, J.F., and Johnson, A.G., 1971, Extrapolation of time dependent waveforms along their path of propagation, Geophysical Journal of Royal Astronomical Society, 26, 285-293.

Deregowski, S., and Rocca, F., 1981, Geometrical optics and wave theory for constant-offset sections in layered media, Geophysical Prospecting, 29, 374-387.

Diebold, J.B., and Stoffa, P.L., 1981, The traveltime equation, tau-p mapping, and inversion of common midpoint data, Geophysics, 46, 238-254.

Dunkin, J.W., and Levin, F.K., 1973, Effect of normal moveout on a seismic pulse: Geophysics, 38, 635-642.

Fokkema, J.T. and van den Berg, P.M., 1992, Reflector Imaging: to be published in Geophys. Journal Int.

Fokkema, J.T., van den Berg, P.M., and Vissinga, M., 1992, On the computation of Radon transforms of seismic data: Journal of Seismic Exploration,1, 93-105.

Fowler, P., 1984, Velocity-independent imaging of seismic reflectors, Proceedings of the 54th Annual International SEG Meeting.

French, W.S., 1975, Computer migration of oblique seismic reflection profiles: Geophysics, 40, 961-980.

French, W.S., Perkins, W.T., and Zoll, R.M., 1984, Partial refraction via true CDP stacking, Proceedings of the 54th Annual International SEG Meeting.

Froberg, C.-E., 1965, Introduction to numerical analysis, Addison-Wesley publishing company, inc., Reading.

Gazdag, J., 1978, Wave-equation migration by phase shift: Geophysics, 43, 1342-1351.

Gazdag, J., and Squazzero, P., 1984, Migration of seismic data by phase shift plus interpolation: Geophysics, 49, 124-131.

Hale, I.D., 1984, Dip moveout by Fourier transform, Geophysics, 49, 741-754.

De Hoop, A.T., 1960, A modification of Cagniard's method for solving pulse problems, Applied Scientific Research, B8, 349-356.

De Hoop, A.T., 1988, Acoustic radiation from impulsive sources in a layered fluid: Niew Archief voor Wiskunde, Amsterdam, Vierde serie, Deel 6, No 1-2, 111-127.

Koster, J.K., 1991, A direct layer-stripping approach to the inversion of marine seismic data: Ph.D. Thesis, Delft University of Technology.

Levin, F.K., 1971, Apparent velocity from dipping interface reflections: Geophysics, 36, 510-516.

Loewenthal, D., Lu, L., Robertson, R., Sherwood, J.W.C., 1976, The wave equation applied to migration: Geophysical Prospecting, 24, 380-399.

McMechan, G.A., 1983, Migration by extrapolation of time-dependent boundary values: Geophysical Prospecting, 31, 413-420.

Neidell, N.S., and Taner, M.T., 1971, Semblance and other coherency measures for multichannel data: Geophysics, 34, 482-492.

Schneider, W.A., 1978, Integral formulation for migration in two and three dimensions: Geophysics, 43, 49-76.

Schultz, P.S., 1982, A method for direct estimation of interval velocities: Geophysics, 47, 1657-1671.

Sherwood, J.W.C., Schultz, P.S., and Judson, D.R., 1978, Equalizing the stacking velocities of dipping events via Devilish, Proceedings of the 48th Annual International SEG Meeting.

Slotnick, M.M., 1959, Lessons in Seismic Computing: SEG.

Stoffa, P.L., Fokkema, J.T., de Luna Freire, R.M., and Kessinger, W.P., 1990a, Split-step Fourier migration, Geophysics, 55, 410-421.

Stoffa, P.L., Sen, M.K., Fokkema, J.T., and Kessinger, W.P., 1990b, Pre-stack shot point and common midpoint migration using the split-step Fourier algorithm: presented at the 52nd EAEG Meeting, Copenhagen, Denmark.

Stolt, R.H., 1978, Migration by Fourier transform: Geophysics, 43, 49-76.

Stolt, R.H., and Benson, A.K., 1986, Seismic migration: Theory and practice, Geophysical Press.

Tatalovic., R., 1988, Dip correction of shot gathers in the tau-p domain, 58 SEG Meeting, Anaheim, 668-669.

Tatalovic., R., Stoffa, P.L., Fokkema, J.T., and Sen, M., 1990, Velocity estimation using the pre-stack split-step Fourier migration algorithm for plane-wave decomposed CMP data, Proceedings of the EAEG/SEG Velocity workshop, Cambridge.

Versteeg, R., and Lailly, P., 1991, EAEG Workshop report: Practical aspects of seismic data inversion, First Break, 9, 75-77.

Versteeg, R., and Grau, G. (editors), 1991, The Marmousi experience, Proceedings of the 1990 EAEG workshop on Practical Aspects of Seismic Data Inversion, EAEG, Zeist.

Vincentie, E., 1989, A qualitative comparison of velocity analysis in t-x versus τ-p, MSc Thesis, Delft University of Technology

Vissinga, M., 1992, The Radon transform and its applications to the interpretation of seismic data: Ph.D. Thesis, Delft University of Technology.

Yilmaz, O., 1987, Seismic data processing: Society of Exploration Geophysicists, Tulsa.

Yilmaz, O., and Claerbout, J.F., 1980, Prestack partial migration, Geophysics, 45, 1753-1777.

Ziolkowski, A.M., 1984, Deconvolution: IHRDC, Boston

Ziolkowski, A.M., and Bokhorst, K., 1992, Determination of the signature of a dynamite source using the source scaling, part 2: Experiment, submitted to Geophysics for publication

ACKNOWLEDGEMENTS

Part of this research has been financially supported by the EEC under contract number TH.01.121/88NL, The Inversion of Land Seismic Data, and by the KSEPL under contract number 97000884-EPR.

Even though only my name is signed under this thesis, many people contributed to this work in one way or another. I would like to thank to all of those who made positive contributions.

I am grateful to my promotor, Prof. Anton Ziolkowski, who enabled me to come to Delft, and who showed me how to say things in English so that I say what I actually wanted to say. Anton knew how important Fridays in de Kurk are for maintaining friendliness among colleagues.

The theory in this thesis was developed by Dr. ir. J.T. Fokkema and Prof. Dr. ir. P.M. van den Berg. I would also like to thank all the other members of my thesis committee, Prof. dr. ir. A.J. Hermans, Prof. dr. H. Rüter, Dr. ir. T.H. Tan, and Prof. S. Vaage.

During my Ph.D. study in Delft, I have spent 6 months at the University of Texas at Austin; it was there that I understood, by talking to Prof. Paul Stoffa, what migration is (at least, I would like to think that I understand migration!).

I want to thank Dr. Guy Drijkoningen and Evert Slob for reading this thesis in its early stage. I am specially indebted to Evert who revealed the (well hidden) beauty of complex integration to me. The transformation of my Summary into Samenvatting would not have been possible without help from Roald van Borselen and Guy.

Karel Bokhorst spent long hours processing the Tubbergen data with me; his conventionally stacked section and migrated sections are almost too good.

I am grateful to all the hard-working geophysics students for making the weekends in Mijnbouw building less lonely and evenings in het Noorden more enjoyable. My special thanks go to the D.O.G.S.

Ever since I started to study, first in Belgrade, then in Houston, and then in Delft, my fellow student, countryman and friend, Milos Savic, was nearby. In numerous discussions, we have attacked the problems in geophysics, Mijnbouw, TU Delft, Yugoslavia, world, and universe.

But none of it would have ever been possible, if it wasn't for my dear parents, Mika and Zdravko. Their love and unselfishness gave me the strength when I needed it.

And then, when it was really tough sometimes, there was my Oga, to hear my stories, and to love me and to support me.

SAMENVATTING

Het seismische golfveld, zoals het aan het aardoppervlak wordt gemeten, heeft zekere veranderingen ondergaan tijdens zijn propagatie door de ondergrond, en geeft niet direct het karakter van de ondergrond weer. Het is het doel van migratie om de ware geometrie van de ondergrondse reflectoren te onthullen. In dit proefschrift is een prestack tijdmigratie algoritme ontwikkeld dat wordt toegepast op schot-georienteerde en dubbel Radon getransformeerde data.

De Radon transformatie is traditioneel toegepast op CMP-georienteerde data waarbij is aangenomen dat de aarde uit vlakke horizontale lagen bestaat. De dubbele Radon transformatie bestaat uit twee stappen: de eerste transformatie, met betrekking tot de offset coordinaten, wordt toegepast op alle shotgathers van de seismische lijn, en de tweede is toegepast op de éénmaal-getransformeerde data set, met betrekking tot de schotcoordinaten. De introductie van de tweede transformatie maakt het mogelijk de Radon transformatie toe te passen zonder de aanname van een horizontaal-gelaagde aarde.

In het dubbel getransformeerde Radon domein wordt de data gediscretiseerd volgens de locale tijdshelling van de akoestische grensvlakken. De fasefunctie wordt opgesplitst in twee delen: de horizontale fase en de verticale fase. Dit maakt het mogelijk de data af te beelden door de verticale slowness constant te houden. Door de toepassing van deze voorwaarde wordt de gereflecteerde energie van een bepaald grensvlak geselecteerd in een afbeeldingsvlak. Eén inverse transformatie toegepast op de data in het afbeeldingsvlak leidt tot een tijd-afbeelding van het grensvlak. De methode van stationaire fase, gebruikt om de afbeeldingsvergelijkingen af te leiden, is een hoog-frequente benadering die de aanzet van de seismische "events" benadrukt.

De migratievergelijkingen zijn afgeleid voor een enkel grensvlak van willekeurige vorm, en dan uitgebreid voor een willekeurig-gelaagde ondergrond door een RMS achtergrond

snelheidsmodel te introduceren. Vanwege de discretisatie in het dubbel getransformeerde Radon domein, kan de snelheid direct worden verkregen uit de dubbel Radon getransformeerde data. Een vlak in de dubbel Radon getransformeerde data kubus wordt geselecteerd waarin alleen reflecties van de horizontale segmenten van de grensvlakken aanwezig zijn. Niet alleen wordt de beste fit tussen de theoretische krommes en de data bereikt in dit vlak, maar ook de RMS snelheidsfunctie wordt verkregen, in plaats van de stacksnelheden.

De verkregen achtergrond snelheidsfunctie is geldig voor de gehele dataset; omdat de migratie is toegepast in het spatieel-getransformeerde domein kan de snelheid niet lateraal varieëren. Deze restrictie kan zowel als een zwakte van de methode als zijn sterkte worden gezien. Het is niet wenselijk voor een migratie-algoritme dat het geen lateraal-variërend snelheidsmodel aankan; echter, een lateraal-variërend snelheidsmodel is het resultaat verwacht *van* de migratie, en dus is het niet voorhande voordat het migratieproces heeft plaatsgevonden. Het resultaat van elk migratie-algoritme dat een lateraal -variërend snelheidsmodel aankan, wordt sterk beinvloed door het *benaderde* lateraal-variërende snelheidsmodel. Aan de andere kant, een migratie-algoritme dat geen lateraal-variërend snelheidsmodel nodig heeft, zoals bijvoorbeeld hetgene wat gepresenteerd wordt in dit proefschrift, produceert een resultaat dat veel meer door de data zelf wordt beïnvloed, dan door een benaderd lateraal-variërend snelheidsmodel.

De methode is met success toegepast op twee complexe datasets: de Marmousi synthetische data set, en de Tubbergen dataset. Ondanks moeilijkheden, ontstaan door practische toepassingen, zoals grote structurele complexiteit in the Marmousi dataset, en een onregelmatige schotgeometrie in de Tubbergen dataset, zijn goede resultaten verkregen voor beide datasets. De verkregen resultaten zijn aanmoedigend voor verder onderzoek.

BIOGRAPHY

EDUCATION:

- B.Sc. in geophysics, University of Belgrade, Yugoslavia (1976 - 1981)
- M.Sc. in geophysics, University of Houston, Texas, USA (1983 - 1985)
- Ph.D. in geophysics, Delft University of Technology, The Netherlands (1988 - 1992)

WORK EXPERIENCE:

- Seismological Institute, Titograd, Yugoslavia, Seismogram analysis (1981)
- Geophysical Institute, Belgrade, Yugoslavia, Field Geophysicist (1982)
- Geophysical Institute, Belgrade, Yugoslavia, Exploration Geophysicist (1985 - 1987)